



HAL
open science

Versatile low-energy electron source at the PHIL accelerator to characterise Micromegas with integrated Timepix CMOS readout and study dE/dx for low energy electrons

Vladyslav Krylov

► To cite this version:

Vladyslav Krylov. Versatile low-energy electron source at the PHIL accelerator to characterise Micromegas with integrated Timepix CMOS readout and study dE/dx for low energy electrons. Instrumentation and Detectors [physics.ins-det]. Université Paris Saclay (COMUE); Kiiivs kij nacionalnij univërsitet imeni Tarasa Ševčënka (Ukraine), 2018. English. NNT: 2018SACLS169 . tel-02052226

HAL Id: tel-02052226

<https://theses.hal.science/tel-02052226>

Submitted on 28 Feb 2019

HAL is a multi-disciplinary open access archive for the deposit and dissemination of scientific research documents, whether they are published or not. The documents may come from teaching and research institutions in France or abroad, or from public or private research centers.

L'archive ouverte pluridisciplinaire **HAL**, est destinée au dépôt et à la diffusion de documents scientifiques de niveau recherche, publiés ou non, émanant des établissements d'enseignement et de recherche français ou étrangers, des laboratoires publics ou privés.

Versatile low-energy electron source at the PHIL accelerator to characterise Micromegas with integrated Timepix CMOS readout and study dE/dx for low energy electrons

Thèse de doctorat de l'Université Paris-Saclay et de Taras Shevchenko National University of Kyiv, préparée à l'Université Paris-Sud, au sein du Laboratoire de l'Accélérateur Linéaire

École doctorale n°576 Particules hadrons énergie et noyau : instrumentation, image, cosmos et simulation (PHENIICS)
Spécialité de doctorat : Physique des particules

Thèse présentée à Kyiv, le 12 juin 2018, par

M. Vladyslav Krylov

Composition du Jury:

M. Patrick Puzo Laboratoire de l'accélérateur linéaire, CNRS / Université Paris-Sud	Président
M. Giovanni Calderini Laboratoire de physique nucléaire et de hautes énergies, CNRS / Université Pierre et Marie Curie	Rapporteur
M. Volodymyr Yu. Storizhko Institute for Applied Physics NASU	Rapporteur
M. Igor N. Kadenko Taras Shevchenko National University of Kyiv	Examineur
M. Sergey Barsuk Laboratoire de l'accélérateur linéaire, CNRS / Université Paris-Sud	Co-directeur de thèse
M. Oleg A. Bezshyyko Taras Shevchenko National University of Kyiv	Co-directeur de thèse

To my parents

ABSTRACT

Within the present thesis the design, construction and commissioning of a new test beam facility LEETECH have been performed. Performance of the new facility, including low-multiplicity operation mode has been demonstrated. A number of interesting detector tests, including large-area diamond, Micromegas/InGrid and quartz bar detectors have been performed.

Development of new detector technologies for future high-energy physics collider experiments calls for selection of versatile test beam facilities, permitting to choose or adjust beam parameters such as particles type, energy and beam intensity, are irreplaceable in characterization and tests of developed instruments. Major applications comprise generic detector R&D, conceptual design and choice of detector technologies, prototypes and full-scale detector construction and tests, detector calibration and commissioning.

A new test beam facility LEETECH (Low Energy Electron TECHnique) was designed, constructed and commissioned in LAL (Orsay) as an extension of existing PHIL accelerator. Providing electron bunches of adjustable energy (up to 3.5 MeV), intensity (starting from a few particles per bunch) and bunch time duration (down to 20 ps), LEETECH fills the gap between high-cost high-energy test beam facilities and use of radioactive sources. Covering a minimum-ionization particles region (electrons of energy above 1.6 MeV), LEETECH provides for tracking detectors similar conditions as high-energy facilities.

Using LEETECH as an electron source, several types of detectors were investigated in order to study their performance or applications, also providing a characterization of the LEETECH performance. First studies of the LEETECH facility were performed with a plastic scintillator coupled to the Micro-channel plate photomultiplier. A low-multiplicity mode was investigated using the diamond sensor, at the same time demonstrating its ability to resolve bunches consisting of a few particles.

In framework of Time Projection Chamber development for the ILC project, a session dedicated to a large-area Micromegas/InGrid module was performed. For the first time the electron energy losses in Helium-based gas mixtures were measured for the energies of few MeV. The dE/dx resolution was obtained and track reconstruction algorithm was developed.

Being a candidate for the time-of-flight detector of the BESIII upgrade and future HIEPA tau-charm factories, a preliminary characterization of the quartz bar performed. The time resolution of the detector module of 50 ps was obtained, giving a promising results for the further detector studies.

RÉSUMÉ

Les futures expériences en physique des hautes énergies nécessitent une augmentation de la précision de détection sur de plus en plus grands volumes (où surfaces). Les précisions spatiales et temporelles sont importantes ainsi que la collecte rapide des signaux, la réduction du temps mort et l'amélioration de la résistance aux radiations. Les détecteurs gazeux sont reconnus pour leur efficacité dans des expériences où de grands volumes sont mis en jeu, là où les détecteurs silicium ne peuvent pas être exploités. Par conséquent, de nouvelles R&D complexes ont été lancées sur des détecteurs gazeux à hautes performances.

Les nouveaux programmes de R&D requièrent des plates-formes de test polyvalentes avec une précision élevée, utilisant des sources radioactives, des muons du rayonnement cosmique ou des faisceaux de particules dédiés. Ces derniers sont capables de fournir un nombre de particules important sur de courtes périodes avec une résolution temporelle élevée, au prix d'une difficulté à ajuster les caractéristiques du faisceau. Un autre inconvénient de ces dispositifs est leur faible disponibilité.

Cette thèse de R&D porte sur une nouvelle technologie Micromegas/InGrid développée par le Laboratoire de l'Accélérateur Linéaire (LAL), l'Université Nationale de Kiev et le CEA dans le cadre de la collaboration LCTPC. Pour cela, une plate-forme polyvalente appelée LEETECH a été conçue, construite et mise en service sur le faisceau d'accélérateur à photo-injecteur PHIL du LAL. Une approche pour fournir des échantillons étalonnés avec une énergie et un nombre d'électrons prédéfinis a été développée. Les mesures des pertes d'énergie des électrons avec un système de détection à grande échelle Micromegas / InGrid et avec un détecteur de diamant ont été effectuées à l'aide des échantillons d'électrons de LEETECH. Il faut noter que dans cette gamme d'énergie, ces mesures sont les premières jamais effectuées.

Un cycle complet de conception, de construction et de mise en service a été réalisé. Un cadre de simulation basé sur Geant4 a été développé, fournissant des informations sur les caractéristiques des clusters à la sortie de LEETECH en fonction des paramètres de configuration de l'installation.

Suite à la caractérisation de l'installation, plusieurs campagnes de mesures pour différentes technologies de détection ont été réalisées sur LEETECH. Les mesures du capteur de diamant ont démontré la capacité de LEETECH à fournir des paquets composés de quelques électrons et ont démontré la capacité du capteur de diamant à résoudre les signaux provenant de tels paquets.

Une caractérisation du premier détecteur Micromegas/InGrid de grande surface util-

isant les électrons de basse énergie a été réalisée et plusieurs caractéristiques telles que la résolution spatiale et les pertes par ionisation ont été mesurées. La technique de reconstruction de traces a été optimisée en tenant compte de la diffusion multiple et peut éventuellement être réutilisée pour la reconstruction online des futures expériences.

Enfin, la caractérisation temporelle de la barre de quartz couplée au MCPMT a été effectuée. Une résolution temporelle de 50 ps a été obtenue. Il s'agit d'une première démonstration du développement du détecteur de temps de vol pour un futur accélérateur tau-charm.

Une extension de l'accélérateur PHIL a été installée, permettant un réglage fin de l'énergie et de l'intensité des paquets d'électrons. En prenant en compte une longueur de paquet court provenant de PHIL (jusqu'à 20 ps) et un coût d'exploitation relativement faible (en raison de la faible énergie des électrons), le spectromètre construit représente une installation très compétitive parmi toutes celles existantes. Plusieurs séances de mesure ont démontré son applicabilité à la R&D sur les détecteurs.

Le chapitre 1 présente les solutions les plus abouties pour des détecteurs gazeux utilisant également des apports issus des détecteurs au silicium.

Le chapitre 2 passe en revue les expériences futures de Physique des Hautes Energies visant à réaliser de nouveaux tests de précision et à rechercher les effets au-delà du Modèle Standard. Les approches technologiques proposées pour ces expériences sont discutées en mettant l'accent sur les détecteurs de traces, en particulier gazeux, avec toujours pour objectif une optimisation des performances en vue de la physique recherchée.

Le chapitre 3 présente un aperçu des technologies de détection utilisant des détecteurs gazeux. Les techniques conventionnelles et bien établies sont d'abord discutées. Les nouveaux développements et en particulier les Micro Pattern Gaseous Detectors (MPGD) sont examinés plus en détail. La technologie Micromegas et l'extension de cette technologie InGrid, leurs avancées et leurs inconvénients, les problèmes de conception et de construction sont enfin discutés.

Le chapitre 4 propose un développement de la plate-forme polyvalente LEETECH sur le photo-injecteur PHIL au LAL pour la recherche et le développement de détecteurs (Figure 1). La simulation de la plateforme, la conception, la construction et la mise en service de LEETECH sont également présentées. Une approche permettant de fournir des échantillons étalonnés avec une énergie et un nombre d'électrons prédéfinis a été développée. Les résultats expérimentaux sont comparés à la simulation (Figure 2).

Le chapitre 5 détaille la simulation du détecteur Micromegas/InGrid permettant l'optimisation de sa conception. Pour cela, de nouveaux outils ont été développés dans le cadre de cette

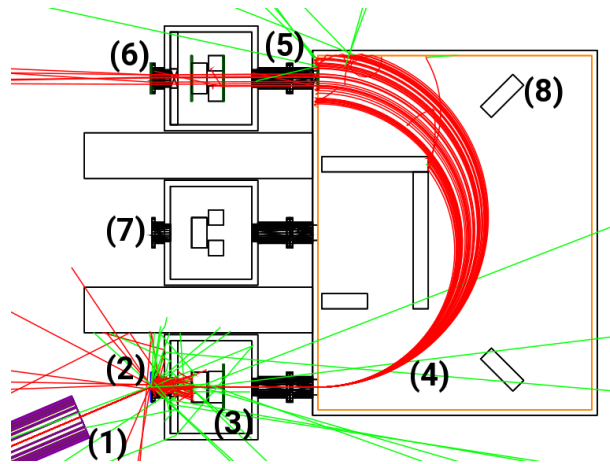


Figure 1: Schéma de l'installation LEETECH. Le tube de faisceau PHIL (1), l'atténuateur en aluminium (2), les systèmes de collimation (3, 5, 7), la région de champ magnétique (4), la zone du détecteur d'essai (6) et le blindage interne (8) sont représentés.

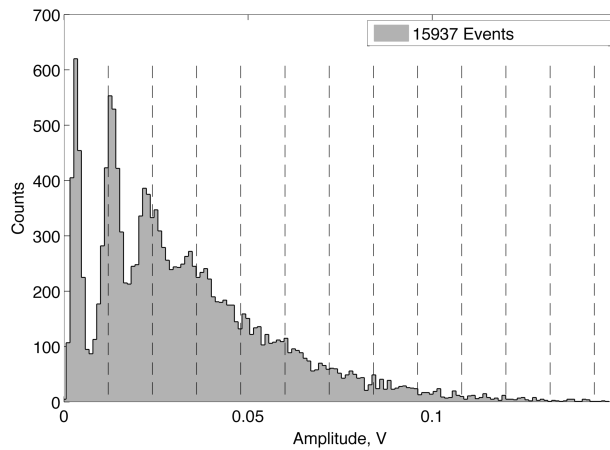


Figure 2: Histogramme représentant le dépôt d'énergie mesuré avec le capteur diamant. Le piédestal et les signaux correspondant aux paquets avec un et deux électrons sont clairement distingués.

thèse. Les pertes d'énergie des électrons dans un gaz sont détaillées. La technologie du détecteur Micromegas/InGrid offre une possibilité unique de fournir des mesures de précision des pertes d'énergie des électrons dans les gaz pour des électrons peu relativistes. Une technique de comptage en cluster (Figure 3) et mono-électrons est prometteuse pour ces études. Des études de simulation dédiées et les premiers résultats expérimentaux sont présentés dans ce chapitre (Figure 4). Les résultats du premier prototype de microTPC ainsi que la conception et la construction d'un prototype à grande échelle sont également

abordés. Une comparaison entre les résultats expérimentaux et la simulation est discutée.

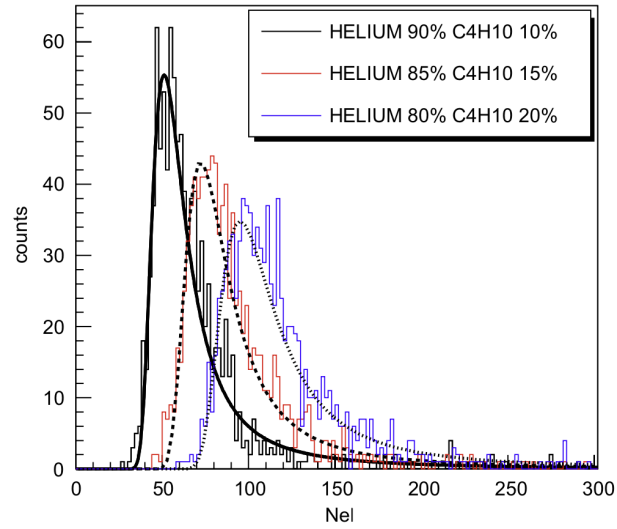


Figure 3: Nombre d'électrons libérés dans un gaz par unité de longueur pour une énergie primaire d'électrons de 50 GeV.

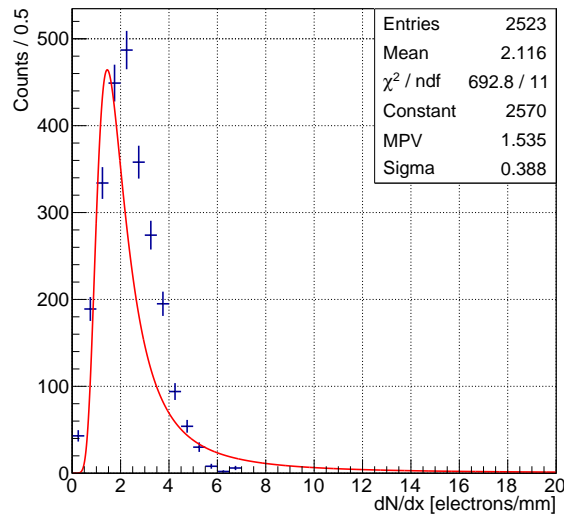


Figure 4: Nombre d'électrons par mm dans le mélange de gaz He/isoButane 80/20 obtenu avec la simulation Degrad.

Des résultats expérimentaux utilisant différentes technologies de détection sont présentés au chapitre 6. La campagne expérimentale sur les études du détecteur Micromegas/In-

Grid de grande surface (Figure 5) avec la plateforme LEETECH y est décrite. Le fonctionnement du détecteur et les résultats de l'analyse des données sont abordés (Figure 6). Une technique dédiée développée pour la reconstruction des traces avec un détecteur Micromegas / InGrid est présentée. Ce détecteur servira de prototype pour un détecteur de trace pour l'International Large Detector.

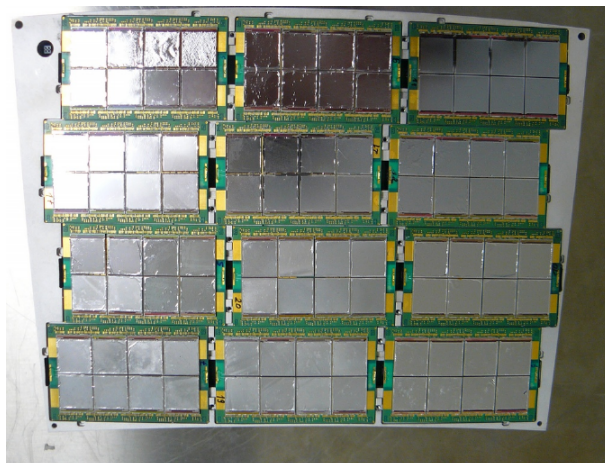


Figure 5: *Détecteur de suivi Micromegas / InGrid avec 96 chips Timepix.*

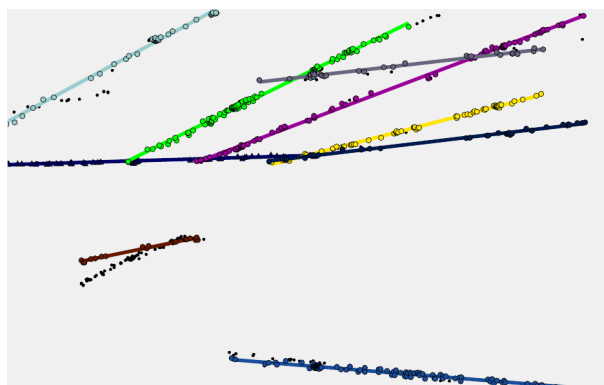


Figure 6: *Exemple d'événement reconstruit. La diffusion multiple et la production d'électrons delta sont présentées.*

Le chapitre 7 décrit une étude de la caractérisation du détecteur à barreaux de quartz couplé à un MCP-PMT (Figures 7, 8). Ce détecteur est un prototype pour le détecteur de temps de vol du collisionneur électron-positon BEPCII et pour le futur accélérateur d'électrons-positrons haute intensité HIEPA.

La thèse comporte plusieurs aspects. La conception, la construction et la mise en

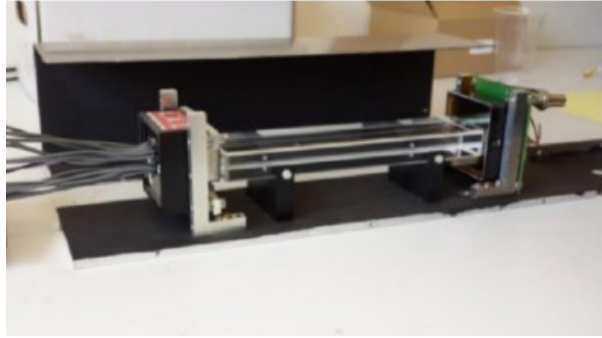


Figure 7: Composants de la configuration expérimentale du détecteur à quartz. Le barreau quartz de $20 \times 40 \times 200 \text{ mm}^3$, deux MCP-PMT et la plaque de recouvrement sont représentés.

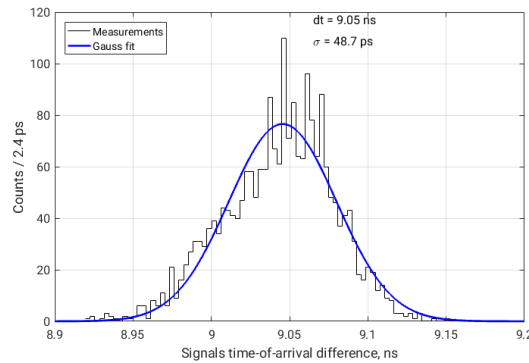


Figure 8: Exemple d'événement reconstruit. La diffusion multiple et la production d'électrons delta sont présentées.

service d'une nouvelle plateforme de tests (LEETECH) ont été effectuées. Basé sur l'accélérateur PHIL avec une énergie de faisceau comprise entre 3.5 et 5 MeV, pouvant être augmenté jusqu'à 10 MeV, LEETECH trouve sa place dans la caractérisation et les tests de détecteurs lorsqu'une grande énergie d'électrons n'est pas requise et que l'ajustement de l'énergie et de l'intensité du faisceau sont des exigences clé. Cela couvre un large éventail d'applications, notamment de nombreux tests de détecteurs gazeux et à semi-conducteurs, en particulier ceux pour lesquels des MIP sont souhaités, des applications en physique médicale et autres. Les performances de la nouvelle installation, incluant un mode de fonctionnement à très faible multiplicité, ont été démontrées. Un certain nombre de tests de détecteurs, notamment des détecteurs de diamant, des détecteurs à grande surface Micromegas/InGrid et des détecteurs à barres de quartz, ont été réalisés.

Il reste néanmoins un problème qui n'a pas pu être entièrement résolu: la réduction du bruit de fond synchrone avec le faisceau, très probablement causé par des particules

multidiffusées, permettrait d'améliorer les performances de la plateforme.

La simulation de LEETECH pourrait également être améliorée en utilisant des systèmes informatiques distribués tels qu'un cluster. Le GPU couramment utilisé peut être une option pour accélérer la simulation si cela devait être officiellement supporté par Geant4 dans le futur.



CONTENTS

Abstract	3
Résumé	4
Contents	11
1 Introduction	15
2 Future High-energy physics experiments	17
2.1 Introduction	18
2.2 Future high energy physics experiments	19
2.2.1 International Linear Collider (ILC)	21
2.2.2 Physics motivation	21
2.2.3 Advantages of lepton colliders	23
2.2.4 ILC detectors	24
2.3 Future Tau-Charm factories	26
2.4 Beijing Electron-Positron Collider II (BEPC II)	27
2.4.1 Particle identification at BES III	27
2.5 High Intensity Electron-Positron Collider (HIEPA)	29
2.6 Super $c\text{-}\tau$ Factory project (SCTF)	30
3 Micro-Pattern Gaseous Detectors	33
3.1 Introduction	34
3.2 Electron passage in gas	34
3.2.1 Clusters and ionization process	35
3.2.2 Electron transfer	36
3.2.3 Multiplication process	38
3.2.4 Gas gain variations	39

3.3	Wire tube	40
3.3.1	Operating principle	40
3.4	Multi Wire Proportional Chamber	42
3.5	Drift chamber	43
3.6	Time projection chamber	44
3.7	Micro Pattern Gaseous Detectors	46
3.7.1	GEM	46
3.7.2	Micromegas	47
3.7.3	Timepix	48
3.7.4	Micromegas/InGrid	50
4	LEETECH spectrometer	55
4.1	Introduction	56
4.2	PHIL - Photoinjector at LAL	56
4.2.1	Working principle	58
4.2.2	Bunch timing	60
4.3	Motivation	62
4.4	LEETECH Development	63
4.4.1	Magnetic field estimation	64
4.4.2	Dipole magnet	65
4.4.3	Vacuum chamber	66
4.4.4	Collimator boxes	67
4.4.5	Collimator systems	68
4.5	Driving electronics	71
4.5.1	Master board	72
4.5.2	Slave board	72
4.5.3	Controller design	76
4.6	Simulation	78
4.6.1	Attenuator thickness optimization	78
4.6.2	Inner shielding	79
4.6.3	Energy spread	79
4.6.4	Beam propagation through the LEETECH spectrometer	80
4.7	Spectrometer characterization	81
4.7.1	Scintillator plate	81
4.8	Studying low intensities with diamond sensor	84

4.8.1	Diamond sensor	84
4.8.2	Calibration of diamond sensor	85
4.8.3	Deposited energy spectrum simulation	86
4.8.4	Measurements	90
4.8.5	Results	91
4.8.6	Conclusions	94
5	Electron energy losses	95
5.1	Introduction	96
5.2	dE/dx calculation algorithms	96
5.2.1	Truncated mean	97
5.2.2	Cluster counting	99
5.3	Simulation	100
5.3.1	HEED simulation	101
5.3.2	Geant4	102
5.3.3	Degrad simulation	110
6	Large-area InGrid module characterization	117
6.1	Experimental setup	118
6.2	Track reconstruction	118
6.2.1	Hough transform	120
6.2.2	Reconstruction results	121
6.2.3	Tracks selection criteria	123
6.3	Spatial resolution	124
6.4	dN/dx distributions	127
6.5	Discussion	128
7	Quartz detector prototype characterization	131
7.1	Introduction	132
7.2	Physics basics	132
7.3	Simulation	133
7.4	Experimental setup	133
7.5	Position recovery	136
7.6	Discussion	137
8	Main results	139

9 Discussion and outlook	141
Acknowledgements	143
A Appendix	159
A.1 Geant4 PhysicsLists options for primary ionization simulation	159

INTRODUCTION

For that future advances require precision tracking in large volumes/surfaces. Both spatial and time precision is important as well as fast signal collection, low dead time and improved radiation resistance. Gaseous detectors are known to ensure an efficient tracking in large volumes of large-scale experiments where silicon detectors cannot be exploited for entire tracking systems.

Therefore new challenging R&Ds of gaseous detectors with improved performance, both traditional and new technology approaches. Samples of most successful solutions based on gaseous detector technologies are demonstrated to ultimately approach a performance of silicon detectors and examples of new gaseous detector technologies are addressed in Chapter 3.

New R&D programs require versatile test platforms with high precision, based on radioactive sources, cosmic ray muons and in particular calibrated beam facilities. The latter are capable in providing large sample over a short test periods with a precision time stamp and the highest possible precision over large energy range and are proved to be cost effective.

The present Ph.D. thesis addresses the R&D of the new Micromegas/InGrid technology performed at LAL, TSNUK and CEA within the LCTPC collaboration. For that a versatile LEETECH platform has been designed, constructed and commissioned at the PHIL photo-injector accelerator beam. An approach to deliver calibrated samples with predefined energy and number of electrons has been developed. Measurements of the electron energy losses with a large-scale Micromegas/InGrid detector system and with an alternative diamond detector in the region, where no precise data is available so far, have been performed using the electron samples from LEETECH. Corresponding simulation framework has been developed, and few competitive simulation approaches have been used. The measurements have been compared to the simulation results.

After the introduction, the Chapter 2 reviews upcoming and projected large-scale HEP experiments of new generation aiming at new precision tests of the Standard Model

and search for the effects beyond the Standard Model. Proposed approaches to detector technologies for these experiments are discussed with the emphasis on tracking detectors and in particular gaseous together with the major goals of the physics programs.

The Chapter 3 outlines a review of gaseous detector technologies. Conventional and well-established techniques are first discussed. New developments and in particular MPGD are reviewed in more detailed. Micromegas technology and the InGrid technology extension, their advances and remaining challenges, the design and construction issues are finally discussed. The simulation framework development and the simulation campaign to detail the Micromegas/InGrid detector operation and further optimize the detector design is described in Chapter 5. The first microTPC prototype results and a large-scale prototype design and construction are also addressed. A comparison between the experimental results and simulation is discussed.

A development of the versatile LEETECH platform at the photo-injector electron accelerator PHIL for detector R&D is described in Chapter 4.

Simulation, design, construction and commissioning of the LEETECH platform are discussed. An approach to deliver calibrated samples with predefined energy and number of electrons has been developed. Experimental results are compared with the simulation. Experimental results using different detector technologies are presented. Experimental campaign of the large-scale Micromegas/InGrid detector studies with the LEETECH platform is discussed in Chapter 6. Detector operation and data analysis results are addressed. A dedicated technique developed for the track reconstruction with a large-scale Micromegas/InGrid detector is presented. The studied large-scale Micromegas/InGrid detector will serve a prototype for the tracking detector candidate for ILD.

Electron energy losses in gases are discussed in Chapter 5. A unique possibility to provide precision measurements of the electron energy losses in gases in the energy region, where no precision data are available so far, is provided by the Micromegas/InGrid detector technology. A cluster and single-electrons counting technique is promising for these studies. Dedicated simulation studies and first experimental results are reported in this chapter.

The timing study of the quartz bar detector coupled to MCP-PMT, which is a candidate for the time-of-flight detector upgrade at the Beijing Electron-Positron Collider II (BEPC II) and for future High-Intensity Electron-Positron Accelerator (HIEPA) are described in Chapter 7.

Chapter 8 concludes the performed studies and outlines perspectives for applications in future HEP experiments.

FUTURE HIGH-ENERGY PHYSICS EXPERIMENTS

This chapter aims at addressing selected modern high-energy physics problems to motivate a strategy for the future large-scale experiments. It justifies a scope of priorities for the detector technology race in a challenge to satisfy the increasing demand in measurement precision, fast timing, granularity, large-area coverage, robustness and radiation resistance. With the discovery of the Higgs boson [1] with the mass predicted by the Standard Model, it passed another crucial test. A large part of future colliders physics program is focused on precision studies of the Higgs boson properties, to further search for an evidence of a new physics.

Two main approaches for further studies are described, the energy and precision frontiers. Several future experiments - the ILD experiment at ILC and tau-charm factory HIEPA along with the major upgrade of BEPC and BES III are discussed in more details, mentioning the new competitive detector technologies in the context of the work done in the current thesis.

2.1 Introduction

The Standard Model of strong and electro-weak interactions [2] provides currently the most complete and consistent picture that describes the observed phenomena in particle physics. The Standard Model major parameters have been both predicted theoretically and measured. Sometimes this required a major experiment and effort such as the LHC construction to discover the Higgs boson, followed the former searches at LEP, also aiming at Higgs boson discovery but in e^+e^- collisions.

A great achievement of the Standard Model is its predictions power. For example, the Higgs boson was precisely predicted by theory [3] before the actual discovery. The Figure 2.1 shows the state of prediction before Higgs boson discovery in 2012, which confirmed the Standard Model validity and demonstrated its prediction power.

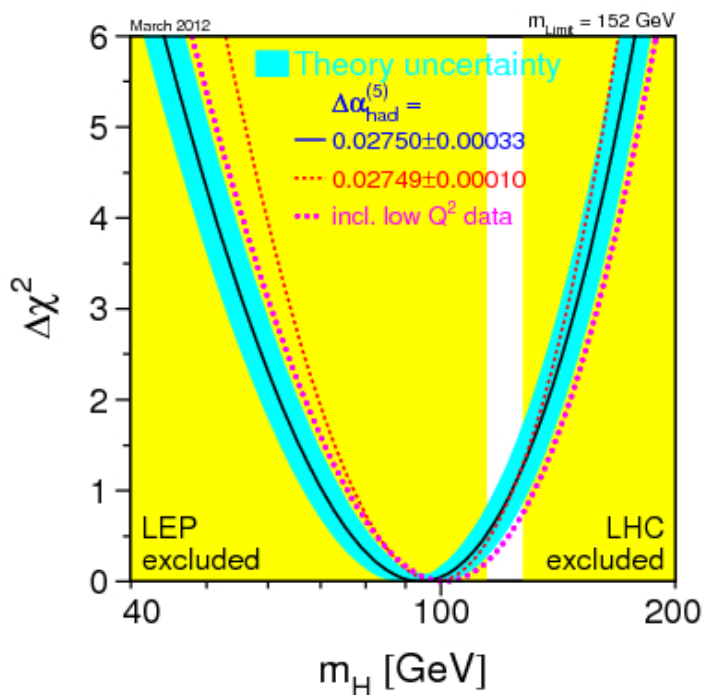


Figure 2.1: Higgs boson mass predictions by Standard Model and experimental search as of January 2011 [4]. The yellow regions represents experimentally excluded mass range.

This accomplished the particle spectrum required by the Standard Model, which is an outstanding achievement. However an explanation of the observed dark energy and dark

matter, complete neutrino properties description, matter-antimatter asymmetry, numerical values of particles masses, which are still free parameters of the Standard Model are promising tests of the Standard Model and its numerous extensions [5].

2.2 Future high energy physics experiments

From the experimental side, searches for the new physics continue in two main directions: *energy frontier* - when the centre-mass energy of accelerator is increased to directly produce new particles, and *precision frontier* (also known as intensity frontier) - when the experiment aims at precision measurements of the effects predicted by Standard Model in order to probe contributions from particles or interactions beyond the Standard Model. Selected future experiments representing both approaches are briefly listed below.

The Super LHC or High Luminosity LHC (SLHC, HL-LHC) [6] is the proposed upgrade to the LHC with the LHC, aiming at increasing the luminosity by factor of 10 to $10^{35} \text{ cm}^{-2}\text{s}^{-1}$.

The Future Circular Collider (FCC) [7] is the LHC successor, aiming at 100 TeV center-of-mass energy for the hadron beams and up to 350 GeV for the electron beams. This allows to extend the mass range for direct production of possibly existing particles up to 30 TeV and to increase the Higgs boson production cross-section. The LHC is presumed to be an injector for FCC for which a new 80-100 km-long tunnel is to be constructed.

The precision frontier measurements do not necessarily require such high energies and related high-technology and expensive accelerator solutions.

Circular Electron Positron Collider (CEPC) [8] - an electron-positron collider in China, aiming at 240 GeV and then go around 500 GeV center-of-mass energy. The synchrotron losses are reduced by using a large tunnel of 53.6 km circumference (twice as large as that of LHC).

The Belle II experiment [9] at the electron-positron collider SuperKEKB is planned to operate at luminosity about $8 \cdot 10^{35} \text{ cm}^{-2}\text{s}^{-1}$, aiming at quantitative description of CP-violation in B-sector.

The mainstream successor of the LHC in the view of further states of Higgs boson properties and search for the new physics in the precision frontier is the International Linear Collider (ILC), which will be described in more details in Section 2.2.1.

On the other hand hadron colliders can reach higher energies, thus maximizing production cross-section of heavier particles. This is illustrated by Figure 2.2, where the dependence of the Higgs boson production cross-section as a function of the LHC center-

of-mass energy is compared to the total cross-section for the $p\bar{p}$ collisions. It clearly shows that even at highest possible at LHC energy the selectivity to detect Higgs boson production has to be of at least of the 10^{-10} order.

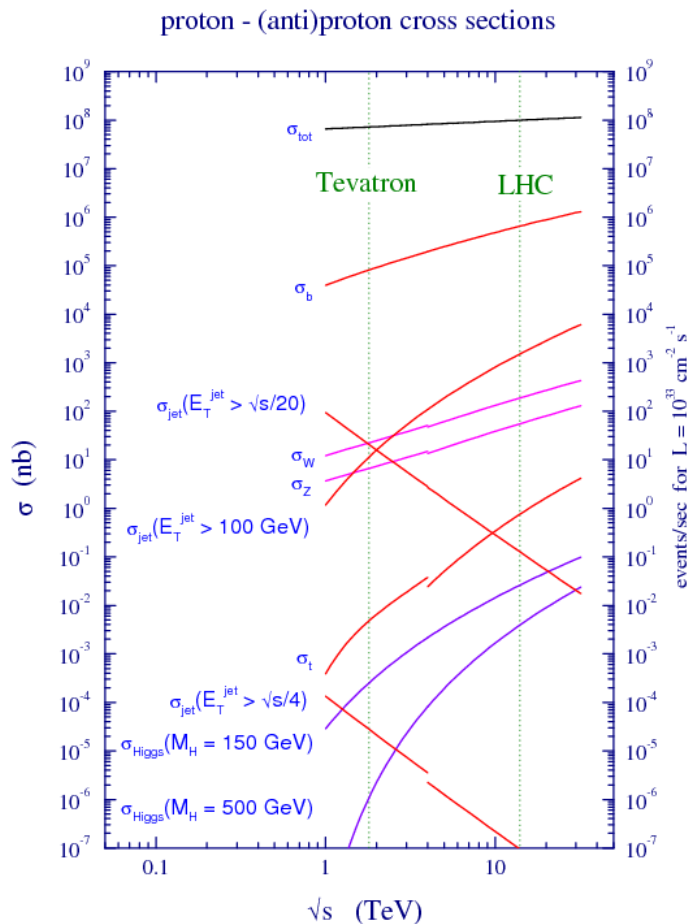


Figure 2.2: Higgs boson production cross-section as a function of centre-of-mass energy at LHC with respect to the background processes contribution to the total $p\bar{p}$ collisions cross-section.

Particle production mechanisms at e^+e^- colliders and at hadron colliders are very different. The e^+e^- colliders are advantageous because of reduced level of background and in particular for particles with $J^{PC} = 1^{--}$ quantum numbers, that can be produced directly via the $e^+e^- \rightarrow \gamma^* \rightarrow V$ process. In addition, an event can be fully reconstructed calculating missing energy and momentum in 4π detectors.

Therefore, many of the precision frontier experiments uses an electron-positron col-

lisions in order to clear the background and increase the probability to detect a new rare events. Therefore, a measurements precision, defined by large area high-granularity, radiation resistant detectors resolution, plays a crucial role.

Further in this chapter a short description of the future ILD experiment at International Linear Collider (ILC) and future tau-charm factory projects at the upgraded Beijing Electron–Positron Collider II (BEPC II), at High-Intensity Electron-Positron Accelerator (HIEPA) or at Novosibirsk facility is given. Large-area Micromegas/InGrid technology, studied in this thesis (Chapter 6) is a promising solution for the TPC readout of the future ILD detector, while a quartz detector coupled to MCPMT (Chapter 7) has been proposed as a forward time-of-flight detector for charged hadron identification in future tau-charm factories.

2.2.1 International Linear Collider (ILC)

Among the post-LHC colliders the most elaborated including the engineering phase is the International Linear Collider (ILC). The positron-electron (e^+e^-) beams will collide at the centre-of-mass energy of 250-500 GeV (with a possible later upgrade to 1 TeV). The extensive study of Higgs boson properties benefits at the centre-of-mass energy about 240 GeV, where the $e^+e^- \rightarrow Zh$ cross section is largest [10], the corresponding facilities are called Higgs-factories. Further energy increase aims at the top quark study (350 GeV) and new physics search.

2.2.2 Physics motivation

At present, the Large Hadron Collider (LHC) is the world’s largest and highest-energy particle accelerator with colliding proton beams. It is designed to reach centre-of-mass energies of 14 TeV with a high peak luminosity of $10^{34} \text{ cm}^{-2}\text{s}^{-1}$. The LHC gives access to high energies for direct production of new particles. However, the production rates of new particles proposed by theoretical models are typically $10^{10} - 10^{12}$ of the proton-proton total cross section. Even after selection of characteristic event types, these processes represent far below 10% of the total yield, over a background consisting of complex Standard Model reactions. This limits both the range of new processes that can be searched for and the precision with which the rates can potentially be measured [11].

With the discovery of the Higgs boson the Standard Model has received a complete list of particles and could be correct up to very high energies. However, it does not explain the most basic fact about the Higgs field, why it is that this field forms a condensate that

fills space and gives rise to the masses of all known elementary particles [12]. Second, it has no place for the particle or particles that make up cosmic dark matter, a neutral, weakly interacting substance that, according to astrophysical observation, makes up 85% of the mass in the universe and 25% of its total energy [13]. Third, it does not explain the asymmetry in the amount of matter and antimatter in the universe [14]. One might add to this list many more fundamental questions, for example, why quarks and leptons, which make up observed matter, have the quantum numbers that they do. However, these three questions are the keys to progress through experiment. The most pressing issue in particle physics today is that of where and how the Standard Model breaks down. If the questions just listed have answers given by current theoretical proposals, new particles and forces beyond the Standard Model should appear at the leading accelerators currently operated and planned—the LHC and the ILC.

The most important aspects of the ILC physics program are measurement of the properties of the newly-discovered Higgs boson with very high precision; measurement of the properties of the top quark with very high precision; searches for and studies of new particles expected in models of physics at the TeV energy scale.

The LHC measurements of Z boson polarization in $h \rightarrow ZZ \rightarrow 4$ lepton events already gives strong evidence that the Higgs boson couples to the Z boson in the specific manner required to give the Z boson its mass. More generally, the LHC measurements of the various production and decay reactions of the Higgs boson are all consistent with the picture of the Higgs field as the origin of all elementary particle masses. The current situation is illustrated in Figure 2.3 [11]. Left plot illustrates the Higgs couplings predicted by Standard Model and the data fit from CMS experiment. Right plot shows the expected measurement precision improvement at the ILC [15].

With the measurement of the mass of the Higgs boson, now known to 0.2% accuracy, the parameters of the Standard Model are fixed. All other properties of the Higgs boson are predicted by the model. The observation of any deviation from these predictions would be a clear indication of physics beyond the Standard Model. Different models of physics beyond the Standard Model lead to different patterns of deviation from the predicted Higgs boson couplings. In supersymmetric models, and more generally in models with more than one fundamental Higgs field, the largest deviations are expected to be found in the couplings to the down-type quarks and leptons and in the effective couplings to photons and gluons. In models in which the Higgs boson is composite, the effects of compositeness produce a uniform decrease in all of the Higgs couplings. Such models may also have partial top quark compositeness and heavy top partners; these effects induce

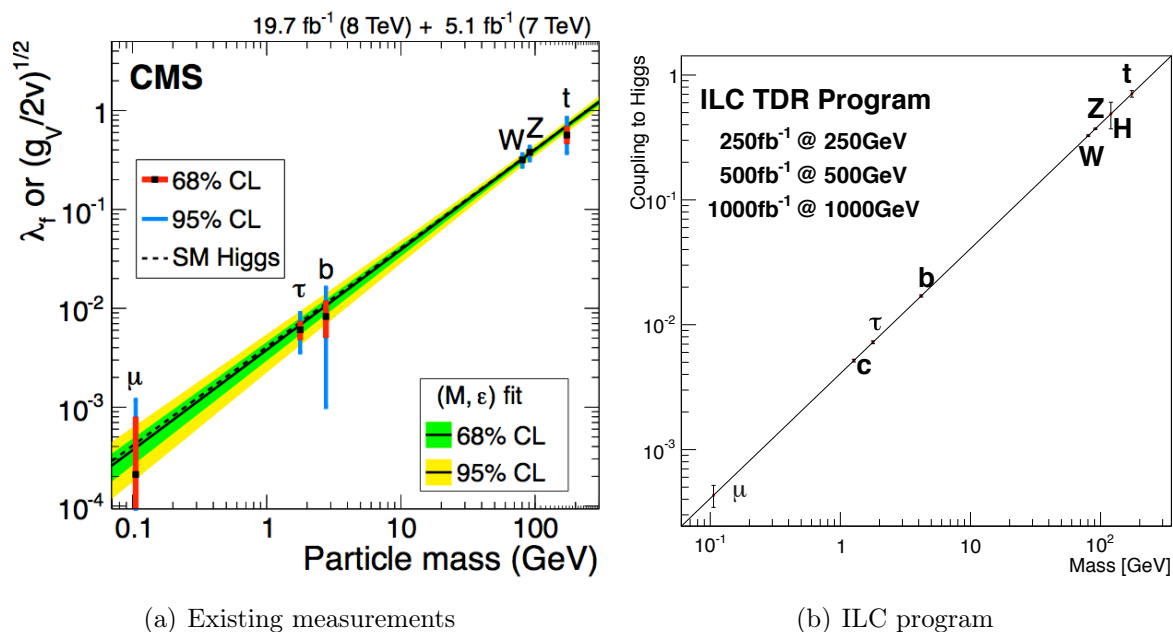


Figure 2.3: Higgs boson coupling to different particles at LHC (a) and ILC (b). [11]

further shifts of the Higgs couplings to top quarks and to photons and gluons. Thus, the measurement of the couplings of the Higgs boson will give evidence on the question of whether the Higgs boson is a fundamental scalar particle—the first ever observed—or a composite of more fundamental constituents [11].

2.2.3 Advantages of lepton colliders

In contrast to hadron interactions, the lepton collisions are characterised by much lower background. ILC provides an accurate knowledge of the initial conditions like centre-of-mass energy, initial state helicity and charge. The interaction of electrons and positrons is purely electroweak and the Standard Model background is low. The requirements for radiation resistance are reduced compared to those at LHC. This allows an employment of high-precision detectors with low material budget. To increase the beam energy to the required level, a linear collider instead of a circular collider will be needed. In a ring accelerator, the energy loss in one turn due to synchrotron radiation emitted by accelerated particles is proportional to $\Delta E \sim \frac{E^4}{m^4 R}$, where R is the curvature radius of the accelerator, m is the particle mass and E is the beam energy. The energy loss increases as a fourth power of the beam energy and decreases only linearly with the radius. This makes a circular lepton collider unacceptably large if it is supposed to run beyond centre-of-mass

energy of 250 GeV. Therefore the ILC will be a linear machine to avoid the synchrotron radiation losses.

The ILC will be the first collider to reach the e^+e^- production threshold at around 350 GeV. This allows the mass and the electroweak properties of the top quark to be accurately measured.

2.2.4 ILC detectors

Despite the fact that ILC has a single interaction point two detectors will be to be constructed: a Silicon Detector (SiD) and International Large Detector (ILD) [16]. A motivation to build two different detectors is to have a possibility to perform verifications in case if unexpected result is obtained. They are going to be installed on the moving platforms which can move a detector in the beam or park it into the corresponding garage (Figure 2.4).

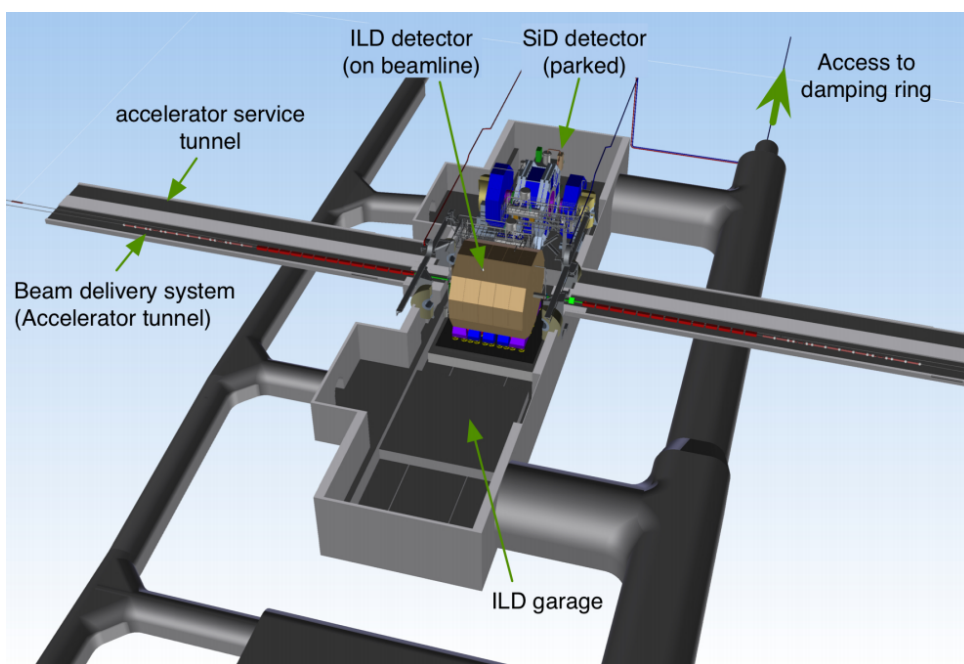


Figure 2.4: Design of two detectors place at the ILC interaction point. ILD in on the beamline and SiD is parked in the close-by maintenance position.

The SiD detector is designed to have a purely silicon tracker system while in the ILD the main tracker is a time projection chamber. Since a large part of this thesis is dedicated to the InGrid gaseous detector for the time projection chamber readout, the ILD detector is described below in more details.

The schematic view of the ILD is shown as a quadrant view in Figure 2.5. Particles, coming from the beam interaction region, cross first a multi-layer pixel-vertex detector (VTX), with three super-layers each comprising two layers, or a five layer geometry. A system of silicon strip and pixel detectors surrounds the VTX detector. In the barrel, two layers of silicon strip detectors (SIT) are arranged to bridge the gap between the VTX and the TPC. The time-projection chamber (TPC) - a distinct feature of ILD - covers a large yielding up to 224 reconstructed interaction points per track. The TPC is to provide for 3-dimensional point resolution with a minimum material in the field cage and in the end-plate. It also allows particle identification based on the dE/dx measurement.

Outside the TPC a system of Si-strip detectors, one behind the end-plate of the TPC and one in between the TPC and the electromagnetic calorimeter (ECAL), provide additional high-precision space points which improve the tracking performance and provide additional redundancy in the regions between the main tracking volume and the calorimeters. A highly segmented sampling electromagnetic calorimeter provides up to 30 samples in longitudinal direction and a small transverse cell size. The ECAL is split into a barrel and an end cap system. Tungsten has been chosen as an absorber. For the sensitive area, silicon diodes or scintillator strips are considered. The ECAL is followed by a highly-segmented hadronic calorimeter (HCAL) with a Steel-absorber structure and up to 48 longitudinal samples and a small transverse cell size [17].

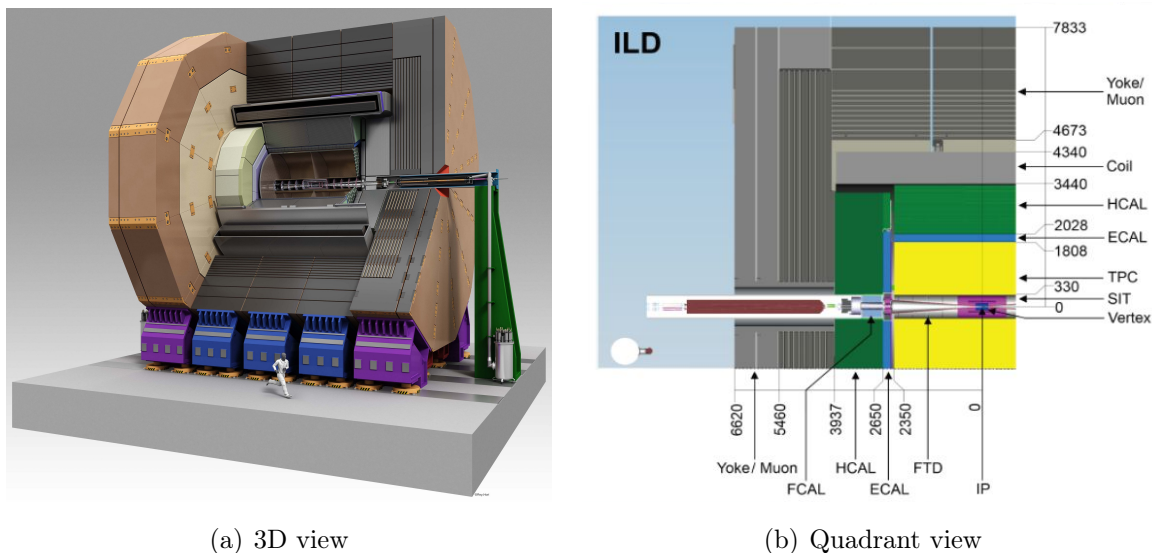


Figure 2.5: The ILD detector view.

Table 2.1: *Physics program outlined for the design of BEPC-II Tau-Charm factory depending on the collider luminosity [18]*

	glueballs, hybrid exotic and hybrid charmonium
	excited ψ and D states
	semi-leptonic D decays to O(1%) precision
	τ decay Br's to O(0.1%) precision
10^{32}	$\Lambda_C^\pm, \Sigma_C, \Theta_C, \Omega_C$, etc. decays to O(5%) precision
	V-A structure in τ decays comparable to precision in μ decays
	doubly Cabibbo suppressed D^0, D^\pm, D_s^\pm decays to O(3%) precision
	pure leptonic D decays, f_D , to O(2%) precision
	$\tau \rightarrow eX$ limit $\simeq 10^{-5}$; constraints on ν_τ masses below $1 \text{ MeV}/c^2$
	D^0/\bar{D}^0 mixing at SM level, 10^{-5} rare $\tau/D/J - \psi$ decays
	to limits $\simeq 10^{-7} - 10^{-8}$
10^{33}	direct ν_τ , mass limit $\simeq 1 \text{ MeV}/c^2$
	CP violation in D decays a SM level
	CP violation in τ decays at milli-weak level (10^{-3})
	CP violation in Λ, Θ decays at SM level

2.3 Future Tau-Charm factories

The Tau-Charm factory represents a high-luminosity e^+e^- collider which operates at energy near the threshold of tau lepton pair and a $c\bar{c}$ production. The high luminosity provides conditions for measurements of tau-neutrino mass, search for CP-violation in τ -sector and charm decays, studies of very rare and forbidden decays of τ and charm hadrons, precision studies for $D^0 - \bar{D}^0$ mixing, precision glueball searches.

The largest tau-charm factory is Beijing Electron-Positron Collider II (BEPCII), which has reached its maximum luminosity of $10^{33} \text{ cm}^{-2}\text{s}^{-1}$ in 2016. Its physics program is summarized in Table 2.1, being mainly executed to the date. Then further upgrade for the BEPCII is being discussed. Construction of future tau-charm factories is being discussed with a general goal of reaching instantaneous luminosity of $10^{35} \text{ cm}^{-2}\text{s}^{-1}$ us-

ing new acceleration technologies. A first possibility can be a major upgrade of BEPCII machine.

One of the most promising projects of the future tau-charm factories is the High-Intensity Electron-Positron Accelerator (HIEPA), which will be described in more detail in Section 2.5.

Finally, a new Super C-Tau Factory is under planning in Budker Institute (Novosibirsk, Russia), aiming at luminosity of $10^{35} \text{ cm}^{-2}\text{s}^{-1}$ and energy range of 2-5 GeV. These projects are briefly discussed below.

2.4 Beijing Electron–Positron Collider II (BEPC II)

The Beijing Electron Positron Collider (BEPC II) located at Beijing, China, hosts a single experiment - Beijing Spectrometer III (BES III). Electrons and positrons are accelerated in a tunnel with a circumference of 237.5 m, covering the τ -charm energy region with energy ranges of $\sqrt{s} = 2 - 4.6 \text{ GeV}$, and collide at the interaction point (IP), where the BES III Experiment is located [19]. Launched in 2009, BEPCII achieved a maximum luminosity of $10^{33} \text{ cm}^{-2}\text{s}^{-1}$ [20] in 2016. This allowed for collection of large data samples and therefore producing a list of precision measurements.

BES III is a 4π detector, comprising main drift chamber (MDC), time-of-flight counter (TOF), CsI electromagnetic calorimeter and muon detector. Charged particle momenta are calculated using a curvature of the track measured in MDC due to magnetic field, provided by superconducting solenoid magnet (Figure 2.6(a)).

The BES III experiment has collected the world largest data samples of J/ψ events with more than 10^9 events as well as the largest data sample of $\psi(2S)$ ($\approx 0.6 \times 10^9$), $\psi(3770)$, $Y(4260)$ and $Y(4360)$ events collected so far.

2.4.1 Particle identification at BES III

Since a quartz detector coupled to micro-channel plate photomultiplier (MCP-PMT) is a promising solution for a forward time-of-flight (TOF) detector for BES III experiment, particle identification at BES III is described in more details below.

The particle identification part of the detector consists of a helium-based small-celled drift chamber and time-of-flight counters. This combination allows to extend the energy range of efficient particle separation, as explained below.

Main Drift Chamber (MDC)

The main drift chamber (MDC) is 2.58 meters in length and has an inner radius of 59 mm and an outer radius of 0.81 m. The inner and outer cylinders are carbon fiber. The polar angle coverage is $\cos(\theta) = 0.83$ for a track passing through all layers, and $\cos(\theta) = 0.93$ for one that passes through 20 layers. The end-plates are machined with a hole position accuracy better than 25 microns. Altogether there are 43 layers of 25 micron gold plated tungsten sense wires; the field wires are 110 micron gold-plated aluminum. The cells are approximately square, and the size of the half-cell is 6 mm in the inner portion of the drift chamber and is 8.1 mm in the outer portion. The chamber uses a 60/40 He/C_3H_8 gas mixture. The design spatial, momentum, and dE/dx resolutions are $\sigma_s = 130 \mu m$, $\sigma_p/p = 0.5\%$ at 1 GeV/c, and $\sigma_{dE/dx}/dE/dx \sim 6\%$, respectively. Beam tests performed with prototype electronics in a 1 T magnetic field yielded a spatial resolution better than 110 μm and dE/dx resolution better than 5%. Tests of the final chamber and readout electronics using cosmic rays without magnetic field yield a spatial resolution of $\sigma_s = 139 \mu m$ and cell efficiency of 97% [21].

Time of Flight Detector (TOF)

The TOF detector is divided into a barrel with a polar angle coverage of $|\cos(\theta)| < 0.82$ a radius of 81 to 92.5 cm and an endcap from $0.85 < |\cos(\theta)| < 0.95$, the total length being 2.3 m for the barrel part [20].

The system is based on plastic scintillators, which are read out by photomultipliers. TOF measures the flight time of a charged particle for particle identification which is related to the mass of the particle m , where L is the flight path and v is the speed of light:

$$\beta = \frac{L}{vt_m} \quad m^2 = p^2 \frac{1 - \beta^2}{\beta^2} \quad (2.1)$$

The time of flight of charged particles is used for particle identification by comparing the measured time against the predicted time, which one deduces from from the tracking and momentum information from the drift chamber.

For the flight time measurement the scintillation principle is used. The ionizing particles excite molecules in the scintillator. The de-excitation light is then emitted, which can be measured by the photomultiplier.

Using the known flight path the flight time difference for particles of different types can be obtained for particle discrimination. The limiting factor for this technique is time resolution. The single layer time resolution for 1 GeV muons is 100-110 ps, this increases

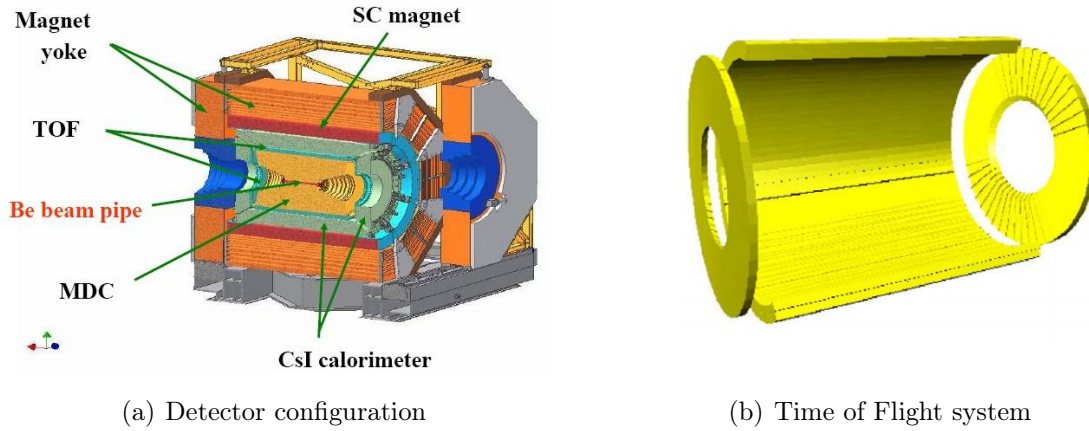


Figure 2.6: Schematic view of BES III detector and the time-of-flight system.

by 20% for kaons and pions, because of their strong interactions, whereas the double layer design was expected to have a total time resolution of 80-90 ps. The total time resolution for pions and kaons is in the order of 135 ps and therefore allows π/K separation at a 2σ level up to momenta of 1 GeV as described in Ref. [22].

BEPCII and BES III upgrade

The presumed detector design is shown in Figure 2.7. The inner drift chamber replacement with the cylindrical GEM or Micromegas is under discussion. The PID detector, required for good particle identification should provide a better ($3-4\sigma$) π/K separation up to 2 GeV. The current implementation PID with multigap resistive plate chambers (MRPC) provides 2σ separation at energy up to 1.4 GeV [23].

2.5 High Intensity Electron-Positron Collider (HIEPA)

A new High Intensity Electron-Positron Collider (HIEPA) is proposed to be built in Hefei, China. To fully explore the τ - c physics program, including production of pairs of charm baryons, the energy range of the new facility will be extended. The centre-of-mass energy will vary between 2 and 7 GeV and luminosity up to few $\times 10^{35} \text{ cm}^{-2}\text{s}^{-1}$ will be achieved. In order to achieve this challenging luminosity large Piwinski angle and crab waste technique will be employed. Discussions of whether to design one or two polarized beams and whether to couple the HIEPA facility to the new performant light source are ongoing. The main parameters of this new accelerator are summarized in the Table 2.2.

The detector for HIEPA follows the traditional 4π detector design considerations. It comprises the inner pixel silicon detector (PXD), main gaseous tracker (drift chamber), particle identification time-of-flight system, electromagnetic calorimeter and muon detector 2.7. One of the main candidates for the endcap time-of-flight detector is the FTOF technology developed for the former SuperB project. The FTOF proposal for the HIEPA detector is jointly prepared by the team of Taras Shevchenko National University of Kyiv and Laboratoire de l'Accélérateur Linéaire.

Table 2.2: *Main parameters for HIEPA accelerator*

Beam energy (GeV)	1...3.5
Circumference (m)	992.8
Emittance (nm.rad)	10
Bunch length (mm)	10
Synchrotron losses per turn (MeV)	0.716
RF voltage (MV)	2.0
RF frequency (MHz)	500
Revolution frequency (MHz)	0.302
Number of bunches	540
Bunch current (mA)	5.0
Beam current (A)	2.7
SR power (MW)	1.93
Energy spread	8.12×10^{-4}
Luminosity ($cm^{-2}s^{-1}$)	1.05×10^{35}

2.6 Super c - τ Factory project (SCTF)

A project of the Super charm- τ factory (SCTF) [24] has been developed at the Budker Institute of Nuclear Physics (Novosibirsk, Russia). SCTF (Figure 2.8) is a symmetric electron-positron collider with a peak luminosity of $10^{35} cm^{-2}s^{-1}$ operating in the center-of-mass energy range between 2 and 5 GeV. Longitudinal polarization of electrons is foreseen at the beam interaction point.

The main goal of experiments at SCTF is a study of the processes with c quarks or τ leptons in the final state using data samples that are at least two orders of magnitude higher than those collected in the CLEOc [25] and BES III [26] experiments. The planned

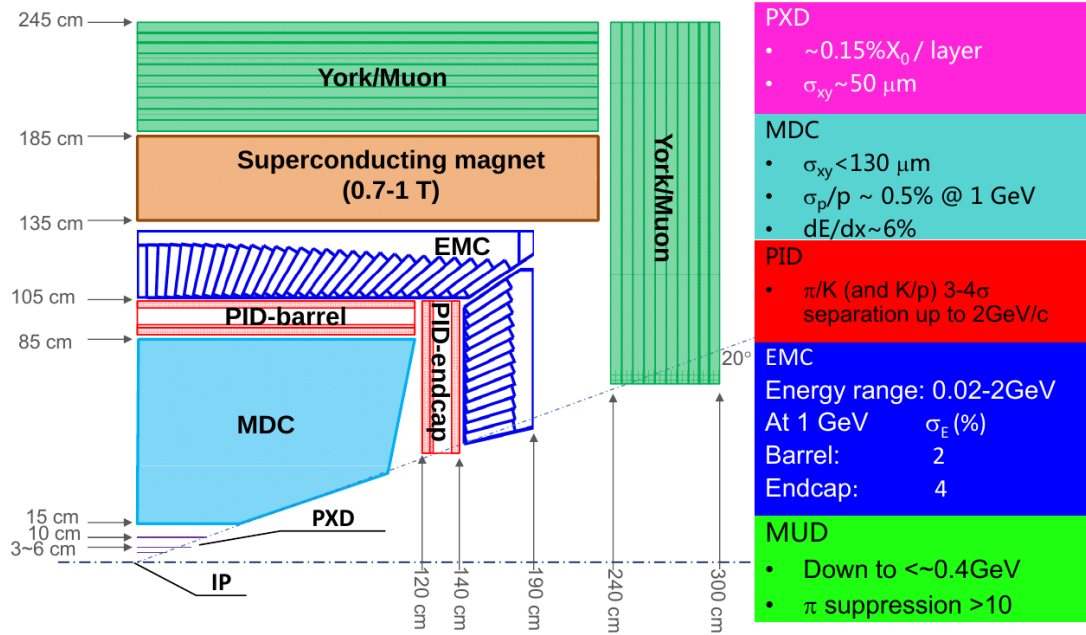


Figure 2.7: Schematic view of the HIEPA detector.

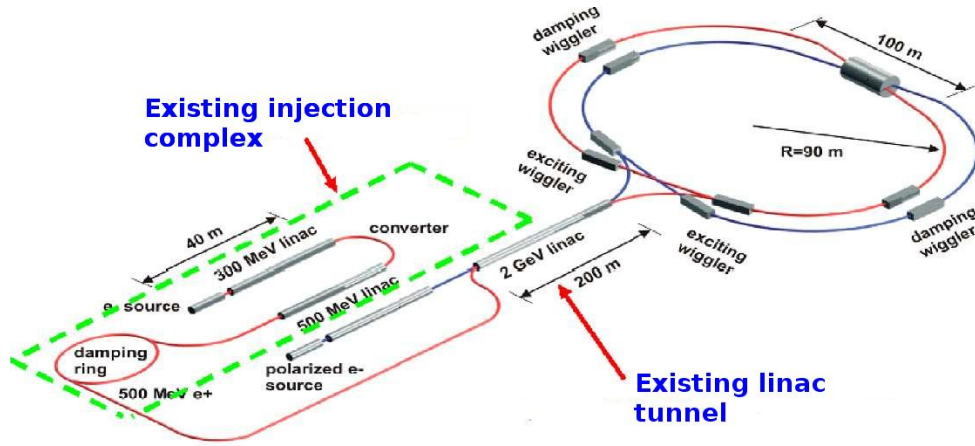


Figure 2.8: Layout of the future Super charm- τ factory (SCTF).

operation luminosity allows to collect approximately 10^9 τ leptons, 10^9 D mesons and a 10^{12} of J/ψ mesons. The total integrated luminosity planned to be collected at the Super charm- τ factory is 10 ab^{-1} . These data samples will allow a systematic study of all states of quarks of the two first generations (u, d, s and c) as well as searches for states of exotic nature.

Huge data samples of D mesons, charmed baryons and τ leptons will allow a search for principally new phenomena, such as CP violation in the D meson system and in τ

leptons as well as lepton flavor violation with high sensitivity.

The commissioning of the SCTF is planned to 2025–2026.

MICRO-PATTERN GASEOUS DETECTORS

As it was shown in Chapter 2, future high-energy physics experiments require large-area precise, fast, radiation-resistant and cost-effective tracking. Among the most promising solutions are those proposed within the class of micro-pattern gaseous detectors (MPGD). These detector technologies are rapidly evolving over the last decade.

This chapter aims at describing the current state-of-art in MPGD. For that, a brief history containing main principles of gaseous detectors operation is outlined. The main detector types and their characteristics evolution are mentioned. The description of MPGD breakthrough is given, mentioning new types of detectors which are gradually introduced into large high-energy physics experiments. Main challenges, their current solutions and limitations caused by them are also outlined.

3.1 Introduction

The history of tracking systems and in particular the gaseous detectors is very reach. Starting from invention of wire tube by H. Geiger in the beginning of 20th century till nowadays they are widely used in major particle physics experiments. The trackers played an important, sometimes decisive role in major discoveries. The Nobel prize has later been awarded for: cloud chamber (Wilson, 1927), photo-emulsions (Powell, 1950), bubble chamber (Glaser, 1960), multi-wire proportional chamber (Charpak, 1992).

Obviously the concepts and main characteristics of gaseous detectors have been evolved since they first were introduced. This chapter contains an overview of various gaseous detectors, their operating principle, main characteristics and challenges which have led to invention of new better concepts from the beginning till nowadays.

3.2 Electron passage in gas

When the ionizing particle interacts with the gas media, either ionization or excitation process takes place. In case of ionization an electron-ion pair is released, which may cause an avalanche, detected by the readout electronics. A number of important detector characteristics such as time and spatial resolution, gaseous amplification and its stability are defined by the electron propagation in gas media, so understanding of this process is essential to design a competitive fast detector.

In this section we will try to discover the mechanism of the electron transfer and multiplication in gas.

In the gaseous detectors R&D the following characteristics are the objects of primary interest: timing, spatial and energy resolution, detection efficiency, radiation hardness, gain homogeneity and stable operation regime. At the same time the fundamental feature of gaseous detectors is a signal amplification which should be high enough to provide a good signal to noise ratio.

The gas mixture composition defines many of important detector characteristics. The spatial resolution is defined by diffusion coefficient, timing - by electron drift velocity. The gas amplification is expressed in terms of the gain parameter which, is defined as the ratio between the number of electron-ion pairs created in the primary ionization process and the total number of electrons arriving at the anode. The gas gain measurement results as a function of the amplification field for different gas mixtures are shown in Figure 3.1 [27].

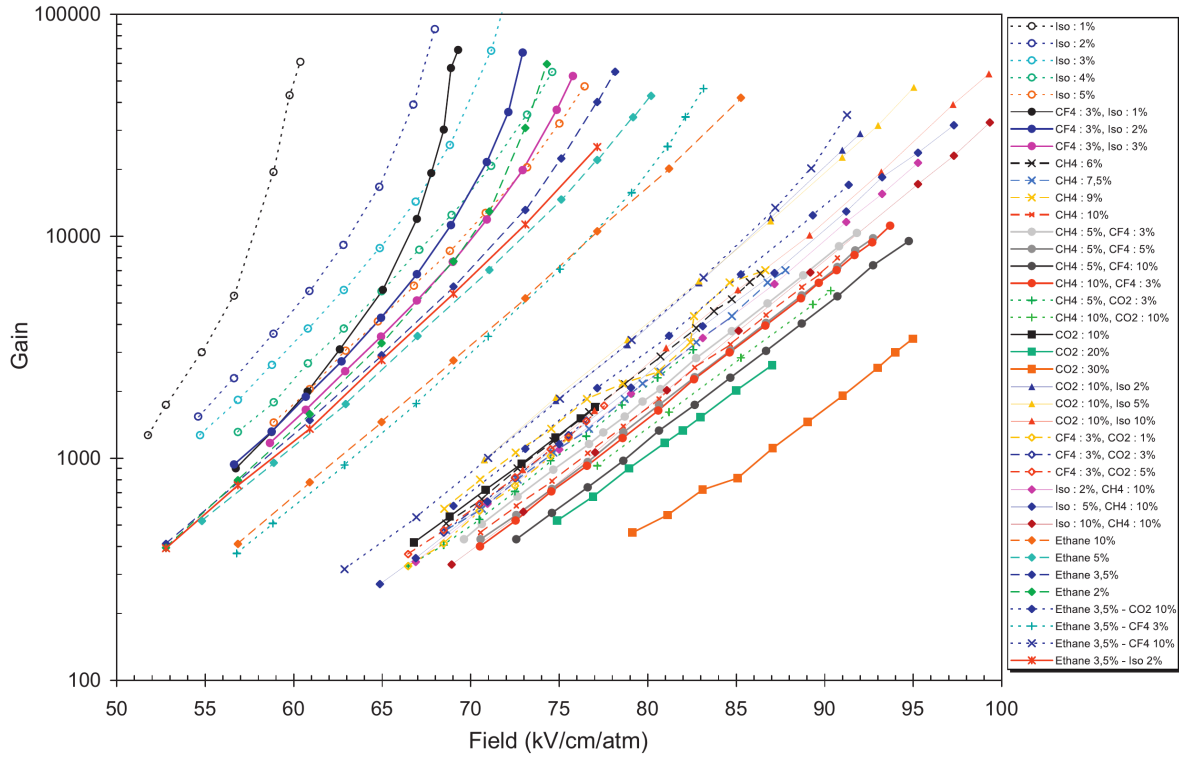


Figure 3.1: Gas gain measurement results of the Argon-based mixtures using the Micromegas detector with amplification region of $50 \mu\text{m}$ height [27].

3.2.1 Clusters and ionization process

When the ionizing particle passes through the gas media the primary ionization occurs and later secondary electrons are produced. The primary and secondary ionization in the gas are distinguished. Primary ionization is a process when the ionizing particle passes through the gas volume and produces the electron-ion pairs. More than one electron can be released in this process:



These electrons, in turn, can further ionize the gas if their kinetic energy is higher than the minimum ionization potential of the gas molecules. This process is called secondary ionization, and produce most of the charge along the track.

A set of the electrons produced in a single primary ionization collision, including all the subsequent secondary ionizations, is called the cluster [28]. So-called delta-rays or delta-electrons are the electrons with high kinetic energy that are produced in the primary ionization. The precise energy range definition for delta-electrons does not exist, but normally one means the kinetic energy of a few keV or higher [29]. The direction of delta-electrons can be estimated with a relation:

$$\cos^2\theta = \frac{E}{E_M}, \quad (3.3)$$

where E is the delta-electron energy and E_M is the energy of the primary ionizing particle. As one can see, for $E_M \gg E$ the direction of delta-electrons is perpendicular to the incident track.

Delta-electrons can travel up to several centimeters in the gas volume, further ionizing the gas. In MWPC or drift chambers with the readout strips or wires the electrons produced in primary and secondary ionizations are not distinguishable, resulting in a large amplitude signal. In the high granularity pixel-readout detectors the delta-electrons are visible as separate track or as dense regions in the frame so it is possible to reconstruct or filter them out.

3.2.2 Electron transfer

In this section, theoretical approaches to describe the gas transfer coefficients such as drift velocity and diffusion coefficients, are reviewed. The ionization collisions are neglected and will be taken into account in further sections, describing the electron multiplication process.

A simple approach based on the energy conservation [30] gives the following expressions for the drift velocity ω , diffusion coefficient D and component of the drift velocity perpendicular to the electric field ω_{\perp} :

$$\omega = \sqrt{\frac{2}{3} \cdot \sqrt{\frac{1}{3}\Lambda} \frac{eEl_e}{m}}, \quad (3.4)$$

$$D = \sqrt{\frac{2}{9\sqrt{3}\Lambda} \frac{eEl_e^3}{m}}, \quad (3.5)$$

$$\omega_{\perp} = \frac{1}{2\sqrt{3}} \frac{eB_{\perp}}{m} \sqrt{\Lambda} l_e, \quad (3.6)$$

where Λ is the mean fractional energy loss in a collision, and is a function of the electron energy; l_e is the mean free path for collision of the electrons with the gas molecules; E is an external electric field; B_{\perp} is magnetic field component perpendicular to the electric field; e and m are the charge and mass of electron. The Λ and l_e can be calculated from kinematics of electron collision with the gas molecules: $\Lambda = \frac{2m}{M}$ and $l_e = \frac{1}{n\sigma}$, where M is a mass of gas molecule, n is a concentration of gas molecules and σ is a collision cross-section. Any dependence Λ , l_e and σ on electron energy in this approach is omitted. The obtained results qualitatively describe the electron transfer parameters as a function of applied electromagnetic field [30].

More advanced approach is based on the conservation of number of electrons in the absence of ionization. The drift velocity w and diffusion coefficient D can be expressed as [31]:

$$\omega = \frac{2eE}{3m} \left\langle \frac{l}{v} \right\rangle + \frac{1eE}{3m} \left\langle \frac{dl}{dv} \right\rangle, \quad (3.7)$$

$$D = \frac{1}{3} \langle lv \rangle. \quad (3.8)$$

To calculate the averages in the coefficient expressions the electron distribution function in the phase space $f(\vec{r}, \vec{v}, t)$ needs to be known. It can be estimated from the Boltzmann equation, which can be solved analytically with some approximations or solved numerically. Among different approaches [30–35], the following expression is considered as a representation of a general theory of electrons in gases [31]:

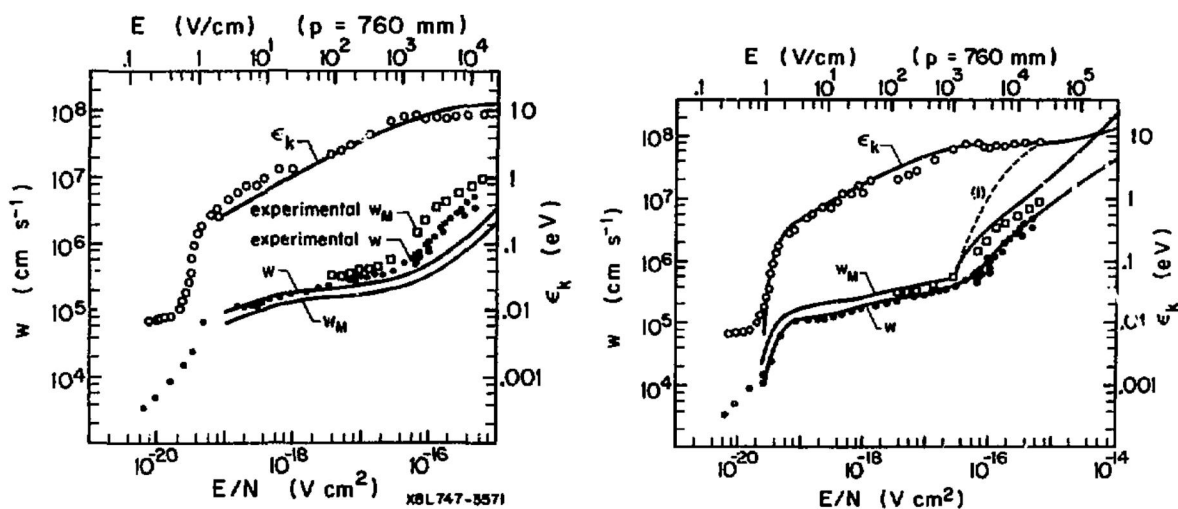
$$F(\epsilon) = C\sqrt{\epsilon} \exp\left(-\int_0^{\epsilon} \frac{3\Lambda(\epsilon)\epsilon d\epsilon}{[eEl(\epsilon)]^2}\right) \quad (3.9)$$

where C is normalization constant, $\int_0^{\infty} F(\epsilon)d\epsilon = 1$. This gives the following expressions for the drift velocity and diffusion coefficient:

$$\omega = \frac{\sqrt{2/m}}{eE} \int_0^{\infty} \frac{\Lambda(\epsilon)}{l(\epsilon)} \epsilon^{3/2} F(\epsilon) d\epsilon, \quad (3.10)$$

$$D = \frac{1}{3} \sqrt{\frac{2}{m}} \int_0^{\infty} \sqrt{\epsilon} l(\epsilon) F(\epsilon) d\epsilon. \quad (3.11)$$

After taking into account the cross-section data and $\Lambda(\epsilon)$ dependence (which can be taken as $\frac{2m}{M}$ in zero approximation) one can calculate the transfer coefficients. Results of the application of the analytical expressions to Argon are shown in Figure 3.2(a) [31].



(a) Analytical approach.

(b) Numerical approach.

Figure 3.2: Calculation results of electrons drift velocity in Argon [31].

The numerical approach does not require any approximations to the Boltzmann equation on the distribution function, giving more accurate results (Figure 3.2(b)) [31]. Thus it dominates nowadays when computing resources are available. More details and corresponding software can be found elsewhere [31, 35–37]. The most common software widely used for recent developments is Magboltz [38], the calculation results for several gas mixtures are presented in Figure 3.3 [39]

3.2.3 Multiplication process

When colliding above the threshold of inelastic collisions, the electron interaction with the gas molecules leads either to excitation or ionization. In case of ionization the secondary electron is produced and accelerated by the electric field, eventually ionizing another molecule. This is an avalanche process which is fundamental for all gaseous detectors and takes place in strong electric fields. The size of electron avalanche initiated by a single electron produced in a primary ionization collision is called a gas gain. Modern gaseous detectors operate at gain values of about $10^3 - 10^5$.

The gas multiplication process is characterized by a number of ionizations per unit length, so-called Townsend coefficient. A common parametrization for the Townsend coefficient [40] suggests its dependence on electric field E and gas pressure P :

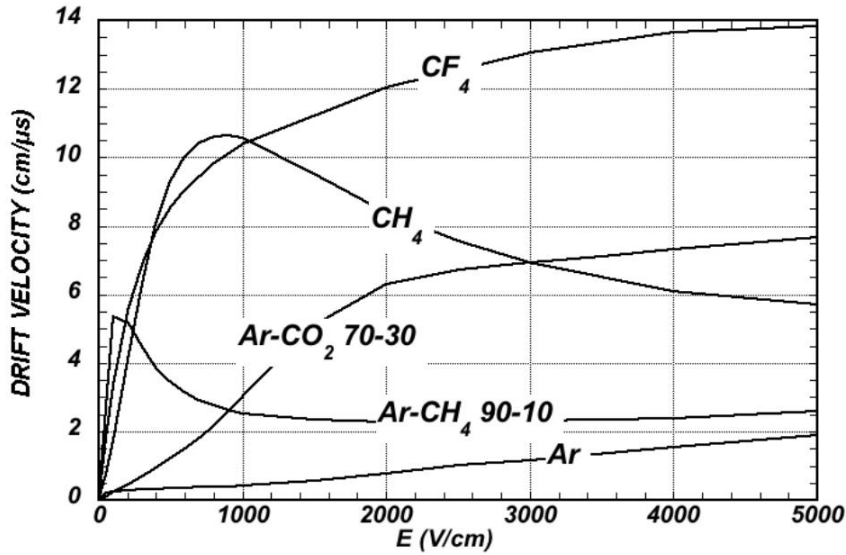


Figure 3.3: Drift velocity for several gas mixtures calculated with MAGBOLTZ software [38].

$$\alpha = AP \exp -B \frac{P}{E} \sqrt{\epsilon} l(\epsilon) F(\epsilon) d\epsilon. \quad (3.12)$$

This parametrization is applicable for electric fields up to about 50 kV/cm.

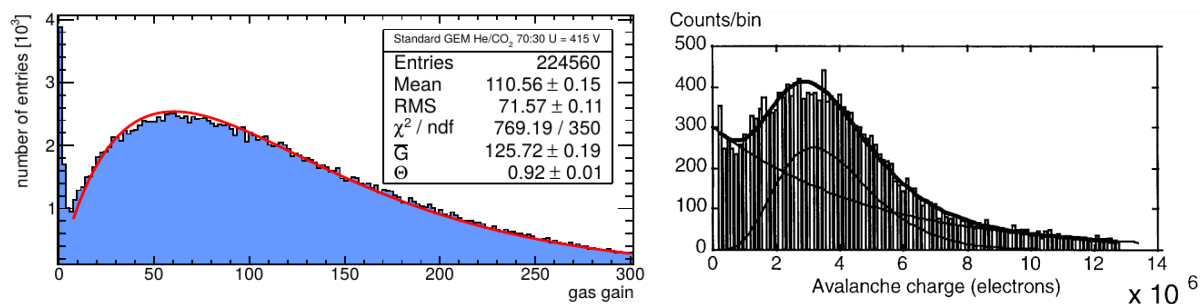
3.2.4 Gas gain variations

The gas gain in all typical detectors follows the broad spectrum, in most cases described by Polya distribution [41]. Examples of the Polya distribution fit for simulation and experimental data are shown in Figure 3.4.

This fact has two important consequences. First, gain variations directly imply the detector signal charge, thus distorting the deposited energy measurement. Second, a long tail of the distribution represents a probability of very strong discharges, which may damage the detector. Therefore, an average detector operation gain is limited by discharge probability. In many cases an additional electrode protection is introduced to detector design to ensure a high radiation resistance [43].

Raether limit

When the size of the avalanche created in electron multiplication process in gas becomes sufficiently large, it may cause a streamer. If the streamer reaches the anode, the detector electrodes are connected by a conductive path and the detector capacity discharges, dam-



(a) GEM detector filled by the He/CO₂ 70/30 gas gain distribution (simulation) [28].

(b) Polya fit of the pulse height spectra obtained with the parallel-plate chamber filled by the Ar/iC₄H₁₀ 90/10 gas mixture [42].

Figure 3.4: Simulation and experimental results of gas gain fluctuation measurements.

aging the detector. An empirical limit of 10^8 electron avalanche size when the discharge is still not produced is called a Raether limit [44].

3.3 Wire tube

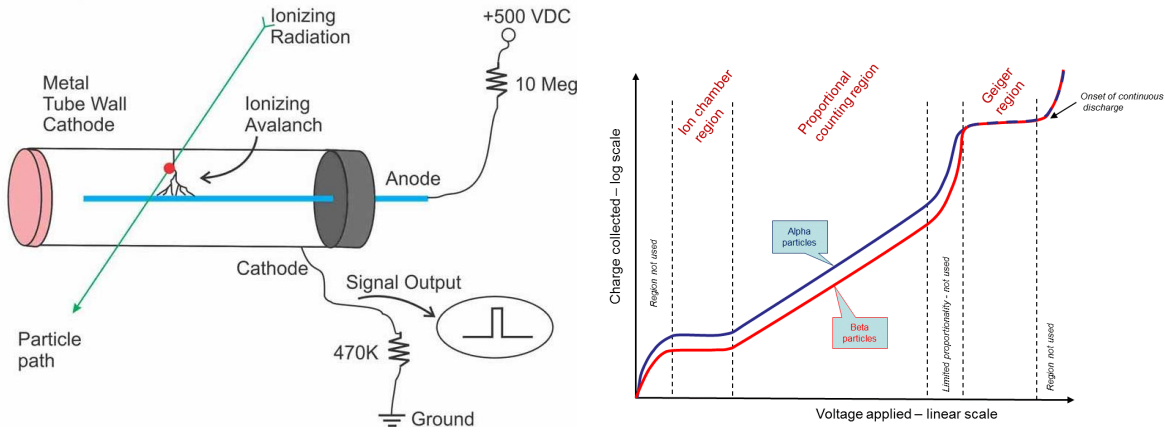
Described in 1908 by Hans Geiger [45] it took 20 years before the first gaseous detector was introduced [46] by Hans Geiger and Walther Muller. Despite the fact that the wire tubes were replaced by their successors in majority of their primary applications, the main operation principles of all gaseous detectors can be illustrated by this detector.

3.3.1 Operating principle

The wire tube (Geiger-Muller tube) consists of a pair of electrodes with high voltage across them surrounded by a gas. The most common configuration is cylindric with the cathode shield and anode wire stretched along the central axis (Fig. 3.5(a)).

When the ionizing particle enters the gas volume it can produce the electron-ion pair. The ions (and electrons) are attracted to opposite electrodes, which under action of electric field, are accelerated. They further ionize the gas molecules, resulting in an avalanche close to the anode wire, which produces an electric current. Reading the signal from the electrodes the information about the primary ionizing particle can be obtained. The type of this information is defined by the mode of wire tube operation.

Possible modes of operation are described by a classical dependence of collected charge (gas amplification factor) on the voltage applied between the electrodes (Fig. 3.5(b)).



(a) Principle of wire tube operation.

(b) Collected charge by wire tube from a single ionization dependence on the voltage applied between electrodes.

Figure 3.5: *Illustration of wire tube operation principle.*

At low voltages the recombination of electron-ion pairs is observed, which partially suppresses the effect of primary ionization. It is impossible to determine the fraction of primary charge that has been detected, so this mode has no practical applications.

Increasing the voltage the wire tube enters the so-called ionisation chamber region, where all primary charge is collected. There is no gas amplification yet.

Applying higher voltages results in avalanche creation, which size grows exponentially. The avalanche size, and thus, collected charge, grows proportionally to the primary charge. This region is called proportional and can be used to obtain the energy loss in the detector volume by measuring the pulse amplitude at the electrodes.

At higher voltages the collected charge growth becomes stronger; the dependence on the initial charge disappears. At a given voltage the detector enters the Geiger mode, where the detected charge does not depend on applied voltage and primary ionization. In this mode, the detector operates Each primary ionization produces an avalanche, which propagates to and later along the anode wire in a strong electric field. Amplification in this region is typically 10^8 - 10^{10} .

Higher voltages result in glow discharges, which sustain constantly, while the detector becomes insensible to ionizing radiation.

3.4 Multi Wire Proportional Chamber

In the first half of 20th century the only option to construct a gaseous tracker was to assemble a stack of wire tubes, which was difficult to implement mechanically. Such a device has a spatial resolution limited by the tube diameter which is in order of cm. The idea to place many wires in a single gas volume appeared much earlier, before the first multiwire chambers were constructed. However, the issue of coupling capacitance between adjacent sensitive wires has been shifting the invention for years.

The main advantage of multiwire gaseous detector over all previously known trackers is the automatic signal readout. At most trackers of that time of sub-mm spatial resolution (bubble chambers, photoemulsions) tracks of particles were recorded in photographs. Therefore, the data processing required a lot of hard routine handwork.

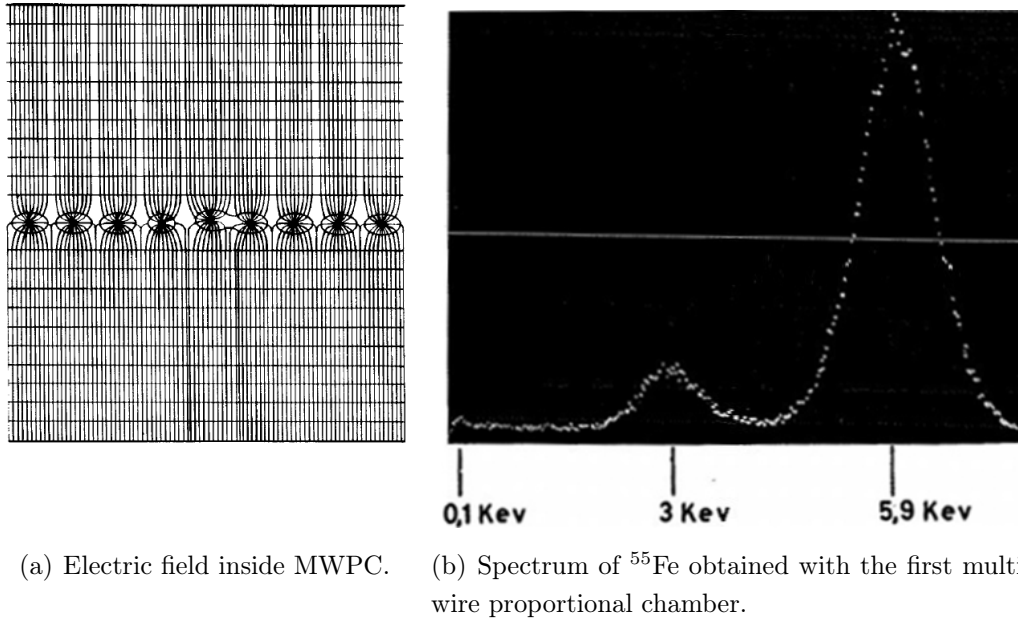


Figure 3.6: *The MWPC field configuration and spectrum of ^{55}Fe .*

First successfully operated multiwire proportional chamber (MWPC) was described by Georges Charpak [47] in 1968. The time resolution of $0.4 \mu\text{s}$, counting rate of 10^5 particles per wire, detection efficiency close to 100% and 15% of energy resolution at 5.9 keV X-rays from ^{55}Fe radioactive source (Fig. 3.6(b)) were achieved.

The layout configuration of the MWPC is shown in Fig. 3.6(a). A stack of parallel anode wires is positioned between two cathode planes. The detector acts almost as independent proportional counters (down to separation between wires of about 1 mm

[47]). The position of primary particle's interaction along the track is determined by the center-of-gravity method taking into account induced charge from each anode. Making the cathode plane as a series of segmented strips at the same potential and reading the ions signal allows to determine the 2nd coordinate of the interaction point. A typical spatial resolution of MWPC is about $600 \mu\text{m}$.

This invention triggered a development of a new family of tracking detectors - multiwire gaseous trackers, including later concepts of drift and time-projection chambers.

3.5 Drift chamber

In the drift chamber the anode and the cathode wires are enclosed between field-forming electrodes (Figure 3.7). Thus the electron avalanche from a single interaction is collected on the nearest sensitive wire. The coordinate of interaction can then be calculated by a measurement of time from the moment of primary interaction, provided by an external trigger, to the moment of signal detection by the readout electronics.

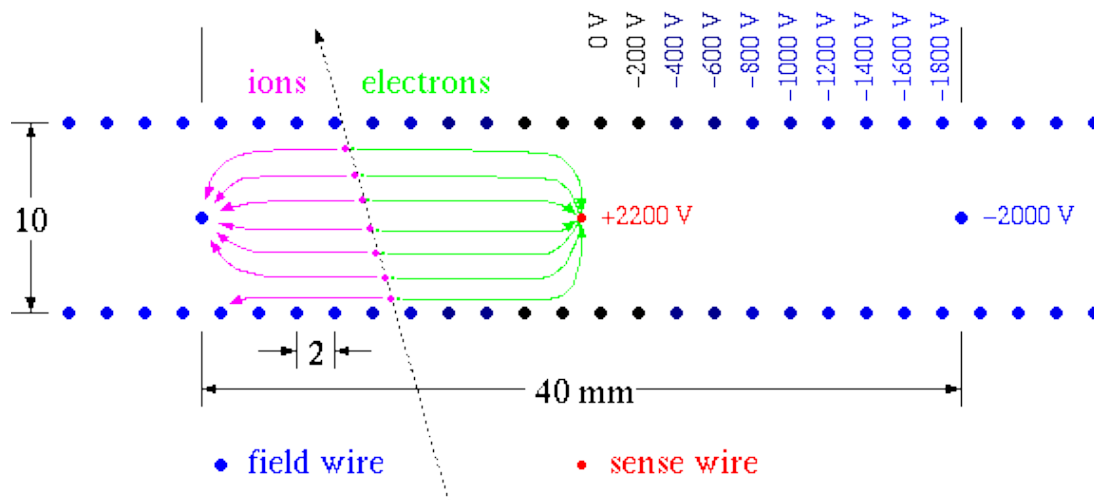


Figure 3.7: Geometry and typical field configuration of the drift chamber.

A big advantage of the drift chamber over the MWPC is significantly reduced number of sensitive wires, and at the same time an improved spatial resolution [48]. A slow dependence of the spatial resolution as a function of the drift distance (Figure 3.8) enabled a construction of the large area (up to 16 m^2 [49]) drift chambers with an average resolution of about $200 \mu\text{m}$. On the other hand with the small drift chambers of $10 \times 10 \text{ cm}^2$ the resolutions of about $20 \mu\text{m}$ were achieved [50].

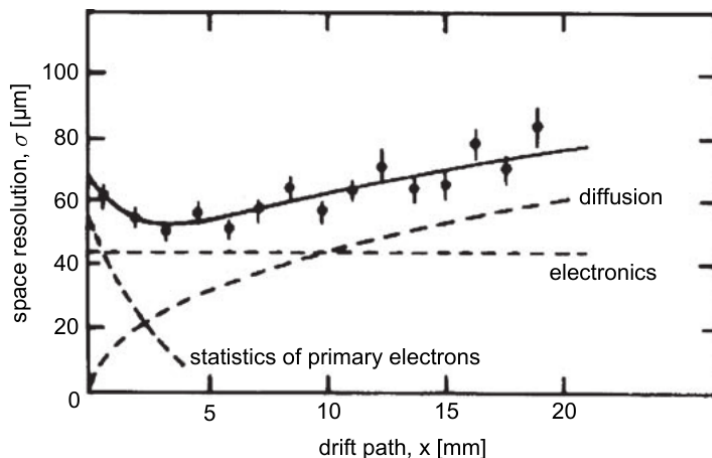


Figure 3.8: *Drift chamber spatial resolution as a function of the drift distance* [51].

Coordinate measurements along the sensitive wire can be done by measuring the difference in arrival time, the pulse amplitudes at the two ends or stacking several modules together at an optimal angle between their wires. Typical values are 3-10 times worse than the resolution along the electric field.

The rate capability directly depends on the size of the chamber since the sensitive wire detection rate should be maintained at low level for the nominal chamber operation. In general, the rate is about 10^7 particles per second.

3.6 Time projection chamber

The time projection chamber (TPC) uses a similar concept as the drift chamber. It consists of a large drift region and the highly segmented anode producing the 2D projection of the track (Figure 3.9). The 3rd interaction point coordinate is determined by measuring the drift time to the anode giving the 3D track pattern. A homogeneous electric field in TPC is provided by the electrode strips around the field cage. Such concept allows a construction of large volume TPCs of several 10 m^3 .

Large TPC volume makes it an attractive tracker for the large collider experiments. In this case the cylindrical TPC is divided in two parts by the central cathode, having two anodes at the sides. The magnetic field is often applied in parallel to the electric field, primarily, to separate particles with different momenta. This also reduces the electron diffusion (Figure 6.3). The typical TPC spatial resolution is about $\sigma_{r\phi} \sim 200 - 400 \mu\text{m}$ and $\sigma_z \sim 1 \text{ mm}$. Before the micro-pattern gaseous detectors were introduced the MWPC

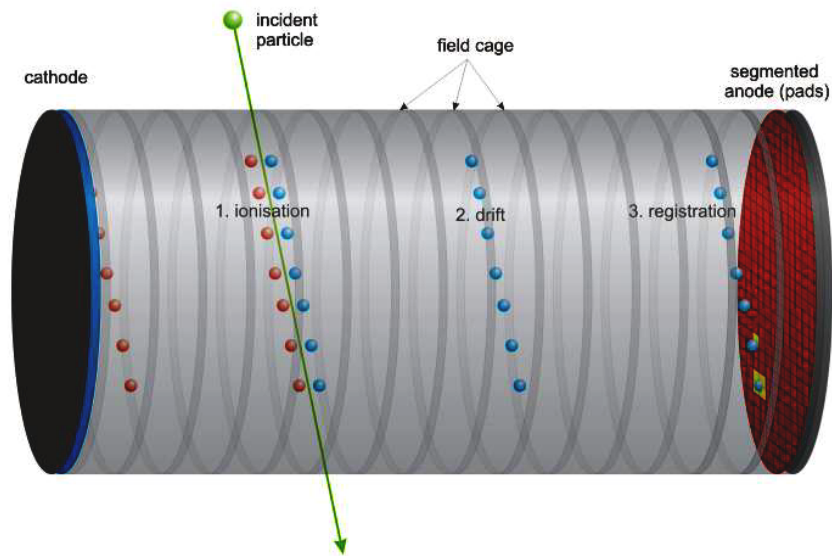


Figure 3.9: Time projection chamber principle of operation. 1 - an incident particle ionizes the gas media producing electron (blue) - ion (red) pairs. 2 - electrons are drifting to the anode in homogeneous electric field. 3 - electrons hit the segmented anode, forming the 2D projection of the track.

have been widely used as the anodes for TPC.

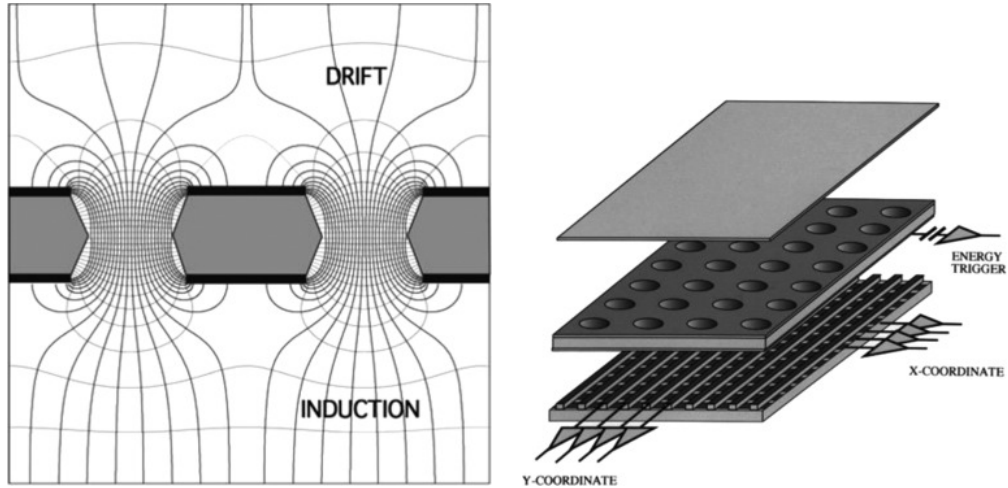
3.7 Micro Pattern Gaseous Detectors

With the photolithographic technologies development of a new concept of gaseous detectors was introduced, named micro-pattern gaseous detectors (MPGD) with a typical size of amplification structure of about $50 - 200 \mu\text{m}$. To date a variety of detectors with different electrodes geometries have been proposed [52–56]. Two most successful configurations are the Gas Electron Multiplier (GEM) [54] and the Micro-mesh gaseous detector (Micromegas) [55].

Along with the enhanced spatial resolution and timing characteristics the GEM and the Micromegas have much wider dynamic range than the MWPC and drift chamber, providing the gain stability at higher radiation loads.

3.7.1 GEM

The Gas Electron Multiplier (GEM) [54, 57] represents an insulating plate with the electrodes at both sides of it. The holes of equal diameter are chemically etched through the plate on the equal distance from each other. Applying the proper voltages to the electrodes the electric field configuration shown in the Fig. 3.10(a) is achieved, providing the dense field regions in the holes volume, where the electrons multiplication occurs.



(a) Electric field inside GEM.

(b) Geometry configuration for single GEM detector.

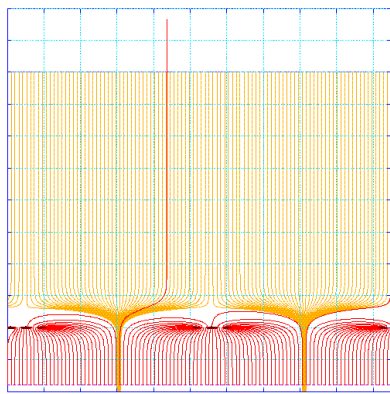
Figure 3.10: *Gas Electron Multiplier (GEM).*

Above and below the GEM plate the electric field provides no gas amplification. These

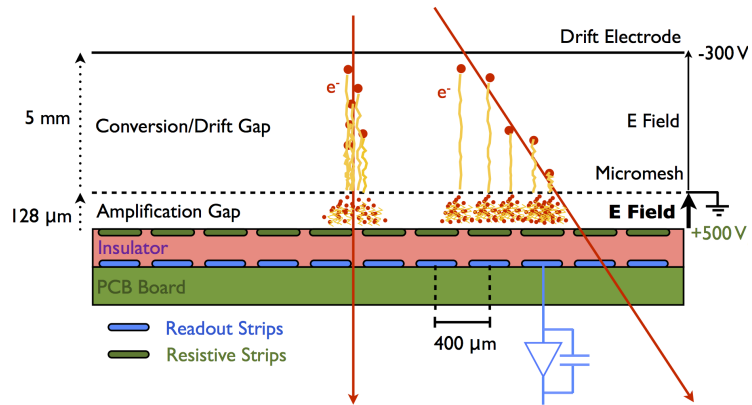
are the regions, where electrons drift to the electrode. Due to small hole diameters (typically between $25\ \mu\text{m}$ and $150\ \mu\text{m}$) and distance between adjacent holes (between $50\ \mu\text{m}$ and $200\ \mu\text{m}$) the primary electron passing through the GEM hole is well localized, providing a good spatial resolution. The typical thickness of the GEM plate is about $50\ \mu\text{m}$ so the field in the hole volume is non-homogeneous. For double or triple only 50-60% of electrons after amplification drifts to the subsequent electrodes due to the field defocusing at the exit of the hole. A typical value of gain achieved with a single GEM plate (Fig. 3.10(b)) is about 10-20 times, so that several GEM plates (up to 4) can be placed on top of each other, providing gains of about 10^4 [58].

3.7.2 Micromegas

The micro-mesh gaseous structure (Micromegas) [55] is a detector consisting of a drift region and a thin ($25\text{--}150\ \mu\text{m}$) amplification gap, separated with a conducting mesh with homogeneously placed holes of the same size (Fig. 3.11(b)). The field map is shown in the Fig. 3.11(a). Due to the field lines compression to the holes the primary electrons pass the mesh, enter the amplification region and create avalanches, registered at the anode.



(a) Electric field inside Micromegas.



(b) Principle of Micromegas detector operation.

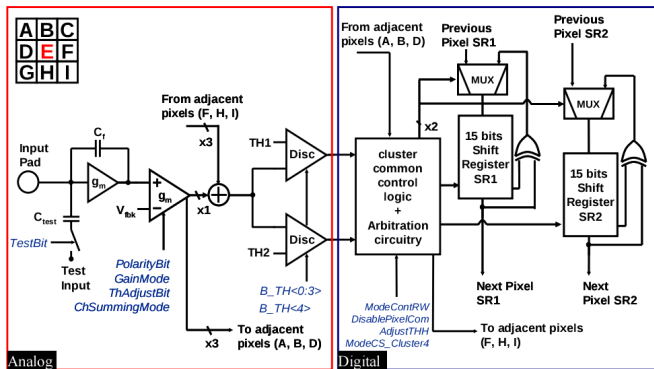
Figure 3.11: *Micromegas operation principle.*

Typical electric field values in the drift and amplification regions are about $1\ \text{kV}/\text{cm}$ and $50\text{--}70\ \text{kV}/\text{cm}$, respectively. The field spatial configuration is shown in Fig. 3.11(a), indicating a good homogeneity in both regions. Transverse spatial resolution highly depends on the detector configuration, and especially on the drift region height. Resolution

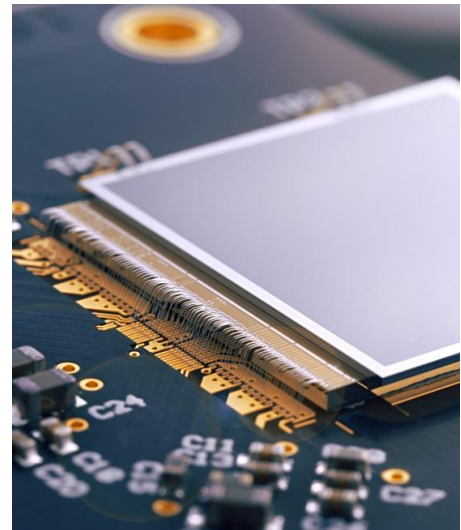
down to $12 \mu\text{m}$ has been achieved for MIPs, limited by the micro-mesh pitch.

3.7.3 Timepix

Among others implementations [59–61] the dedicated pixel readout chip Medipix2 [62], later evolved into Timepix [63] and Timepix3 [64] chips (Figure 3.12), is used as a standard anode readout for Micromegas/InGrid detector (Section 3.7.4). It consists of 65536 (an array of 256×256) pixels each of the size of $55 \mu\text{m}^2$, while the dimensions of active area are of $14.08 \times 14.08 \text{ mm}^2$. Each pixel represents a pad connected to the charge sensitive preamplifier followed by the digital section (Figure 3.12(a)). The layout of a single Timepix cell is shown in Figure 3.13. The sensitive part of the pixel is represented by a yellow octagon.



(a) Schematic of a Timepix cell circuitry.



(b) The Timepix chip bonded on the PCB.

Figure 3.12: *The Timepix chip.*

The digital part for each pixel uses an external clock of 100 MHz maximum frequency and contains a single-level discriminator and 14-bit counter shift register. This register has a dynamic range of 11810 counts and provides the information about the detected signal which depends on the configuration mode. The pixels of the chip are enabled only while the so-called shutter window is open. Its length is configured externally and can consist of up to 11810 periods of the clock signal.

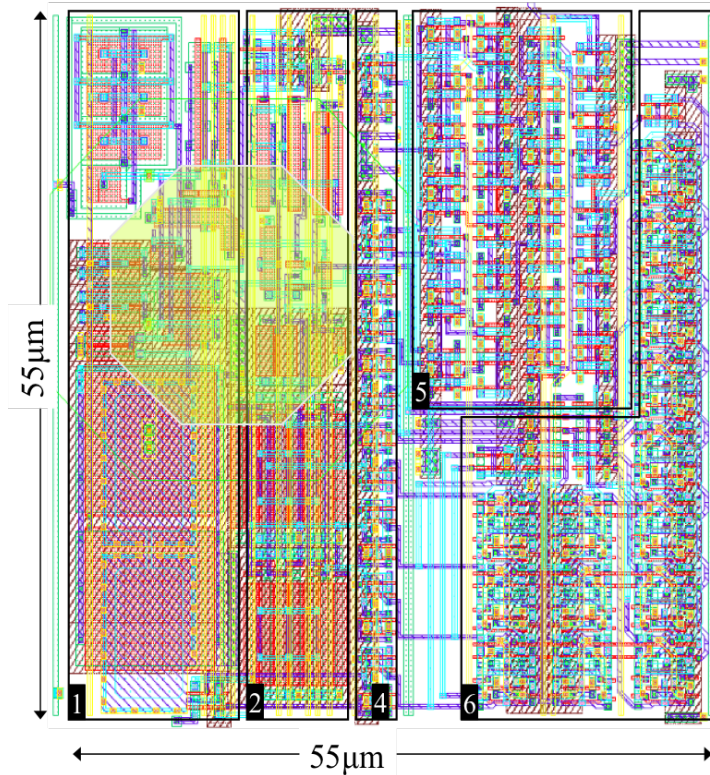


Figure 3.13: *Timepix cell layout. Different parts of cell schematic are shown: charge sensitive preamplifier (1), threshold discriminator (2), 8-bit configuration register (4), synchronization logic (5) and 14-bit counter shift register (6).*

Four operation modes (Figure 3.14) are available and can be set via the pixel configuration register:

- Counting mode: also known as Medipix mode. The counter is incremented only once when the signal crosses the discriminator threshold. Thus the number of signals above the threshold during the shutter time is counted.
- Time over threshold (TOT) mode: the counter is incremented while the signal level is above the discriminator threshold. Taking into account a possibility to calibrate this time to the input charge, the TOT mode allows a signal charge measurement. Times from all signals within a single shutter period are summed.
- Time mode: also known as time of arrival (TOA) mode. The counter is incremented from the first threshold crossing until the end of the shutter time. Since the shutter time is known, the counter value represents the signal arrival time.

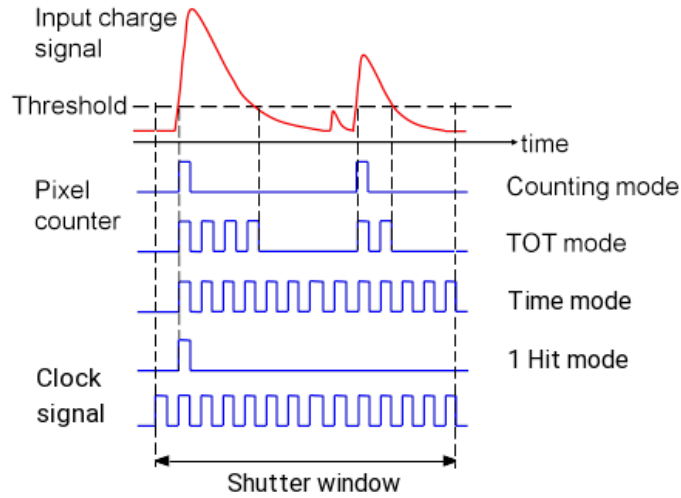


Figure 3.14: *Illustration of the Timepix pixel operation modes.*

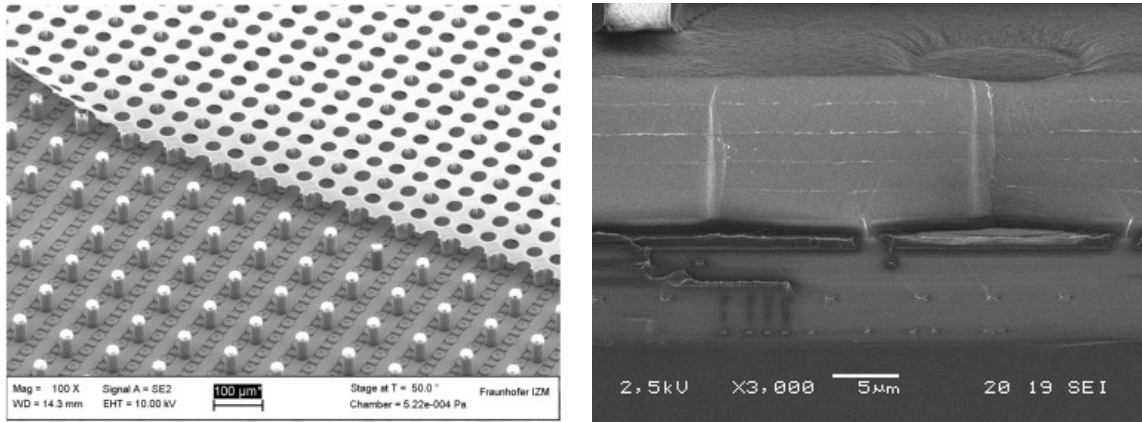
- One hit mode: the counter register is incremented once within the shutter time if a signal crosses the discriminator threshold.

The Timepix3 chip is available since 2013. It is capable to perform the TOT and TOA measurements simultaneously, which provides a unique possibility to detect the tracks via 3D measurements along with the corresponding deposited energy using a compact detector.

3.7.4 Micromegas/InGrid

The Micromegas-like type of detectors with the highly pixelated ASIC anode readout and the mesh produced directly on top of the anode using microfabrication technique [65] is called InGrid which stands for Integrated Grid.

With the photolithography development a competence to produce the gaseous-detector amplification structures of μm size has been developed. However in many cases the signal readout is performed either by strips [66] or by mm-size pads [67]. The capability to construct a corresponding μm size pixelated readout would provide a detector which resolves individual electrons produced in primary ionization collisions. Because of the electron diffusion in the detector drift region, the spatial resolution of gaseous detectors is limited to a few tenth of μm , which defines the order of the pixel size. This value, however, approaches typical spatial resolution of the silicon tracking systems [68], also taking an advantage of large sensitive volume, low-density detector media, better radiation hardness and lower detector cost.



(a) InGrid mesh produced on top of the Timepix3 protection layer. (b) Cross-section of the InGrid protection layers. Five layers and sensitive pad connection are shown.

Figure 3.15: Illustration of the Micromegas/InGrid mesh (a) and protection layers (b) fabrication process.

The pure ASIC is sensible to signals above $500e^-$ so it cannot be directly used as a standalone detector in gaseous media. A corresponding electron multiplication can be ensured with the MPGD amplification structures. Aiming at achieving ultimate spatial resolution with a high granularity pixel anode, the corresponding Micromegas-like grid is an attractive choice to accomplish the detector design. A small height between the mesh and the anode can be adjusted in order to keep the transverse electron multiplication avalanche size within a single pixel.

The measurements with the GEM structures and the Timepix readout have also been performed and can be found in Refs. [69, 70]. The detailed information on InGrid fabrication process and characterization of the detector can be found in Ref. [71].

Discharge protection

Due to the nature of the gas amplification strong avalanches causing the discharge may occur at any average gain value (Figure 3.4). Thus, the InGrid readout pads can be damaged and become insensitive.

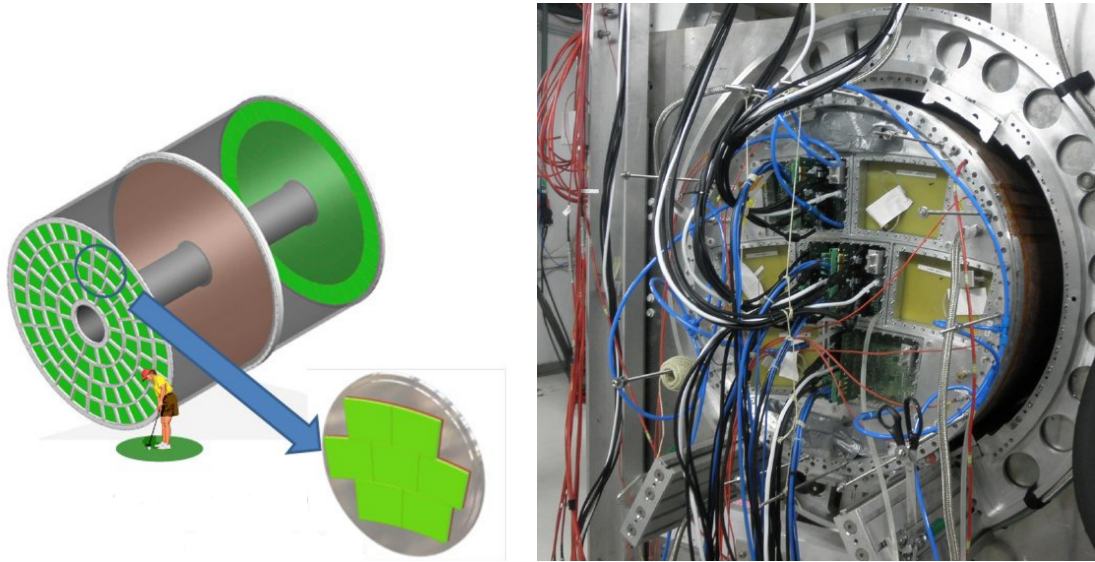
To avoid this the Timepix pads are covered by multiple protection layers, so-called SiProt (silicon protection) layers. The Figure 3.15(b) demonstrates the cross-section of the 5 layers above the chip surface and the readout pad, connected to the Timepix pixel. The protection layer is always a compromise between the detector damage probability and

a quality of the signal readout. Thus, too thick protection layer will spread the incoming charge to the adjacent pads, reducing the InGrid spatial resolution. An optimization of the layer thickness can be performed related to the InGrid functioning environment and average flux. Typical values are from 4 to 20 μm . The detailed study on the InGrid discharge protection can be found in Ref. [43].

Large area Micromegas/InGrid

The real challenge is to produce a large-area Micromegas/InGrid detector, which requires a lot of chips synchronously operating. Design steps towards anode plane with multiple chips were the quad-module (4 chips) [72] and octoboard (8 chips) [73] modules. A great boost for the InGrid technology comes from the fact that it is one of the three possible design options for the TPC readout at the ILD [17], which is the first InGrid large-scale application.

In order to cover two endcaps of the TPC, 50-60 thousands of Timepix chips (depending on the chips arrangement) are required. In order to make the prototype development possible, a large system, containing 7 TPC modules was built at DESY (Figure 3.16) [74].



(a) Endcap of TPC at ILD and large prototype schematic view.

(b) Three 96-chips modules installed at the large prototype at DESY for the testbeam [75]

Figure 3.16: *The ILD large prototype at DESY, Hamburg.*

The main scalability challenges with large-area Micromegas/InGrid setup are the syn-

chronization of many chips thresholds (to ensure the same sensitivity and noise reduction), the power dissipation (a water cooling is required), and large data signal readout. From the detector side the dead regions cannot be eliminated since an additional space is required to connect the chips to the PCB (Figure 3.12(b)). The layout of the currently used ILC TPC modules is shown in Figure 3.17, while examples of the suggestions to reduce the dead area are presented in Figure 3.18.

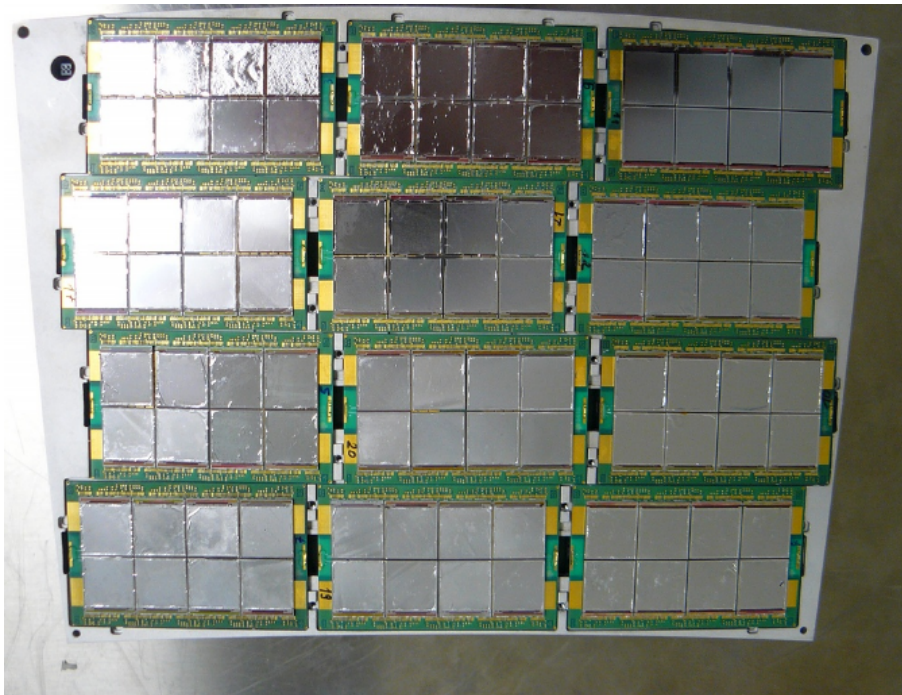


Figure 3.17: *InGrid* TPC module for ILD designed in Bonn [76].

A great prove-of-concept work was done by M. Lupberger [76], presenting a scalable Micromegas/*InGrid* readout system and summarizing results from the test beam at large prototype with 3 modules containing 160 chips in total, which is the largest investigated *InGrid* setup to date [78].

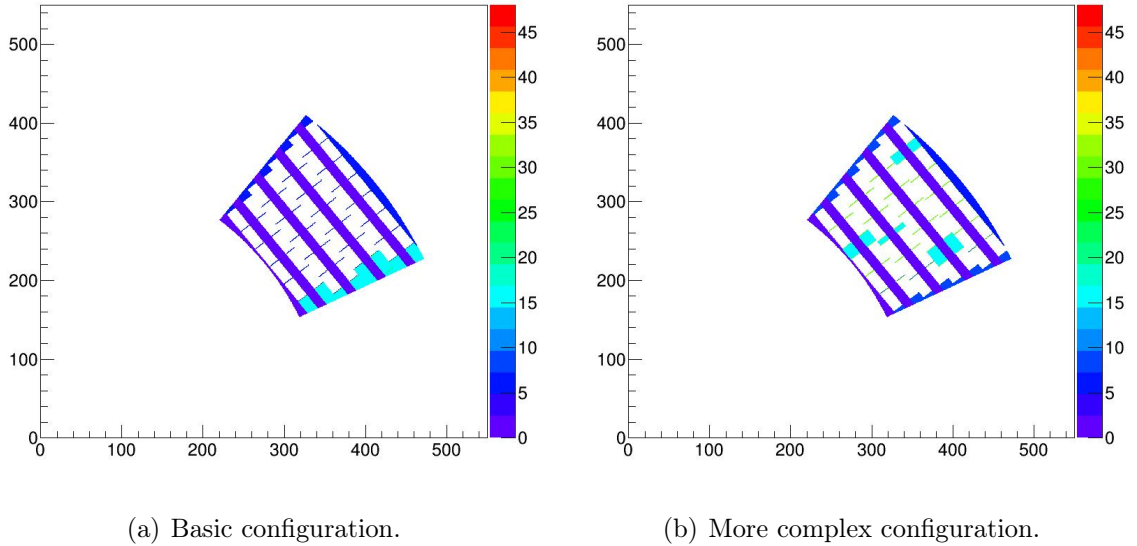


Figure 3.18: *In order to increase the detector sensitive area a Timepix chips configuration is being optimized for the new ILD TPC module [77]. The empty regions caused by chips connection are shown in purple, while the light blue regions indicate empty regions left after filling the module with chips according to a given algorithm. Two options are shown: where empty regions allowed only at the side of the module (a) and where the empty region area is minimized (b).*

LEETECH SPECTROMETER

As outlined in Chapter 3, the development of novel MPGD requires performance test facilities. Among the test facilities briefly reviewed in this chapter electron beams with different energies take a central place.

Within a present thesis a new test beam facility LEETECH (Low Energy Electron TECHnique) was built as an extension of PHIL accelerator at LAL (Orsay). This section describes the creation steps - simulation, design, manufacturing and commissioning. Providing a possibility of flexible adjustment of electron beam energy and intensity, operating in energy range up to a 5 MeV (upper boundary is defined by currently used PHIL photocathode), LEETECH fills the gap between larger and more expensive test beams and non-monochromatic radioactive source with a defined energy spectrum. Also a very short time width of PHIL beam bunches provides unique time characteristics of LEETECH facility.

The commissioning process and facility characterization is presented and a mode of single-electron beam is described in this chapter.

4.1 Introduction

An important detectors tests discussed below as well as a validation of the technique that allows to deliver samples of electrons with adjustable energy and multiplicity using a versatile LEETECH platform was performed with electrons from the PHIL accelerator.

4.2 PHIL - Photoinjector at LAL

The PHIL (PHotoInjector at LAL) [79] is an electron beam accelerator at LAL. This accelerator is designed for tests and characterization of the electron photoguns and high frequency structures for future accelerator projects (lepton colliders of the next generation — CLIC, ILC). This machine produces electron bunches of low energy ($E < 10$ MeV) with small emittance $\epsilon \approx 10\pi \cdot mm \cdot mrad$, high current (charge of up to 2 nC/bunch, duration < 10 ps) electron bunch at low repetition frequency (< 10 Hz). At the end of the accelerator, the normalized emittance is about $4\pi \cdot mm \cdot mrad$. Bunch length is determined by laser pulses having FWHM duration of 5 ps. PHIL is currently a 6-meters long accelerator with two extracted beam lines. The PHIL accelerator design is illustrated by Figures 4.1 and 4.2.

The electron beam is initiated by a laser pulse. The beam is then transported by a system of solenoid magnets to downstream the direct or the deviated line. Further beam instrumentation serves to ensure and monitor the beam quality and to characterize the beam performance.

Four solenoid magnets are installed along the beamline to adjust the beam trajectory: B1, B3, B5 and B7. The B5 solenoid is located 2.1 m downstream the photocathode, in the middle of the beamline.

The B1 solenoid is used to cancel the magnetic field on the photocathode, which is non-zero when B3 is activated, otherwise this non-zero magnetic field would induce an increase of the initial bunch transverse emittance. The B3 solenoid is located 14 cm downstream the photocathode, just at the RF-gun exit. The B3 can be used either to transversely focus the electron bunch, in order to transport it without losses, or to optimize the bunch transverse emittance at the RF-gun exit by the emittance compensation process. The B5 is used only to transversely focus the electron bunch, in order to transport it without losses [80].

The direct beam line is mainly dedicated to the 2D transverse emittance and bunch length measurement. The deviated line is devoted to the measurements of the beam

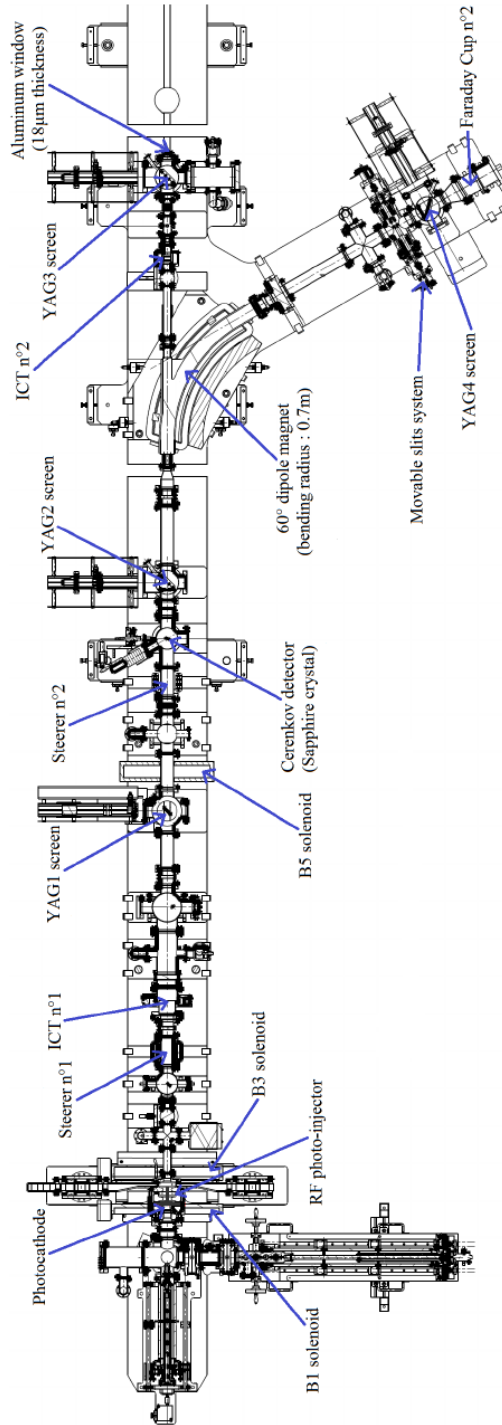


Figure 4.1: 2D view of the PHIL accelerator [80].

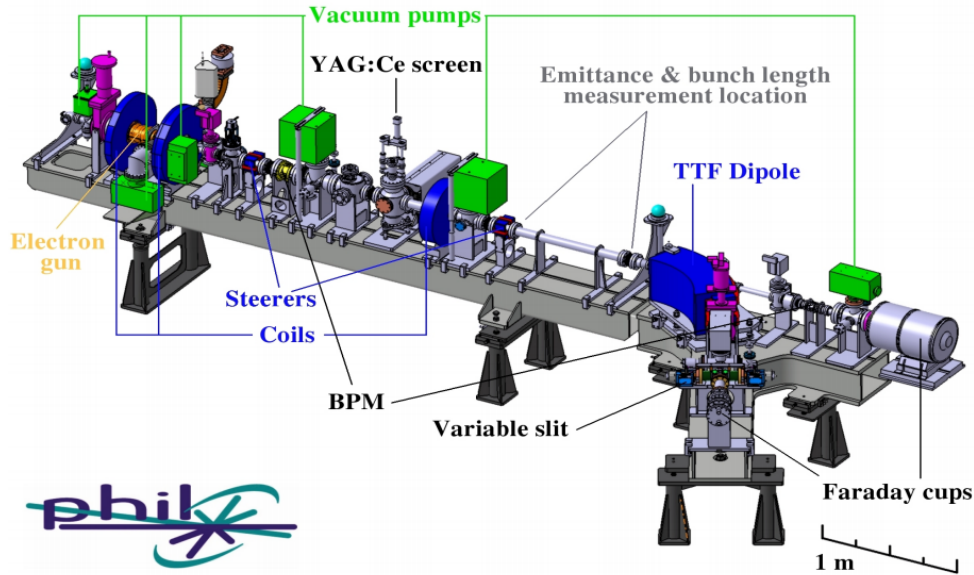


Figure 4.2: 3D view of the PHIL accelerator.

parameters, such as mean and dispersion energy measurement of the beam. The beam is deflected to the deviated line by the Tesla Test Facility dipole.

The direct beam line is equipped with two beam profile monitors (BPM), four phosphorescent transverse beam profile monitors, and a Faraday Cup. The beam profile monitor is the phosphorescent screen oriented at 45 degrees with respect to the beam axis. The screen is a cerium doped yttrium:aluminum:garnet (YAG:Ce) crystal scintillator of $300 \mu\text{m}$ thickness and 40 mm of diameter. Each phosphorescent screen is complemented with a versatile optical system made of one or more achromatic lens and a Gigahernet CCD camera (2 with $1/3''$ sensor format with $7.4 \mu\text{m}$ pixel size and 2 with $1/2''$ sensor format with $4.65 \mu\text{m}$ pixel size). The CCD dynamic range is 8 bit. In order to avoid pixel saturation during the measurement a remote control optical density wheel is mounted in front of each camera.

4.2.1 Working principle

In this section the main components of the PHIL facility are described in more detail. It belongs to the photoinjector type of linear accelerators which characterized by as short bunch duration as few ps when the radiofrequency gun is used. [80].

Electron gun

An electron gun is a source of electrons, which consists of the three major parts: electron emitter (cathode), accelerating region and focusing system.

The electron emission is performed either by heating the cathode (thermionic guns), photoeffect generation (photocathode guns) or quantum tunneling (field-emission guns). The acceleration of the released electrons is performed using the static (DC guns) or oscillating (RF guns) electric field. The focusing system is required at the stage after primary acceleration in order to prevent beam losses due to the beam divergence caused by Coulomb space charge interactions.

PHIL uses radiofrequency (RF) photocathode guns as an electron source. This type of guns generates electron beams accelerated to an energy of a few MeV on 10-20 cm distances and is used in several facilities [81–83]. The gun comprises photocathode and RF cavities, placed after the photocathode to accelerate released electrons.

The operation principle of the photocathode is illustrated by Figure 4.3, which represents the electron kinetic energy distribution in the cathode material. The blue and orange curves correspond to 0 K and 2000 K temperature respectively. At zero temperature no electrons are present above the Fermi level ϵ_f , while to be emitted from the cathode the kinetic energy at least of $\epsilon_f + W_{eff}$ is required, where W_{eff} is the effective work function in the conditions of the experiment. Generally, it is a function of the temperature and the electric field applied to the surface.

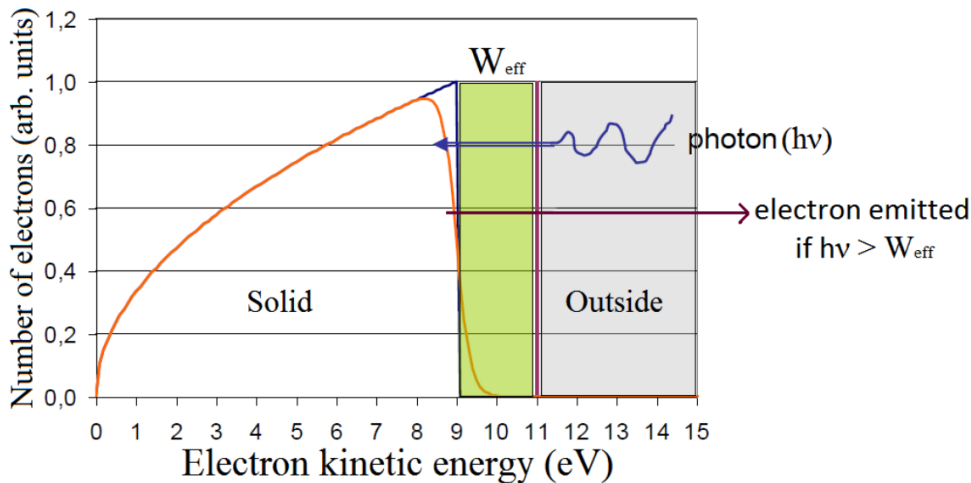


Figure 4.3: *The photocathode electron emission principle [80].*

Following the laser pulse irradiation with the energy of photons higher than W_{eff} the

electrons of the cathode acquire sufficient energy to leave the material.

The main advantages of photocathode RF guns are the following [84]:

1. The electron bunch length is determined by the laser pulse width, which may be as narrow as a few picoseconds. Thus ultimately short bunches can be obtained.
2. No buncher section is required, which permits extremely narrow energy spreads for the accelerated beam.
3. The electron bunch is synchronized with the laser pulse to picosecond accuracy.
4. Very low emittance beams can be produced simply by decreasing the laser spot size at the photocathode.
5. The RF cavity can support acceleration gradients of the order of 1 MeV/cm at the cathode, minimizing the space-charge growth of the emittance when the electrons are nonrelativistic.

4.2.2 Bunch timing

A detailed study of the bunch length at PHIL was performed by Thomas Vinatier and described in his PhD thesis [80]. The applied method and main results are summarized in this section.

Due to the characteristics of the RF gun described above, the measurement of time length of the PHIL bunches requires a sub-picosecond precision, which cannot be achieved using classical electronic devices like pick-ups or wall current monitors [85]. An overview of indirect methods, which measure the beam profile in a frequency domain by studying the electron beam radiation can be found in Ref. [86].

A so-called 3-phase method permits to measure the bunch length from 3 or more energy spread measurements at different acceleration conditions (amplitude of accelerating field or its phase). In practice it is easier to vary the RF phase, which gives the name to the method. A detailed description can be found in Ref. [80, 87, 88]. The results of bunch length measurements at PHIL are shown in Figure 4.4.

The measured bunch length is below 5 ps which places the PHIL facility among unique sources for various detector timing studies.

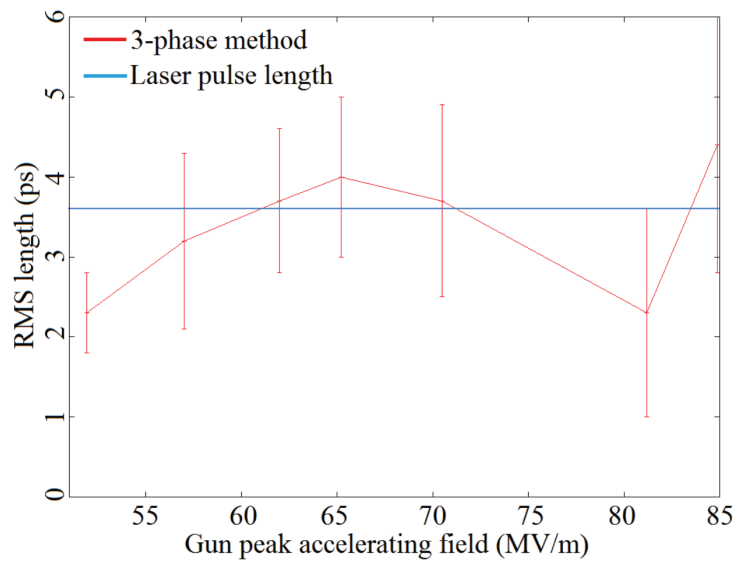


Figure 4.4: Bunch length RMS deduced from 3-phase method at PHIL as a function of the gun peak accelerating field [89].

4.3 Motivation

The test beam facilities play a crucial role in the detector R&D. As discussed in Section 4.2, the PHIL accelerator provides electron bunches of nominal energy and excellent time characteristics, which can be used for detector studies. Using these bunches a versatile platform for flexible testing and calibration of MPGD, and, more generally, to a much wider range of detector technologies, has been proposed. It aimed at providing the bunches of electrons with smoothly adjustable energy and intensity. A desired sample multiplicity starts from extremely low values for scintillating detectors for neutrino experiments or from single electron response for studies with MPGD. The upper multiplicity limit is the maximum possible values defined by PHIL bunch charge and applicable for silicon or diamond detector studies. In addition, variation of sample multiplicities in a wide range is required by linearity studies for numerous detector technologies. Finally, the operation cost of the facility should be minimized to ensure beam availability for routine detector studies.

According to its functionality, the new electron source was named LEETECH, which stands for Low Energy Electron TECHnique.

4.4 LEETECH Development

The principle of the LEETECH setup is illustrated in Figure 4.5. The beam coming from the PHIL beam pipe (2) scatters on the Aluminum attenuator (1), producing thus a wide energy spectrum and a solid angle distribution. The entrance collimator system (3) selects a direction of electrons entering the spectrometer and also adjusts the sample intensity. Thus obtained narrow secondary beam passes the magnetic field region (4) inside the vacuum chamber. At the exit (5) the electrons are again filtered by the exit collimator system and through the thin exit window collide with the test detector (6). The second exit window (7) with collimator system is dedicated to the educational and monitoring purposes. An additional lead shielding was added inside the vacuum chamber to reduce the background from electrons scattered inside the vacuum chamber. Since the signal electrons travel along a semi-circle in the magnet, an obvious relation between their momentum and the value of the magnetic field allows to select a desired electron energy by changing the field value. The electron energy in the delivered sample is controlled by dipole magnetic field which can be smoothly adjusted setting the dipole current value. Output intensity can be complementarily adjusted by changing the attenuator thickness and magnetic field.

Control and monitoring of the collimator systems and dipole current is performed remotely with a dedicated software from the PHIL control room.

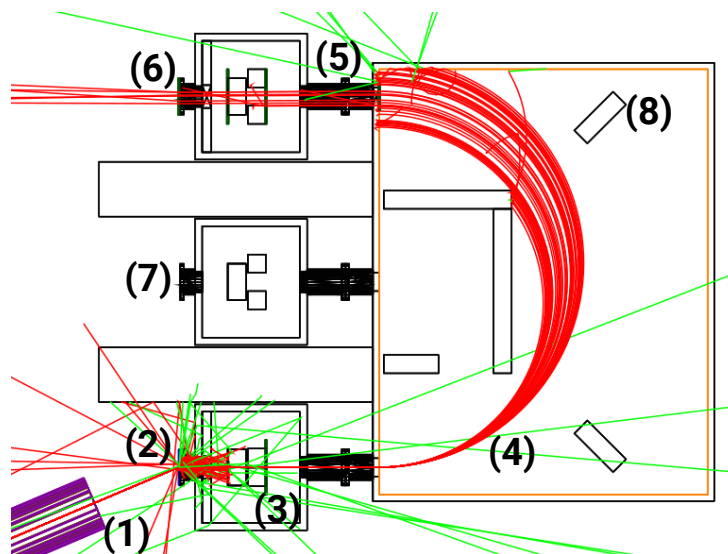


Figure 4.5: Schematic view of the LEETECH facility.

4.4.1 Magnetic field estimation

The size of the spectrometer is a compromise between the required magnetic field uniformity, magnet construction and magnet operation costs. The dimensions of the vacuum chamber were chosen such that the chamber fits in the gap of the dipole magnet. Assuming the diameter of the electron trajectories to equal to 40.3 cm, which is the size of the chamber, it is easy to calculate that 1750 Gs magnetic field is required to turn the 10 MeV electrons by 180°. In practice, the achievable energy range is defined by the linearity range of the magnetic field.

For the relativistic particle this relation can be written in terms of momentum and kinetic energy:

$$B(p) = \frac{p}{eR} \quad (4.1)$$

$$B(E_{kin}) = \frac{\sqrt{(E_{kin} + mc^2)^2 - m^2c^4}}{eR} \quad (4.2)$$

The maximum energy of electrons at PHIL is about 5 MeV with a 10 MeV future planned upgrade [79]. The plots corresponding to the relations 4.1 and 4.2 are shown in the Figure 4.6. In practice, they are used to quickly convert the magnetic field setting to the beam energy.

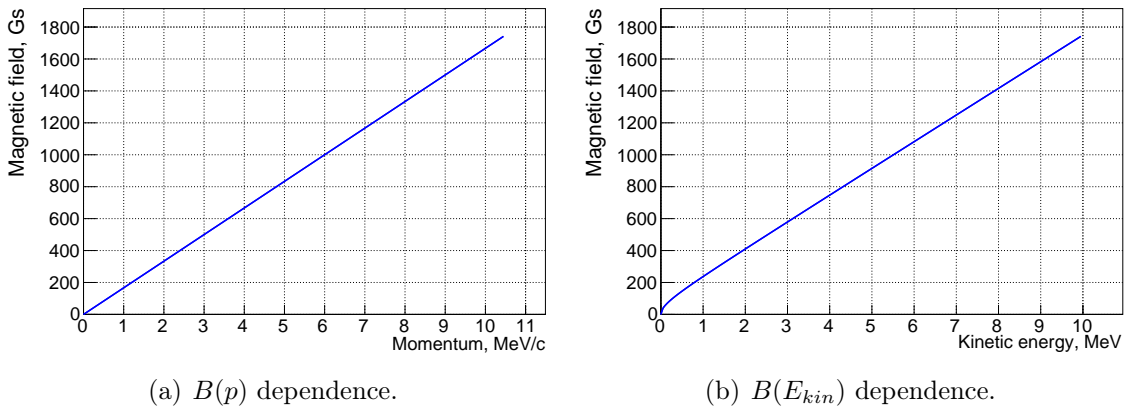


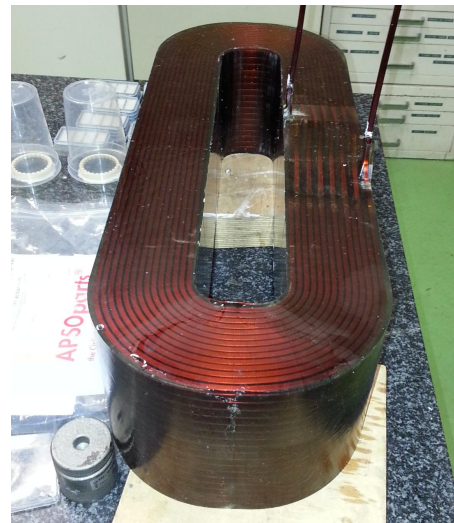
Figure 4.6: Magnetic field dependence on the desired electron kinetic energy and momentum.

4.4.2 Dipole magnet

The dipole magnet for the LEETECH spectrometer was designed and manufactured at CERN in beginning of 2014. The resistance of the magnet is 242 mOhm, inductance 360 mH, maximum current 42 A. The magnetic field range is from 0 to 2000 Gauss.



(a) Coil winding.



(b) Coil covered by a dielectric isolation.



(c) Upper yoke.



(d) Dipole assembled.

Figure 4.7: Production stages of the LEETECH dipole magnet.

The chosen power supply is to SM 18-50 (Delta Electronika) [90] with a voltage and current limitations of 18 V and 50 A, respectively. It has an Ethernet interface with an open application programming interface (API) for the remote control. The performance

of the power supply is critical for LEETECH, in particular its long-term stability of $9 \cdot 10^{-5}$ define the quality of the delivered electron samples.

The magnetic field dependence on XZ coordinates is shown in Figure 4.8(a). One can see the plateau region inside the magnet and a decreasing regions which correspond to a stray field that will turn the electrons and potentially distort the spectrometer operation.

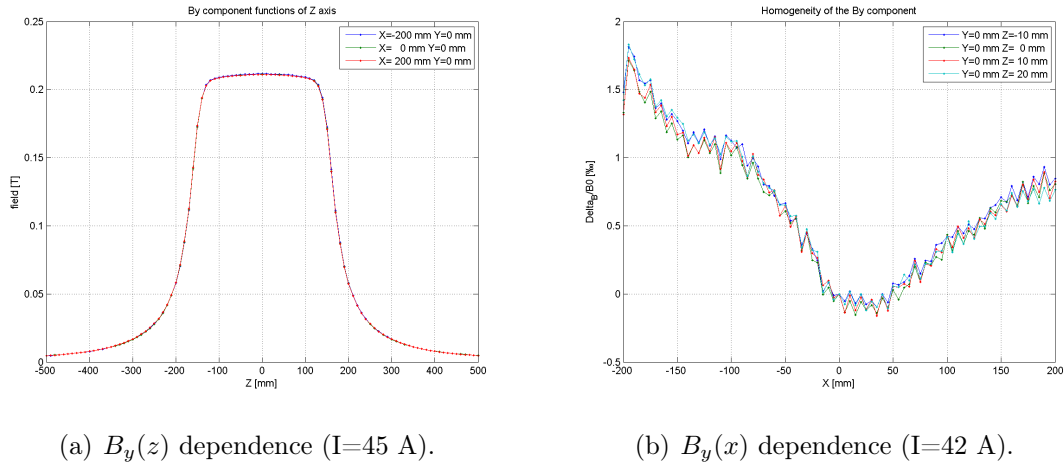


Figure 4.8: Dipole magnetic field, B_y component as a function of x and z coordinates.

To reduce the stray field outside the dipole, the ferromagnetic protection screen was designed and installed in front of the dipole, from the side of beam entrance, exit and detector area (Figure 4.9). The measurements of the magnetic field outside the dipole magnet were performed with and without the protection screen at CERN and at LAL. The results are shown in Figure 4.10. A clear effect of the protection reducing the stray field is demonstrated, while a good agreement is observed between the measurements and the corresponding simulation in Opera 3D software [91].

Different production stages of the LEETECH dipole magnet are shown in Figure 4.7.

4.4.3 Vacuum chamber

The vacuum chamber, in which the electrons travel in the magnetic field was designed and manufactured in TSNUK. The material chosen to be duralumin in order to minimize the magnetic field distortion inside the chamber. The 3D design and photo of the produced chamber is shown in Figure 4.11. The distance between beam the entrance and the beam exit is equal to 40.6 cm, which defines the electron trajectory diameter. The chamber has one beam entrance and two exit holes at one side and the hole for the vacuum pump at



Figure 4.9: The dipole magnet with the protection screen against stray field.

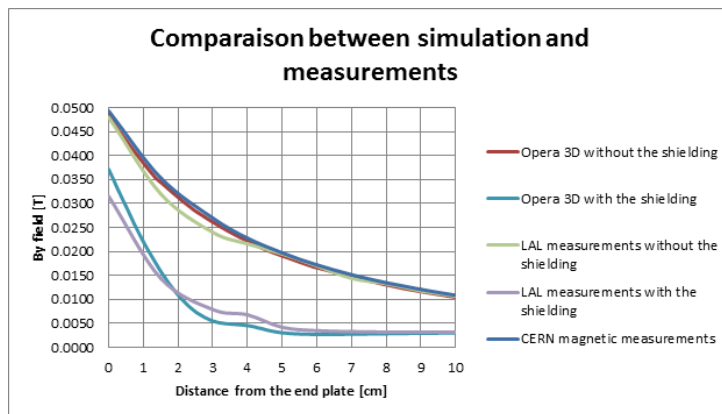


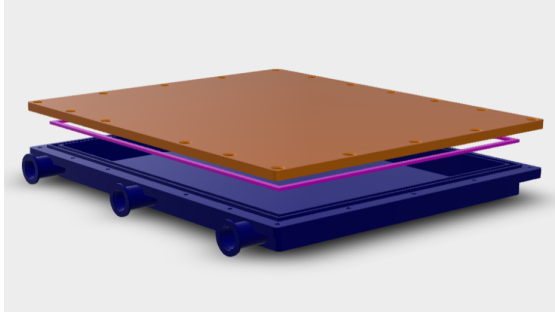
Figure 4.10: Stray magnetic field as a function of a distance from the protection screen. Simulation results and measurements are compared with and without the protection screen.

the opposite side. The collimator boxes and the pump are attached to the chamber with the vacuum clamps.

4.4.4 Collimator boxes

Three collimator boxes were produced to host the collimator systems at the entrance and the two exits of LEETECH. The transverse dimensions are limited by the distance between the holes (20.3 cm) so the side of each box is equal to 16 cm.

The 3D model of the vacuum chamber with 3 collimator boxes and manufactured



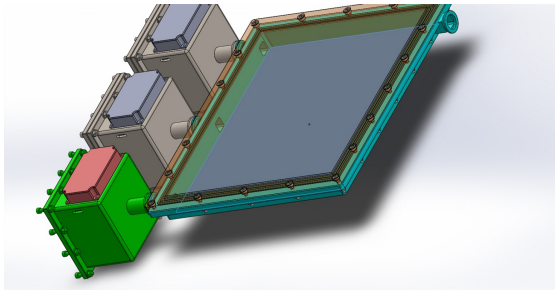
(a) 3D model of the vacuum chamber



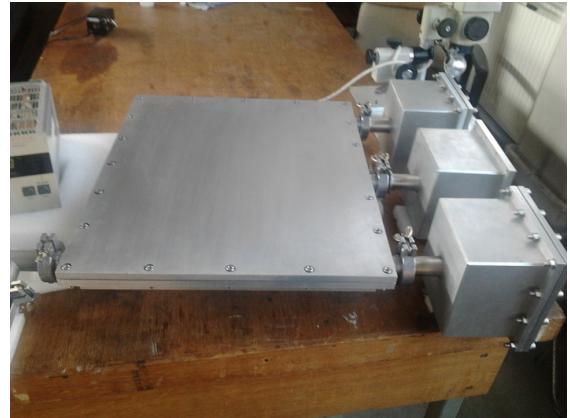
(b) Manufactured vacuum chamber

Figure 4.11: *LEETECH vacuum chamber.*

assembly are shown in Figure 4.12.



(a) 3D model of the collimator boxes



(b) Manufactured vacuum chamber with integrated collimator systems.

Figure 4.12: *LEETECH collimator system.*

4.4.5 Collimator systems

The collimator systems at the entrance and the exits aim at limiting the beam size, thus adjusting the intensity and energy spread. The collimators thickness should be sufficient to entirely stop electromagnetic showers from electrons of maximum possible energy with a punch-through negligible compared to the expected signal. The collimator jaws are made of duralumin, with the thickness of 20 mm, which provides lower than 10^{-3} reduction

factor for 3 MeV electrons. A possibility to adjust the collimator openings is provided by 4 separate jaws that can be moved independently with the the dedicated piezomotors (Figure 4.13).

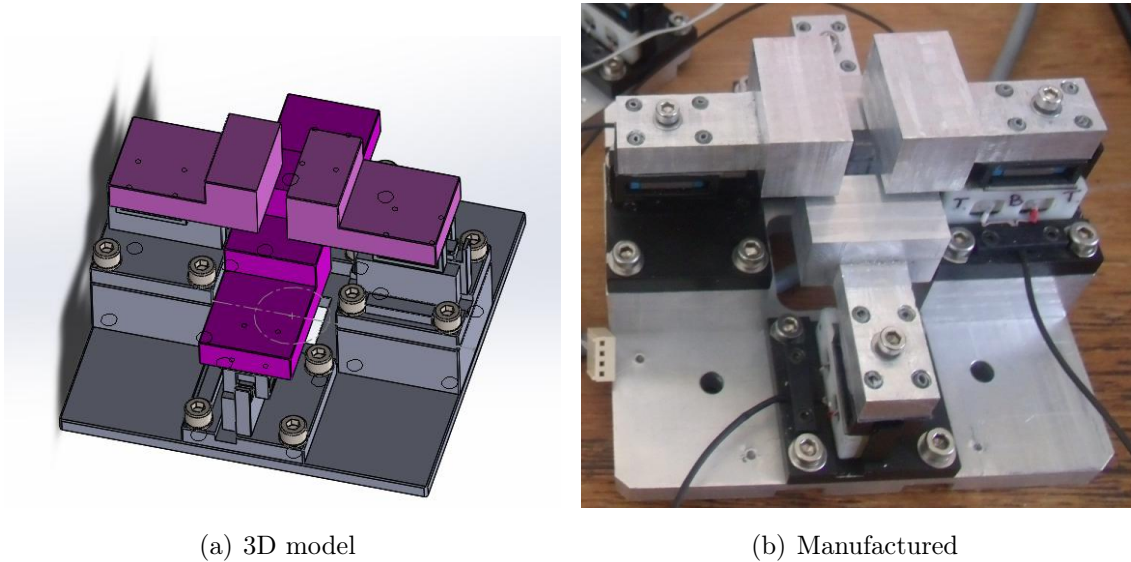


Figure 4.13: *LEETECH collimator system.*

The required positioning precision is 10-50 μm for each jaw for the fine beam tuning. Maximum opening between opposite collimators is 20 mm. The distance between the two edge positions of each collimator jaw is more than a half of maximum opening and is equal to 15 mm, which provides a possibility to adjust the center of the collimators opening window in a $15 \times 15^2 \text{ mm}$ square.

Piezomotors

The piezoelectric motor is based on the change of the material mechanical shape under the external electric field. The working principle is shown in the Figure 4.14.

At LEETECH the piezomotors of ultrasonic (resonant) type are used [92]. The motor consists of static (preload, actuator, guiding and sensor) and moving part (runner and scale). The mechanical contact between actuator and runner is provided with so-called coupling element, which performs a small moves due to piezoelectric deformation in alternating electric field. This moves the runner with attached scale, which position can be established with an external position sensor, placed close to the scale.

The ultrasonic piezoelectric motor is driven by the PWM pulses, which create a voltage

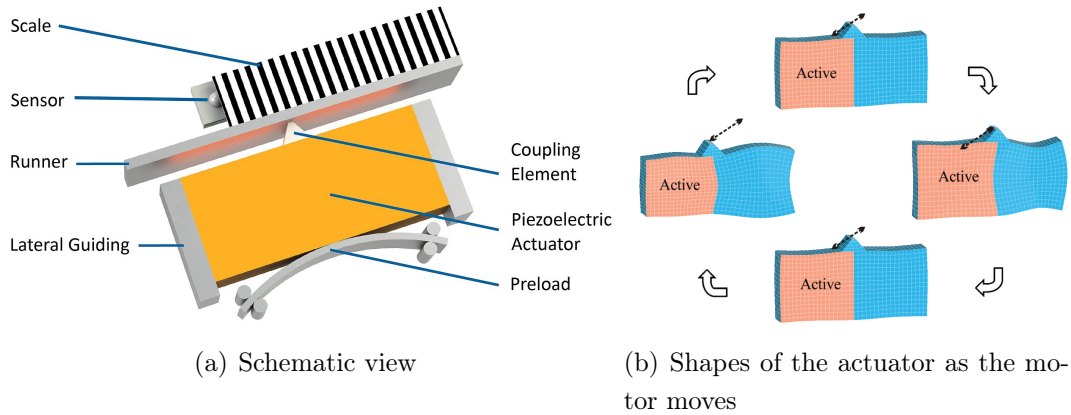


Figure 4.14: *The working principle of linear ultrasonic resonant piezoelectric motor.*

difference and thus an electric field in the actuator material, enabling the motion. The period of the PWM pulses should match the actuator resonance frequency.

The resonance frequency of the PWM pulses for LEETECH piezomotors is around 160 kHz and can vary from motor to motor within 10%. Amplitude of the pulses is 50 V. The duty cycle of the pulses defines the speed of the collimator jaw. The measured force varies from motor to motor and lies in the range of 1.2-1.6 N.

Position sensor

A variety of different types of sensors are present in the market [93]. In LEETECH, where the positioning precision of several μm is required, and the low cost of the facility components should be maintained, the magnetic linear sensor was chosen. The scale represents a magnetic strip with interchanging poles of fixed width, typically of order of 1 mm.

For LEETECH collimator systems the NSE-5310 Hall-effect position sensor was used [94]. For proper operation it requires a magnetic strip of 1 mm pole width placed 0.5 mm above the sensor surface. This provides a magnetic field of 10-40 mT inside the sensor, which is required for the Hall sensor cells. To eliminate constant magnetic field offsets the Hall sensors are grouped in four arrays (quadrants) and a signal difference of the opposite quadrants is taken for further amplification and digitizing. In order to reduce the effect of the field variations depending on the distance between scale and sensor surface (which can vary as the scale moves), the automatic gain control is implemented in the sensor chip using an amplifier with the gain adjusted depending on the Hall sensor signal amplitude.

The position information is stored in a 12-bit register (values from 0 to 4095), which is

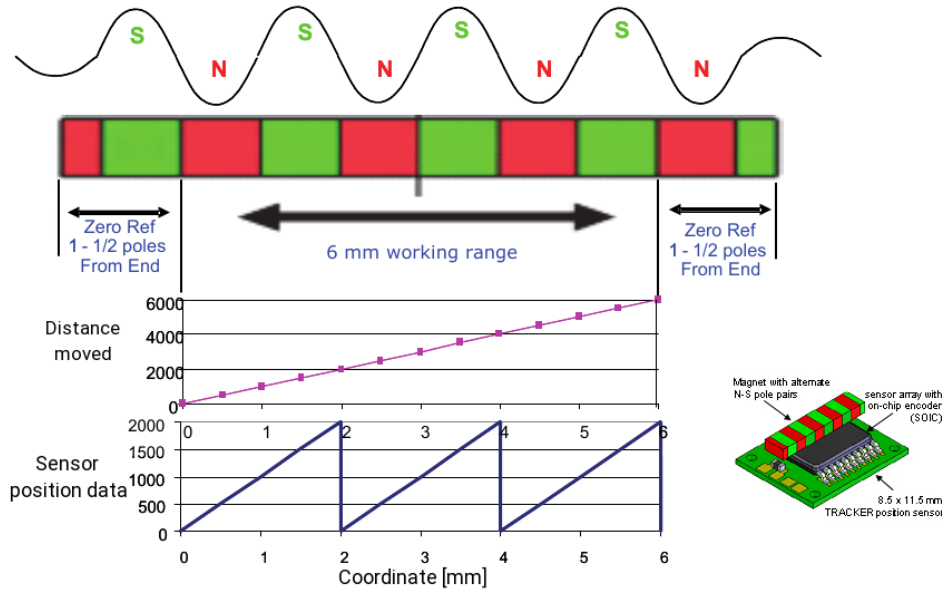


Figure 4.15: Working principle of the NSE-5310 linear Hall sensor used at LEETECH for collimator positioning.

incremented (decremented), when the scale moves related to the sensor on $0.488 \mu\text{m}$. Each 2 mm the register overflows (Figure 4.15), which requires an external overflow counting by the driving electronics.

The data from NSE-5310 sensor can be read using I²C interface, a detailed description of the message structure can be found in the datasheet [94]. Besides the position, the sensor message contains the data on temperature, magnetic field magnitude and automatic gain control. Four flags are also available to indicate whether the data is correct. One of them corresponds to the sensor-scale distance offset compensation and the three others to internal process of data conversion.

The timing is constrained by I²C bus specification V.2.1 [95], the NSE-5310 sensor supports the 800 kHz clock data transfer rate. For I²C message with 5-byte data payload this corresponds to a message transfer rate of 14 kHz, which defines the position readout period of $70 \mu\text{s}$.

4.5 Driving electronics

For remote control of LEETECH collimator system the following electronics was developed and manufactured in TSNUK: the master board provides the connection with PC via

Ethernet TCP/IP interface and communicates with three slave boards, each controlling a dedicated collimator system. A detailed description of master and slave boards are given in the following sections.

4.5.1 Master board

The Master board implements a communicator with PC and slave boards [96]. It is based on the ARM Cortex-M3 STM32F107VCT6 microcontroller unit (MCU) with 72 MHz core clock frequency, USB, Ethernet, SPI, USART and CAN controllers periphery [97].

PC communication

A common way at PHIL to provide a remote device control is to use the Ethernet connection. Its strong advantage is a possibility to use a long cables and route them into the beam area, so the lwIP (lightweight) TCP/IP stack was ported to the master board [98, 99]. The network settings and MAC address of the master board can be reviewed and changed in the netconf.c file [100, 101].

After parsing the corresponding message is compressed to a CAN bus message (8 bytes) and sent to the slave board. The message structure is described in section 4.5.2.

The photo of the master-slave-collimator system prototype, used for system validation, is shown in Figure 4.16.

4.5.2 Slave board

To provide the collimator position control the dedicated boards were developed at TSNUK. The implemented functionality comprises: PWM pulses generation with a possibility of fine period tuning, PWM pulses amplification (amplitude of 50 V is required), I²C communication with 4 position sensors, user interface for PC communication and debugging (USART), interface CAN bus, robust in noisy environment for reliable external automatic control.

The ultrasonic piezoelectric motors used in LEETECH are highly sensitive to the frequency of the driving PWM pulses. A 3% deviation from the resonant frequency may block the motor, though the frequency value differs from motor to motor by 7%. In addition, resonant frequency is impacted by temperature and humidity variations. Therefore, the PWM frequency tuning is essential for proper collimator system functioning.

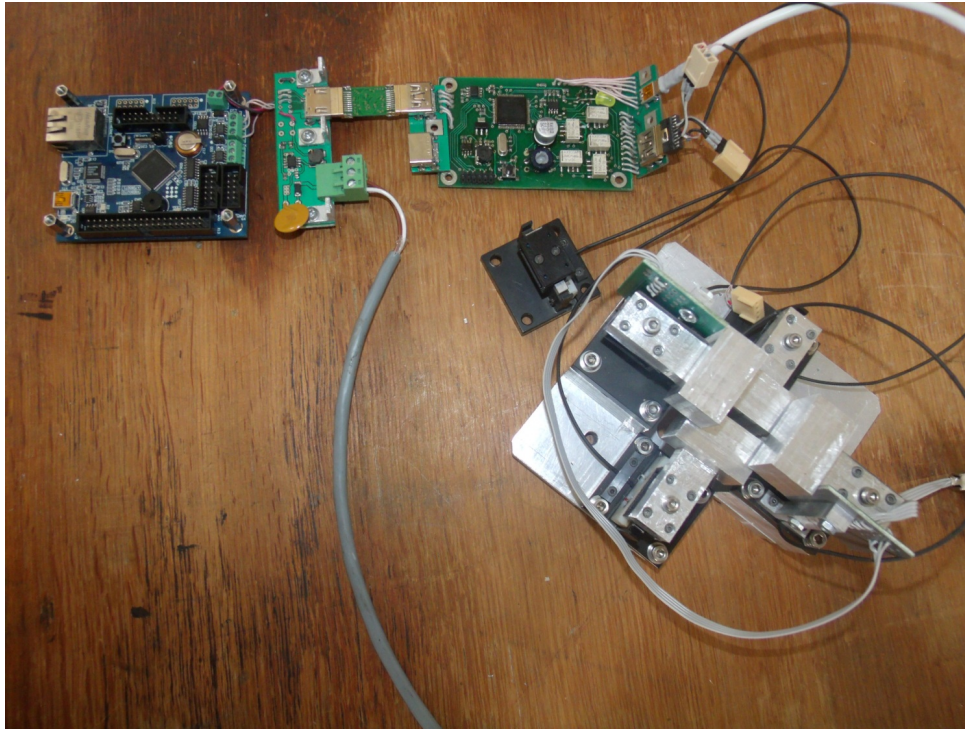


Figure 4.16: *Test setup of master board, slave board, test piezoelectric motor and collimator system.*

To implement the described functionality the base of the collimator driver was chosen to be an MCU with sufficiently fast PWM output pins and previously described peripheral interfaces (USART, CAN, I²C) - STM23F407VET6 chip with ARM Cortex M4 architecture [102]. The routed and manufactured printed circuit board (PCB) according to the corresponding schematic is shown in Figure 4.17.

The PWM pulses are generated using the MCU timers, the pulse period and step duration can be adjusted with a 25 ns precision, which is about 0.4% of the period corresponding to the mean resonant frequency of the motors. One board controls four motors of a single collimator system, so the generated pulses are redirected to a predefined motor using the relay system. The relay switching is performed using the general-purpose input-output (GPIO) pins of the MCU and transistor keys. Pulses amplification is performed using the transformer placed before the relay system in order to use one transformer per board rather than four.

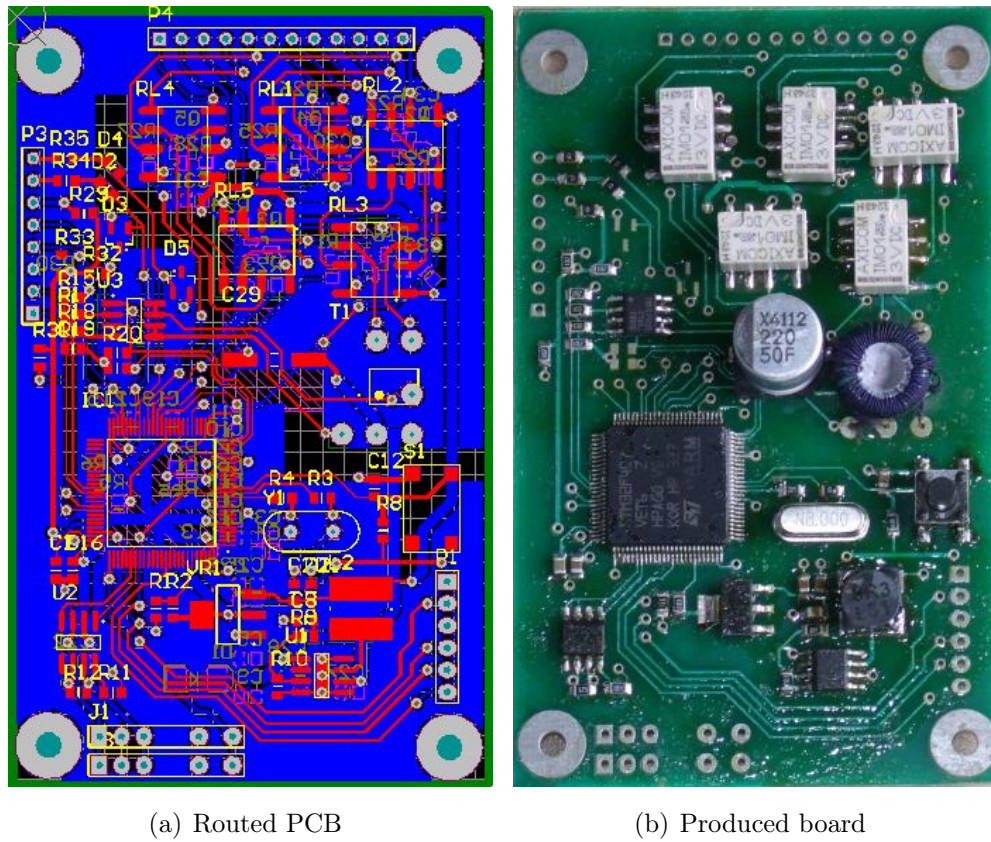


Figure 4.17: *Control board of a collimator system.*

CAN bus interface

The CAN bus interface was chosen to provide the communication between master and slave boards. It is stable against external electromagnetic noise and widely used in a vehicle production.

The CAN message frame structure and physical layer bit representation are shown in Figure 4.18.

The data is transmitted via 2 wires, which form a differential pair to cancel possible signal distortion due to external noise. The clock frequency is synchronized in each device in a line and not transmitted between devices like in I^2C interface.

The CAN frame contains a start-of-frame indicator, device identifier, remote transmission request bit, identifier extension bit, number of data bytes (up to 8), data payload, data correctness indicator (CRC field) and end-of-frame messages. With the maximal data length the whole frame consists of 108 bits, 64 of which are used to transmit the

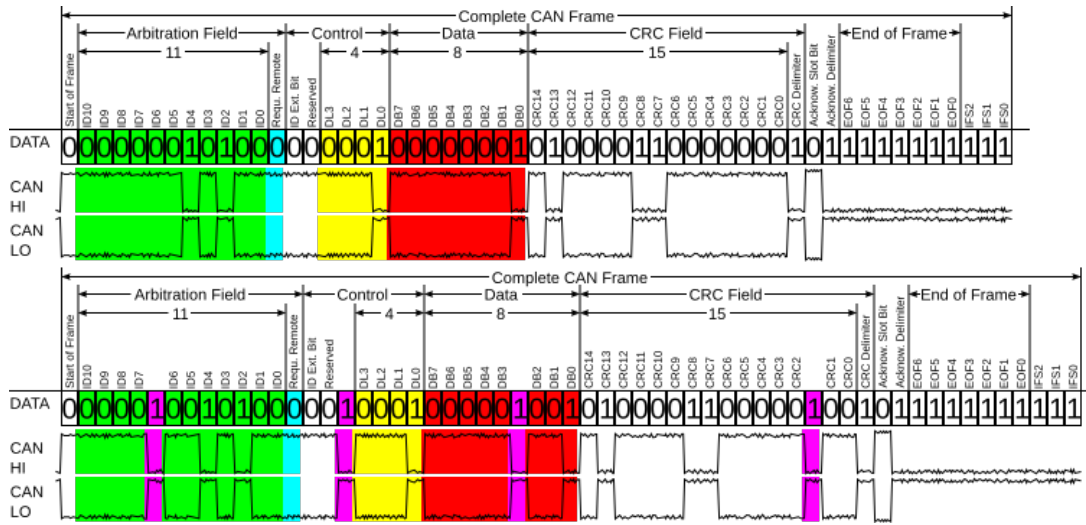


Figure 4.18: CAN bus message frame.

user data. To improve the data transfer stability and avoid desynchronization between the timing of incoming message and the receiver internal clock, a so-called bit stuffing was applied (Figure 4.18). After 5 consecutive logical 0's the logical 1 is inserted to make a synchronization edge (magenta bits). This helps to correctly adjust a clock phase in the receiver if a correction is needed.

A device connected to the CAN bus has an identifier which is transmitted in a frame just after the start-of-frame indicator. The identifier length can be 11 bits (standard identifier) or 29 bits (extended identifier), which defines a maximum number of devices in a line (2^{11} and 2^{29} , respectively).

The CAN bus with the standard identifier with 8 bytes of data payload is used for the master-slave communication to increase the data rate. A maximum clock rate of CAN bus periphery supported by the slave board MCU is 1 MHz, which limits a data transmission rate from slave to master board to about 9k frames per second, the exact value slightly depends on a bit stuffing.

Connectors

The following connectors were used to provide the electronics communication: PC-master - Ethernet, master-slave and slave-piezoelectric motors - HDMI and slave-position sensors - Firewire (IEEE 1394).

Master-slave communication message

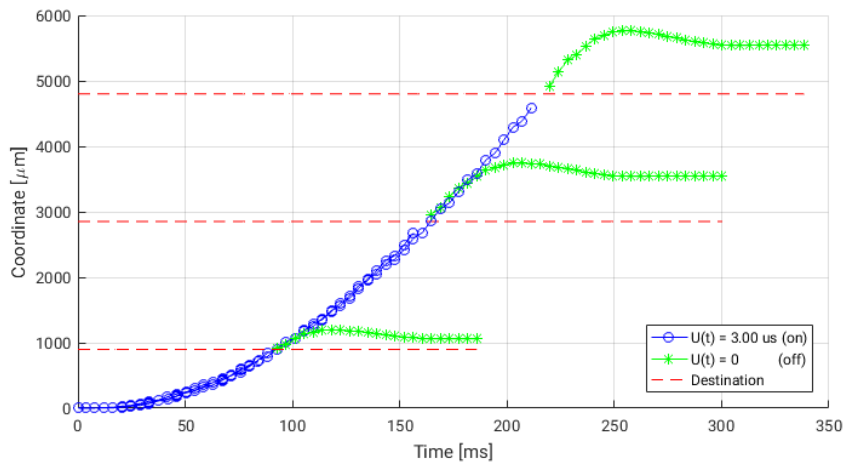
After the action has been performed at the slave side, it returns a response. In most cases it contains a collimator coordinate and the number of 2 mm gaps from the origin, since the gaps are not read by the position sensor (section 4.4.5), which fits the CAN message length. During tests and commissioning of the motors it is useful to explore the motor coordinate as a function of time (Figure 4.19). In this case a large amount of data is transmitted, which significantly slows down the slave-master communication speed (up to 10-15 seconds per trajectory) and therefore cannot be used during routine operation.

4.5.3 Controller design

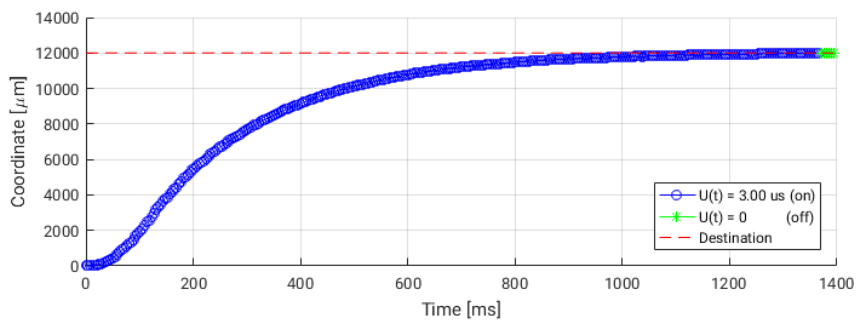
The required collimator positioning is about 10-50 μm . It was established that the naive control implementation when the driving pulses are switched off after the collimator reaches the destination (Figure 4.19(a)) brings a deviation of up to 1 mm. Trying to stop the driving pulses when some part of the destination path is covered slightly reduced the resulting deviation, but the order of 1 mm remained. The time of a single move increased to a few seconds though, so this way to enhance the positioning precision was abandoned.

Instead, the corresponding PID controller [103] was designed to handle the motion of all the motors, independently of their orientation. In the ultrasonic resonant piezomotors the way to adjust a speed is to vary the driving pulses duty cycle, keeping the period the same (according to the motor resonant frequency). In Figure 4.19(b) the trajectory of the motor moving to a large distance is shown along with the duty cycle variation while the motor moves.

The designed PID controller gradually decreases the motor speed as it approaches the destination. The resulting deviation in Figure 4.19(b) is 2 μm , which however not achieved for all cases due to inhomogeneous friction along the moving path. The overall deviation of a single motor positioning does not exceed 20 μm , which results in a 40 μm precision for setting the opening of the opposite collimator jaws.



(a) No controller



(b) PID controller

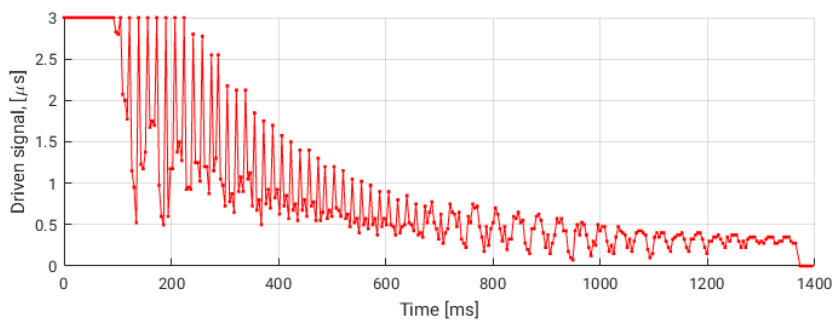


Figure 4.19: Control board of a collimator system. The motor driven signal represents the time range when the PWM signal state was high. The period of the PWM signal corresponds to the motor resonant frequency and equal to $3.5 \mu\text{s}$ with a small deviation of about $0.3 \mu\text{s}$ depending on the motor.

4.6 Simulation

The Geant4 simulation was maintained during the LEETECH project design, commissioning and test beam sessions planning. The geometry is shown in Figure 4.5.

4.6.1 Attenuator thickness optimization

At the very beginning of planning the test beam based on the PHIL accelerator the possibility to decrease the PHIL electrons energy was studied. The process of the beam scattering on the aluminum attenuators of different thickness was simulated and the spectra of scattered electrons was studied (Figure 4.20).

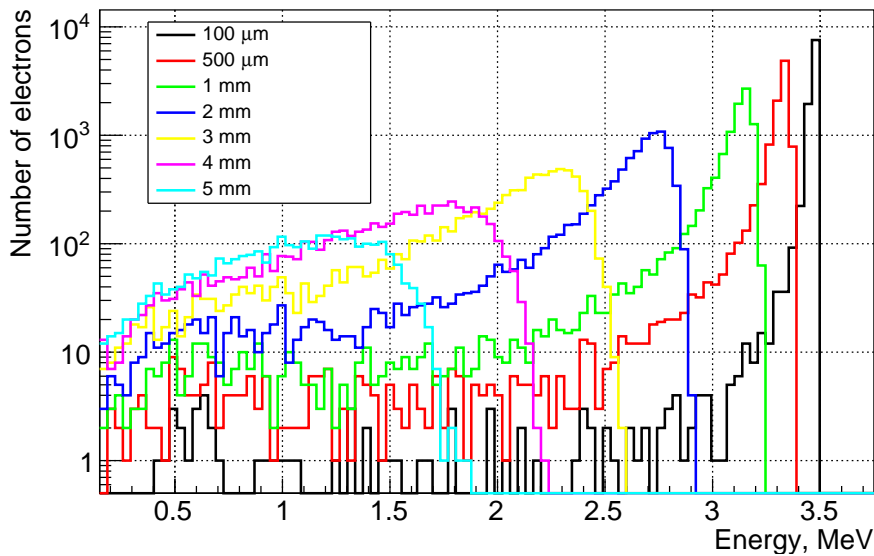


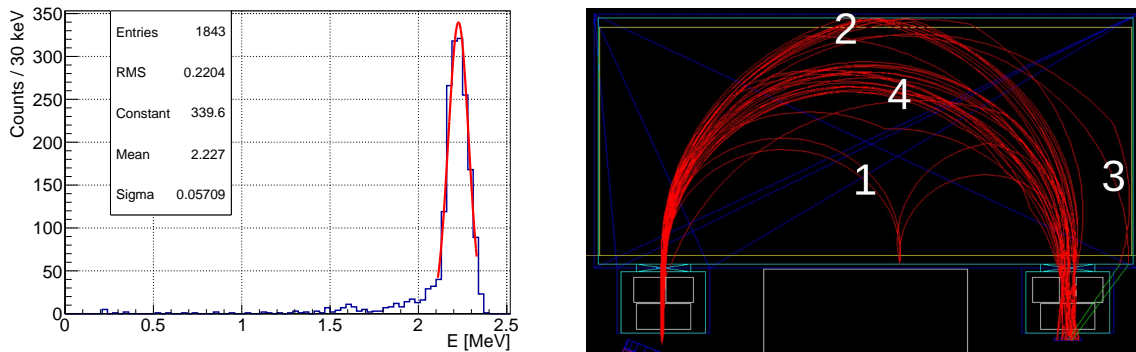
Figure 4.20: Kinetic energy spectra of 3.5 MeV electrons scattered on aluminum attenuator of different thickness obtained with Geant4 (10^4 events).

The obtained results indicate that it is possible by scattering to produce electrons of the whole energy range up to the energy of the primary (beam) electrons. Also Figure 4.20 demonstrates which attenuator should be used to achieve the highest bunch intensity in the specific energy range. Thus if the bunches of 2.5...3 MeV electrons are needed, the 2 mm attenuator should be used to maximize the LEETECH bunch intensity range.

According to this simulation attenuators of 0.1, 0.5, 2, 4 and 6 mm thickness were produced to extend the intensity range of the spectrometer at a given energy of the electrons at the exit.

4.6.2 Inner shielding

One of the key characteristics of the test beam facility is the energy spread of the provided beam. The corresponding simulation in was performed to study this parameter, the typical spectrum of the electrons from LEETECH is shown in Figure 4.21(a).



(a) Typical spectrum of electrons at the exit of LEETECH with 20x20 mm exit collimator opening. (b) Beam propagation in LEETECH vacuum chamber without the inner shielding. Trajectories of electrons that are reflected from the chamber walls (1 and 2), produce the gammas hitting the test detector (3) and correct ones (4) are shown.

Figure 4.21: *LEETECH spectrum and source of noise.*

The tail of energy distribution corresponds to the noisy particles and decreases the beam quality. In order to reduce this part of the spectrum the trajectories of corresponding electrons were investigated (Figure 4.21(b)). In order to suppress the noisy electron trajectories the inner shielding was added to the LEETECH vacuum chamber design (Figure 4.5).

4.6.3 Energy spread

The time and energy spread of the LEETECH electrons were also studied as a function of the collimators opening, which reduces the spatial beam divergence. The results of the energy spread study are shown in Figure 4.22.

The energy spread was studied for different entrance collimator openings. Figure 4.22(a) shows energy spread depending on the entrance collimator opening, while the exit collimator was 20x20 mm² open. While the energy spread increases with opening collimators and accepting more electron directions, starting from a 10x10 mm² opening, all the elec-

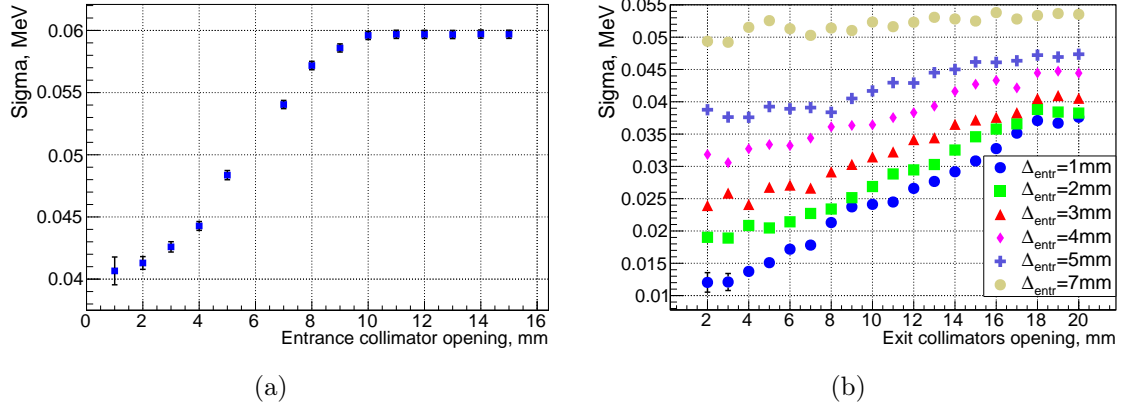


Figure 4.22: *LEETECH* energy spread as a function of collimator openings. The *PHIL* electron energy of 3.5 MeV, attenuator of 2 mm thickness and dipole magnetic field of 400 Gs (2.7 MeV mean electron energy at the exit) were set in the simulation.

trons, defined by the target characteristics and the exit collimator openings are accepted and the energy spread curve is saturated.

The energy spread can be improved by better defining the electron direction using entrance and exit collimators. This is illustrated by Figure 4.22(b) for the entrance collimator opening between 1 and 7 mm, exit collimator opening between 2 and 20 mm. For small collimator openings a very low energy spreads of 12 keV can be achieved for 2.7 MeV electrons at the exit of *LEETECH*. Starting from 7x7 mm² entrance collimator energy spread curve becomes saturated and the sample quality can not be further improved by the exit collimator system.

4.6.4 Beam propagation through the *LEETECH* spectrometer

For complete understanding how different parts of *LEETECH* impact the beam characteristics and which side effects do they bring as the particles propagate through the spectrometer the so-called ideal plane detectors were introduced to the simulation, which store the parameters of particles that cross the detector plane. From the programming point of view, the corresponding detector class does not include any of Geant4 routine, therefore does not affect the Geant4 particle tracking. Such planes were added: after the aluminum attenuator, before the entrance collimators, after the entrance collimators, to the exit of the vacuum chamber, before the exit collimators, after exit collimators and at the exit of *LEETECH*.

4.7 Spectrometer characterization

4.7.1 Scintillator plate

The first measurements at LEETECH were performed with the plastic scintillator coupled to the multi-channel plate photomultiplier (MCPMT) Hamamatsu SL-10. The data acquisition was performed using the LeCroy WavePro 740Zi-A oscilloscope with a 4 GHz bandwidth and 40 GS/s maximum sample rate. Several scans characterizing the LEETECH facility were performed, such as magnetic field scans for different attenuators and collimator opening scans. In each case the magnitude of the detector signal was studied.

The screenshot of an arbitrary picked event is shown in Figure 4.23. Two MCPMT channels are connected to the oscilloscope channels 2 and 3, indicating a clear signal, synchronous to the beam.

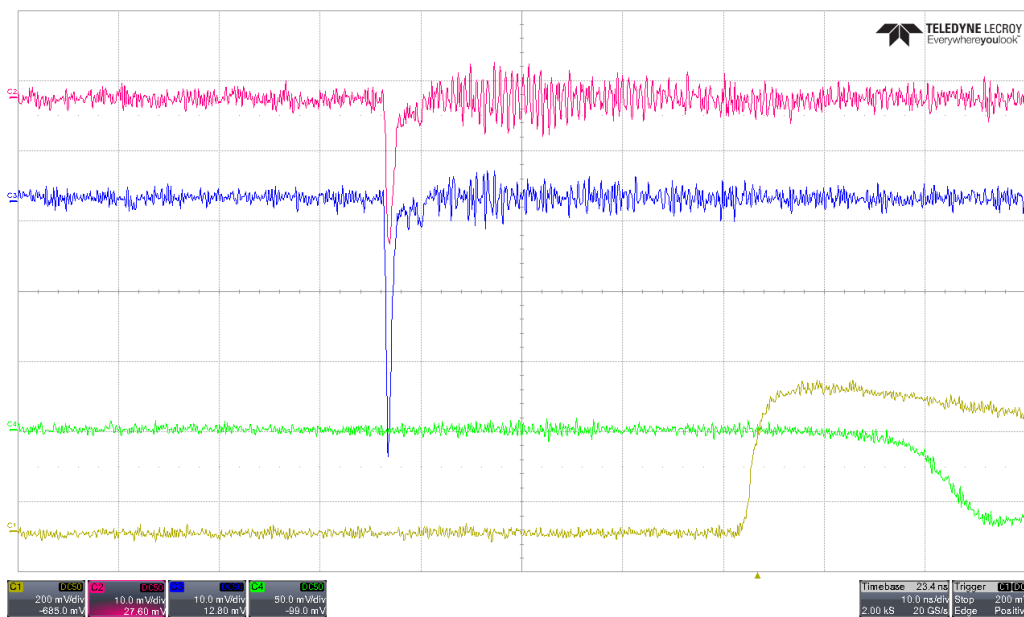


Figure 4.23: Typical event waveform from the plastic scintillator+MCPMT measurement session. The scintillator covers 2 channels of MCPMT which are attached to the channels 2 and 3 (red and blue). First channel (yellow) is a laser-initiated signal which serves as a trigger for data acquisition. The 4th channel (green) is coupled to the scintillator+PMT assembly placed on the floor beneath the LEETECH, to have an indicator of background in the room.

To obtain the spectral characteristics of produced attenuators the corresponding measurements were performed. With each attenuator the magnetic field was varied in range

when the signal is visible on the waveform and the data acquisition was performed. Results of the mean pulse magnitude as a function of the dipole current are shown in Figure 4.24.

The obtained curves represent the spectral characteristics of the LEETECH with different attenuators. This agrees with the simulation results presented in Figure 4.20, which characterize the attenuators itself.

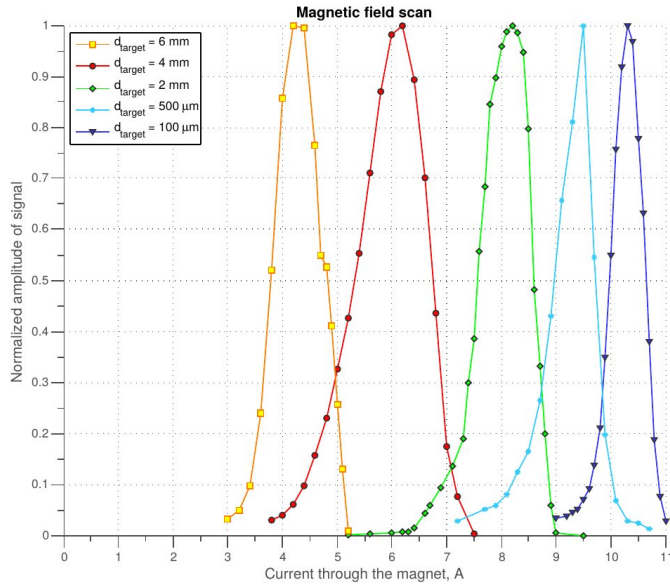
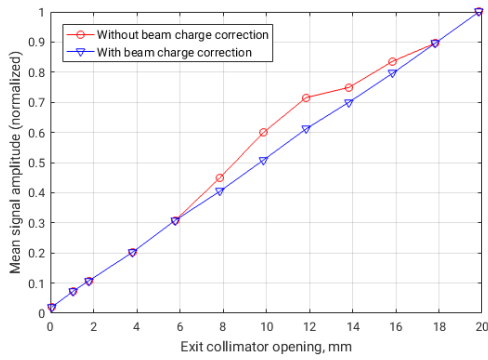


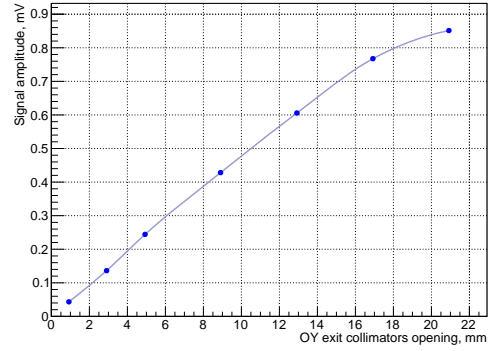
Figure 4.24

The results of exit collimators opening scans are presented in Figure 4.25. For the exit collimators opening scan along X axis 4.25(a) the normalization to the signal from the integrating current transformer (ICT) from PHIL was applied in order to explain the results deviation from the expected linear dependence. The signal amplitude behavior looks reasonable for both small and large openings at the entrance, demonstrating a saturation in the latter case.

The characterization session was the first long measurement session at LEETECH. Besides the quantitative results of the attenuators spectral characteristics and collimator scans, the first experience in driving the LEETECH facility was explored. At that time the operation was not very smooth and some instabilities in the remote control defined the further scope of work, described in Chapter 4. These improvements prepared the LEETECH to further successful measurement sessions described in the next chapters.



(a) Results of the exit collimators opening scan along X axis. The entrance collimators are 11.07x10.03 mm opened while the dY opening at the exit is 20.92 mm.



(b) Results of the exit collimators opening scan along Y axis. The entrance collimators are 2.07x19.84 mm opened while the dX opening at the exit is 9.89 mm.

Figure 4.25: Measurements of the LEETECH beam magnitude as a function of the exit collimators opening.

4.8 Studying low intensities with diamond sensor

LEETECH provides a compact low-energy electron source for characterisation and quality control of wide range of detector techniques, including semiconductor detectors, scintillating materials, and gaseous tracking detectors. One of the key goals of LEETECH is to ensure low-multiplicity operation mode with a capability to deliver calibrated samples of a few electrons with energy spread at the level of a few percent.

An important demonstration of providing few-electron samples, including samples with a single electron, is performed using a diamond sensor. Physics properties and the ability to detect single electrons with diamonds are discussed e.g. in Refs. [104–107]. Recently S. Liu and co-authors [108], using the in-vacuum diamond sensor successfully demonstrated a dynamic range of 10^6 by simultaneous beam core (10^9 electrons) and beam halo (10^3 electrons) measurements at ATF2.

In this section a capability of diamond sensor to distinguish between signals from individual electrons is investigated. Systematic studies of diamond sensor sensitivity to a few electrons require electron sources operating in low-multiplicity mode. The knowledge of diamond sensor operation in this regime is crucial, for several applications, and in particular for the experiments at high energies, where the detector is located near a beam pipe (beam loss monitors), where showers from high-energy particles are almost completely absorbed leading to only a few particles intercepted by the diamond sensor [109].

4.8.1 Diamond sensor

Low-multiplicity operation mode of LEETECH is studied below using diamond sensor. The diamond sensor used in the experiment (Figure 4.26) was prototyped and fabricated at LAL. A single crystal Chemical vapour Deposition (CVD) diamond from Element Six [110], with TiPtAu metallisation on the top and bottom surfaces, is glued with the conducting glue on the PCB. The top surface of the diamond is connected to the signal line on the PCB by four bonding wires. Such a design allows to reduce electron scattering before they reach the active area of the diamond. High voltage is applied through the conductive area on the PCB underneath the diamond.

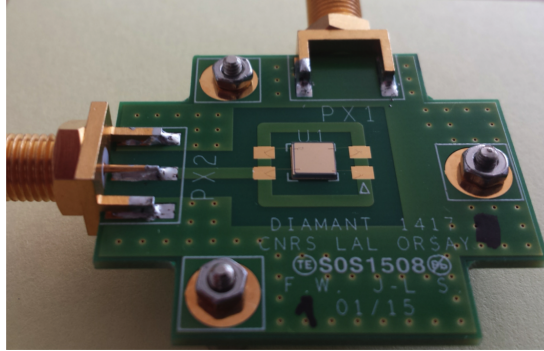


Figure 4.26: *Diamond sensor used for LEETECH characterization.*

4.8.2 Calibration of diamond sensor

Proper calibration of the diamond detector requires a MIP source. One of possible candidates for such calibration can be atmospheric muons. However, taking into account a small surface of diamond sensor the rate of such events will be low, on average ten events in one hour. Electrons with energies above 1.8 MeV can be also used for calibration. For calibration of the diamond sensor we used a $^{90}\text{Sr} + ^{90}\text{Y}$ radioactive source. To avoid the contribution of non-MIP electrons from the $^{90}\text{Sr} + ^{90}\text{Y}$ spectrum we triggered on a scintillator placed behind the diamond sensor. This allows filtering the low-energetic part of the $^{90}\text{Sr} + ^{90}\text{Y}$ spectrum and detecting only the electrons possessing sufficient energy to traverse the “sandwich” diamond - PCB. The signal from diamond sensor is amplified by charge sensitive amplifier (CIVIDEC C6) with gain factor of 4mV/fC and the noise RMS of 0.7 mV [111]. On average the ionisation of diamond yields 36 electron hole pairs in 1 micrometer. The Most Probable Value (MPV) of the collected charge for a single crystal CVD of 0.5 mm thickness is 2.88 fC, which corresponds to an energy of 225 keV deposited in the diamond.

The mean value and the standard deviation of the Landau distribution are not well determined due to the long tails towards high energies. Instead, we use the MPV and FWHM of the distribution was used. From Figure 4.27, the MPV of the signal amplitude and the FWHM are 12.0 ± 0.5 mV and 4.0 ± 0.5 mV, respectively. Note that the histogram in Figure 4.27 is a convolution of the Landau distribution and Gaussian function to account for the amplifier noise.

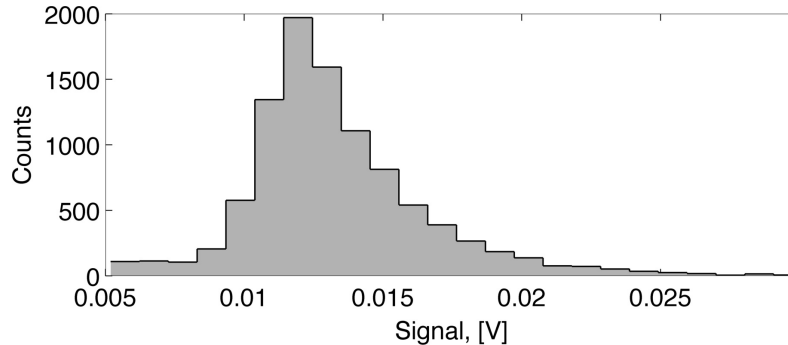


Figure 4.27: *Diamond sensor response to the single MIP electrons. The MPV of the energy deposition is 12 mV.*

4.8.3 Deposited energy spectrum simulation

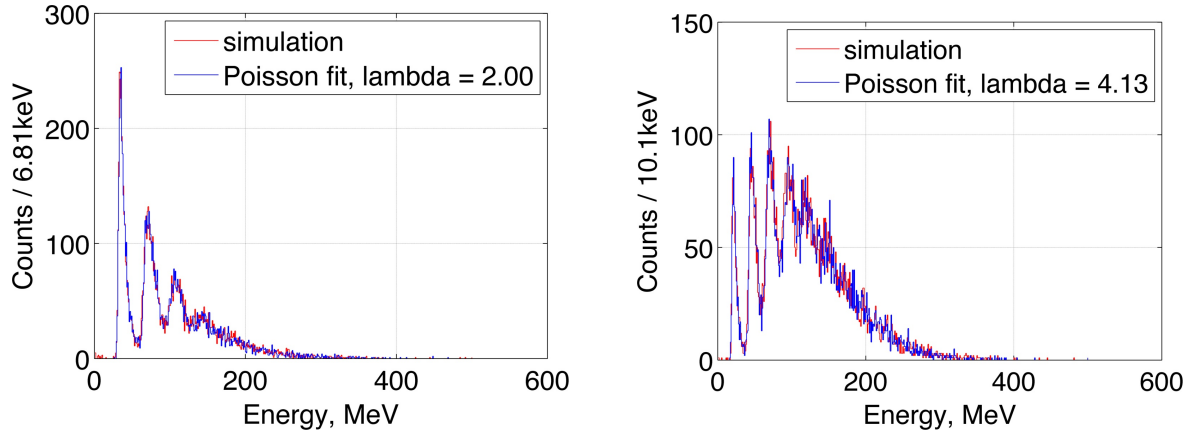
The full Geant4 simulation of one bunch of $10^8 - 10^9$ primary particles passing through LEETECH is computationally challenging. Simulation with a sample acquired in a typical experiment (thousands of bunches) is not realistic in terms of computational power. On average it takes 12 hours using one CPU, and approximately 1.5 hours in configuration with 8 threads. For the optimization studies the computing time increases proportionally to the number of simulation parameters and becomes resource consuming.

Therefore the simulation is divided in several steps - data from artificial detectors were recorded at each stage and used as a source for the following simulation stages.

Firstly, from the distribution after the entrance collimators a new particle source with generalised parameters representing the particles arising from bunches at that location was constructed. It includes normal distributions of energy, angle, and position of the electrons, which enables one to generate the identical particles at this position, rather than repeat the modelling from the PHIL beam pipe. With this new General Particle Source (GPS) we obtain the same results after the exit collimators as with the initial electron bunch. For different configurations of the entrance collimator this procedure has been repeated. In such a way the Geant4 tracking in section upstream the vacuum chamber (PHIL, attenuator, entrance collimator) and downstream the entrance collimator (vacuum chamber, magnetic field, exit collimator) can be treated separately, thereby significantly decreasing the modelling time.

To obtain the GPS data one bunch of $2 \cdot 10^8$ electrons was used with entrance collimator opening of 2.6×1.8 mm, giving 10^4 detector hits, which is sufficient to obtain the parameter distributions for the electrons generation. Using the constructed GPS the random samples each containing $N_{e^-} = 10^4$ electrons were generated. Then the electrons are propagated,

and the energy deposition in the diamond sensor is recorded.



(a) Energy deposition for exit collimators openings of 1x1 mm.

(b) Energy deposition for exit collimators openings of 1.4x1.4 mm.

Figure 4.28: Energy deposition in the diamond sensor by the LEETECH electrons. a, b) Energy deposition distribution for different exit collimator apertures. Entrance collimator opening 2.6x1.8 mm.

Figure 4.28 shows the energy deposition in the diamond sensor for the exit collimator openings of 1x1 mm and 1.4x1.4 mm respectively.

One can discriminate clear peaks in Figure 4.28(a) and Figure 4.28(b). These peaks represent contributions from one, two, three and four electrons, respectively, traversing the diamond simultaneously. For Figure 4.28(a), and 4.28(b) the numbers of empty samples are 15% and 1.4%, respectively. Thus, comparing Figure 4.28(a) and Figure 4.28(b) one can see the role of exit collimators.

Average number of electrons in the sample

In order to demonstrate that the distributions in Figure 4.28 are consistent with those expected from small number of electrons according to Poisson statistics, the energy depositions in the diamond sensor, $E_{dep}(N_{e^-})$, from a given number of electrons $N_{e^-} = 1, 2, \dots, 100$ was generated. The $E_{dep}(N_{e^-})$ is normalized to the total number of events $N_{samples} = 10000$, which is the same as in Figure 4.28. Therefore $E_{dep}(N_{e^-})$ can be used as a basis for describing the simulated LEETECH distributions (Figure 4.28). In order to find λ the minimisation of the following single parameter cost function is performed:

$$f(\lambda) = \ln \left(\sum_E \left[E_{dep}^{LEETECH}(E) - \sum_{N_{e^-}=1}^{100} P(\lambda, N_{e^-}) E_{dep}(N_{e^-}) \right]^2 \right), \quad (4.3)$$

where $E_{dep}^{LEETECH}(E)$ is the result of our Geant4 simulation of LEETECH (blue curves in Figure 4.28(a), 4.28(b)), $P(\lambda, N_{e^-})$ - Poisson weights and $E_{dep}(N_{e^-})$ is the energy deposition in the diamond sensor for $N_{e^-} = 1, 2, \dots, 100$ electrons.

Table 4.1: Estimation of the Poisson parameter λ .

λ	empty samples	mean	variance	fit
Figure 4.28(a)	2.08	2.02	2.31	2.00
Figure 4.28(b)	4.08	4.08	4.76	4.13

The results of the minimisation of $f(\lambda)$ are shown in Figure 4.28(a) and 4.28(b) in red. One can see a good agreement between the fit and the simulation data. In these numerical experiments LEETECH provided the Poisson distributions of electrons with rate parameter of 2.0 and 4.13 for Figure 4.28(a) and 4.28(b), respectively. The Poisson parameter estimated from empty samples as $\lambda = -\ln(N_0/N_{samples})$, from the mean value and from the variance is presented in Table 4.1. The value of Poisson parameter obtained from the variance is overestimated, due to the long tails in $E_{dep}(N_{e^-})$, which contribute to the neighbouring peaks. However since the resolution of 0-electrons peak (noise) and 1-electron peak is good, the estimation of λ from the number of empty samples gives a reasonable result, which we use as the starting point during the minimisation of Eq. 4.3.

Control of the rate parameter

In Figure 4.29 dependence of the Poisson parameter obtained by minimisation according to Eq. (4.3) as the function of the exit collimator opening is presented. For the openings smaller than the size of the detector the dependence can be expressed as a linear function:

$$\lambda(x) = \alpha \Delta x \Delta y = \alpha S, \quad (4.4)$$

where Δx and Δy are the exit collimator openings along the horizontal and vertical axes measured in mm. The linear fit in the mentioned range gives the value of non-dimensional parameter α of 2.3 ± 0.1 . This form of dependence confirms that the number of electrons passing through the exit increases linearly with the opening of the collimators.

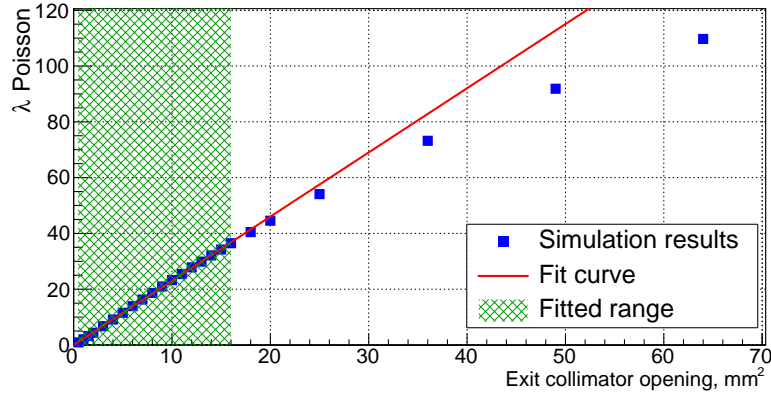


Figure 4.29: Poisson parameter λ as a function of the exit collimator opening.

Thus the quantity α describes the *efficiency* of the reduction of the initial sample population down to the delivered low multiplicity of the sample. For exit collimator opening of $S = 1 \text{ mm}^2$ Poisson parameter λ coincides with the efficiency parameter α . For fixed values of the magnetic field the parameter α is a function of the sample charge entered LEETECH, determined by PHIL bunch charge and entrance collimator openings. Decreasing the entrance collimator openings leads to smaller values of α , which allows to control the Poisson parameter in a more accurate manner.

Beam size effect

In the results presented in Figure 4.29 the PHIL electron beam was simulated as a unidirectional point source. Taking into account realistic beam size greatly reduces effective number of electrons entering the spectrometer.

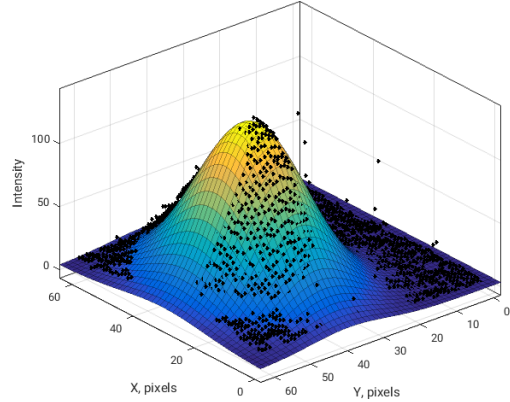
To estimate the beam size and displacement the photo of the lanex luminescent screen (Figure 4.30(a)) was analysed. The intensity of the beam spot follows the Gaussian distribution. The beam size and displacement from the attenuator center can be estimated with the fit of the image intensity, which results are presented in Figure 4.30(b). Knowing the size of the cross on the lanex, the beam sigma of $2.7 \pm 0.3 \text{ mm}$ and displacement of $2.0 \pm 0.2 \text{ mm}$ and $1.5 \pm 0.2 \text{ mm}$ along X and Y axes respectively were determined.

Introducing the estimated beam size of the delivered multiplicity is adjusted by a beam size correction factor of 0.094 ± 0.020 . This results in the corrected value of efficiency α of 0.21 ± 0.05 .

Assuming that beam position alignment with respect to attenuator is significantly



(a) Lanex luminescent screen placed on top of the LEETECH attenuator.



(b) 2D Gaussian fit of the beamspot image intensity.

Figure 4.30: *Analysis of the beam size and displacement using the lanex screen.*

smaller than the beam size the effect due to alignment position can be neglected, which was verified in the simulation. However in the case considered in this work the role of the alignment should be taken into account. The estimated values of horizontal and vertical displacement are respectively. The simulation including the corresponding beam spread and alignment was performed giving the overall correction factor of

$$k_{corr} = 0.050 \pm 0.015 \quad (4.5)$$

4.8.4 Measurements

In the experimental setup the diamond sensor and the low noise charge amplifier are fixed on a remotely controlled XZ translation stage (Figure 4.31). The signal acquisition consists of a 12-bit 500-MHz bandwidth digitiser, sampling between 400 MS/s and 3.2 GS/s (USB-Wavecatcher [112]), which was installed near the LEETECH setup and protected from radiation. The event triggering/synchronisation was done using the photo-injector laser pulses. A sample of 10000 events corresponds to the data acquisition of approximately half an hour.

The mutual alignment of the electron beam, LEETECH spectrometer, and diamond sensor is important to control the test sample characteristics. The absolute positions of the collimator box were aligned at the fabrication stage with a precision of 0.05 mm in such way that the centres of the collimators coincided with the centre of the vacuum

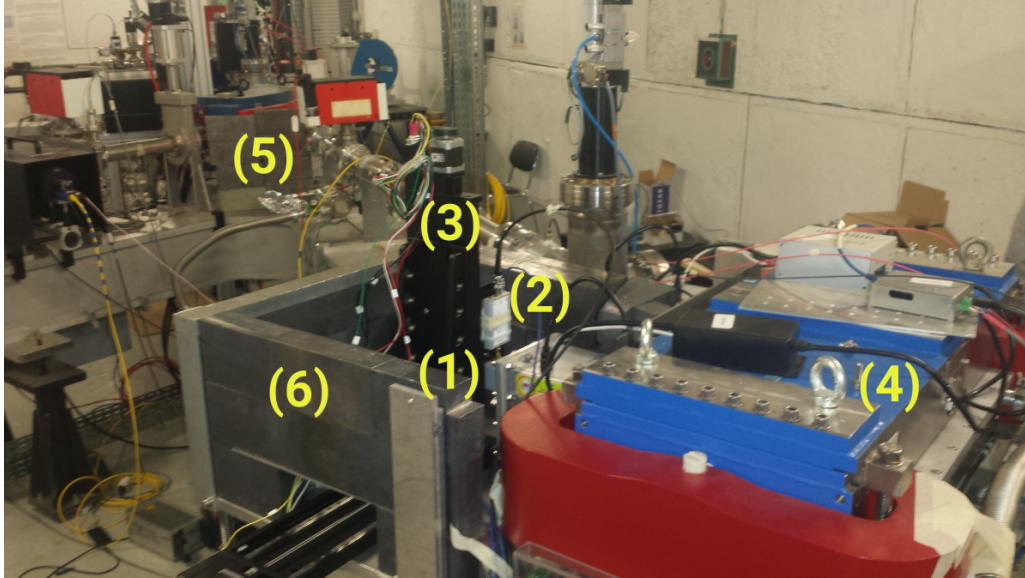


Figure 4.31: Photo of the experimental setup. The diamond sensor (1), charge sensitive amplifier (2), translation stage (3), LEETECH dipole magnet (4), PHIL photoinjector (5) and lead shielding around the detector area (6) are shown.

chamber.

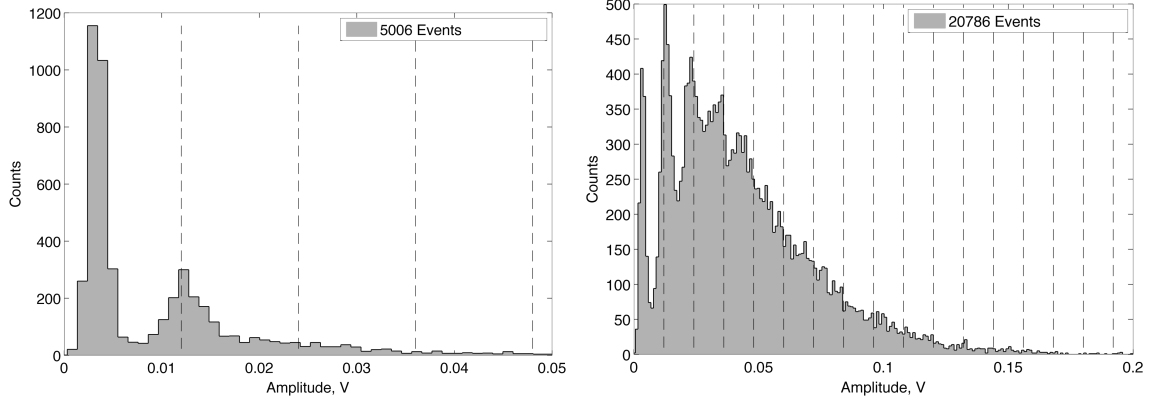
The PHIL beam position at the attenuator is visualised using the LANEX scintillator screen and controlled using the diamond sensor signal. Synchronous vertical scan of entrance and exit collimator positions reduces the effect of the stray field outside the dipole. Using the diamond sensor as a sensitive device positioned at the geometrical centre of the exit collimator, the magnetic field of 400 G is selected to maximise the number of electrons in the delivered sample. Complementary scan of the diamond sensor position aligns the diamond sensor with respect to the electrons coming from the spectrometer.

The working opening of the entrance collimator is selected to be $2.6 \times 1.8 \text{ mm}^2$. The opening of the exit collimator is varied in the measurements outlined below.

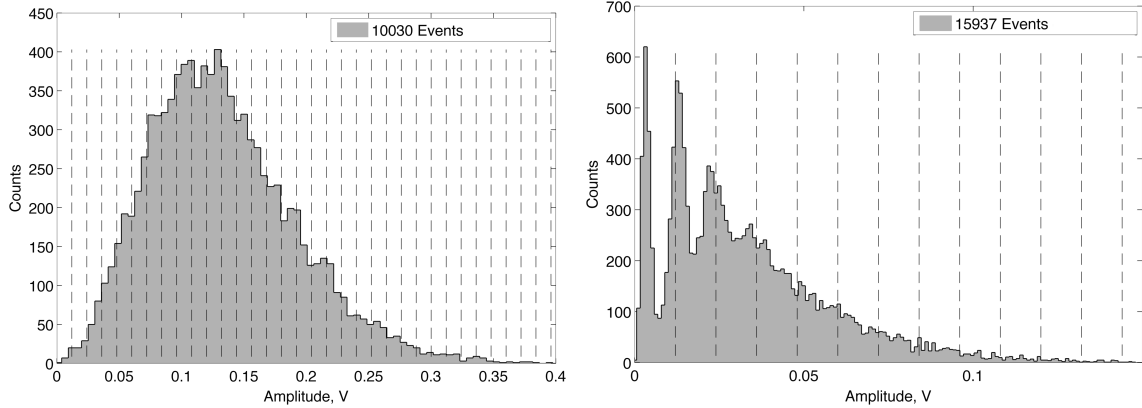
4.8.5 Results

Experimental results are shown in Figure 4.32.

Characteristics of the samples delivered by LEETECH can be adjusted by varying the PHIL bunch intensity, beam position and other machine parameters, attenuator material and thickness, position and opening of entrance and exit collimators. LEETECH platform should be calibrated depending on the above parameters.



(a) Collimator opening: Entrance 2.6x1.8 mm, Exit 1.2x3.1 mm. (b) Collimator opening: Entrance 2.6x1.8 mm, Exit 6.9x3.1 mm.



(c) Collimator opening: Entrance 2.6x1.8 mm, Exit 9.9x3.1 mm. (d) Collimator opening: Entrance 2.6x1.8 mm, Exit 19.9x20.6 mm.

Figure 4.32: Histogram of measured energy deposition in the diamond sensor. Vertical lines are separated by 12 mV and indicate the expected positions for different electron multiplicities. The first peak corresponds to the empty electron samples.

In Figure 4.32 the measurements of several electrons by diamond sensor at the LEETECH spectrometer are presented. The first peak (below 5 mV) in each sub-figure corresponds to the empty electron samples. The width of this peak reflects the noise of the charge amplifier. The percentage of the empty samples can be used to estimate the Poisson parameter. The vertical dashed lines are shown as indications of the expected signal positions from the samples containing different number of electrons. One can discriminate the peaks corresponding to the electrons multiplicity of 1, 2 and 3. The skewness in the distribution in Figures 4.32 is the natural property of the Poisson distribution for small

λ .

The increase of the opening of the exit collimator leads to the increase of the λ . The Poisson parameters for the experimental results in Figure 4.32 are presented in the summary Table 4.2. The errors in the experimental results were calculated by averaging the difference of estimations from mean and empty samples.

The simulation parameters were taken to be the same as in the experiment. In order to compare the simulation and the experimental results (Table 4.2) the beam size and beam alignment should be taken into account. Applying the correction factor from eq. 4.5 one obtains the efficiency parameter $\alpha_{corrected} = 0.12 \pm 0.04$ which is close to the experimental result of $\alpha_{experiment} = 0.11 \pm 0.02$.

Table 4.2: Comparison of experimental data and simulation results of the diamond sensor measurements.

Exit collimator	1.2x3.1	6.9x3.1	9.9x3.1	19.9x20.6	Efficiency α
$\lambda_{measured}$	0.7 ± 0.1	2.2 ± 0.2	2.8 ± 0.1	8.7 ± 0.9	0.11 ± 0.02
$\lambda_{simulation}$	8.0 ± 0.1	46.3 ± 0.1	58.9 ± 0.1	183.2 ± 0.1	2.3 ± 0.1
$\lambda_{sim,bs}$	0.7 ± 0.2	4.2 ± 1.4	5.3 ± 1.8	16 ± 5	0.21 ± 0.05
$\lambda_{sim,tot}$	0.4 ± 0.13	2.4 ± 0.8	3 ± 1	9 ± 3	0.12 ± 0.04

After taking into account all correction factors obtained values of λ as a function on the exit collimators opening were compared to the simulation results (Figure 4.33):

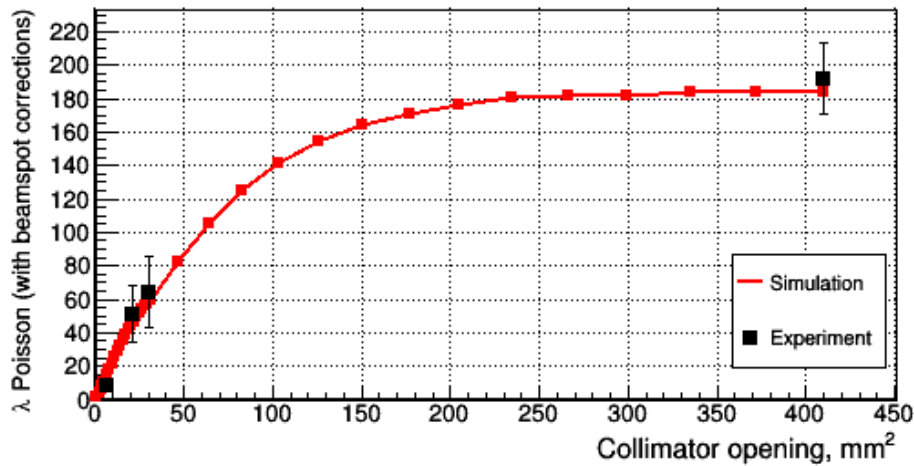


Figure 4.33: Comparison of $\lambda(S)$ dependence measured at LEETECH (black dots) with the Geant4 simulation results (red curve).

4.8.6 Conclusions

The calibration of the low-multiplicity mode of the LEETECH spectrometer was performed using the diamond sensor. Using a complete description of the LEETECH spectrometer a low-multiplicity operation is fully understood. A single efficiency parameter α selects an optimal LEETECH operation mode for detector measurements. We demonstrate LEETECH electron samples to follow the Poisson distribution with the parameter λ measured with the diamond detector. The estimation of the expected diamond detector response to a single electron passage is obtained. Measurement of the Poisson parameter in the wide range with a compact diamond detector is presented. Simulation results reproduce all the effects observed experimentally. Although diamond detector resolution of low-multiplicity peaks obtained is worse than that predicted by the simulation, one can discriminate the peaks corresponding to empty samples and to the samples containing 1 or few electrons. The origin of limited diamond detector resolution is caused by the Landau distribution of energy deposition in thin detectors. The use of the low-noise charge amplifier is expected to obtain more narrow distributions from individual electrons detection and further improve the peak resolution. A capability of diamond detector to discriminate low-multiplicity electrons in the vicinity of a beam line is demonstrated experimentally. Moreover, observation of the temporal evolution of the collected charge allows to follow variations of the parameters of the accelerator machine, providing a promising tool for the beam loss monitoring.

ELECTRON ENERGY LOSSES

As mentioned in Chapter 3, one of the key time projection chamber functionality is a particle identification, based on different energy losses by different types of particles in gas. At the same time, the precise electron dE/dx measurement at lower energies is important for different medical physics applications.

Electron energy losses are well described by Bethe-Bloch based models in energy range from a few keV.

In this chapter the several practices to obtain the dE/dx information from the experimental data are discussed. A review of existing simulation approaches to describe the particles propagation in gaseous media are compared.

5.1 Introduction

Charged particles passing through the matter loss their energy due to ionization and Bremsstrahlung processes [39]. Particle energy loss is described by a Bethe-Bloch formula in a wide range of $\beta\gamma$. However in the region of $\beta\gamma < 0.1$ where particles are non-relativistic, a theory description of the energy losses becomes less reliable. This is also the case when particles traverse a gaseous detector where the interactions with the gas consequent energy loss allows to reconstruct a particle's track and provide an important information on particle identity. A precision description of particle energy losses in gases is thus very important. In addition, gaseous detectors provide a powerful tool to measure dE/dx by reconstructing track curvature in a magnetic field (Figure 5.1).

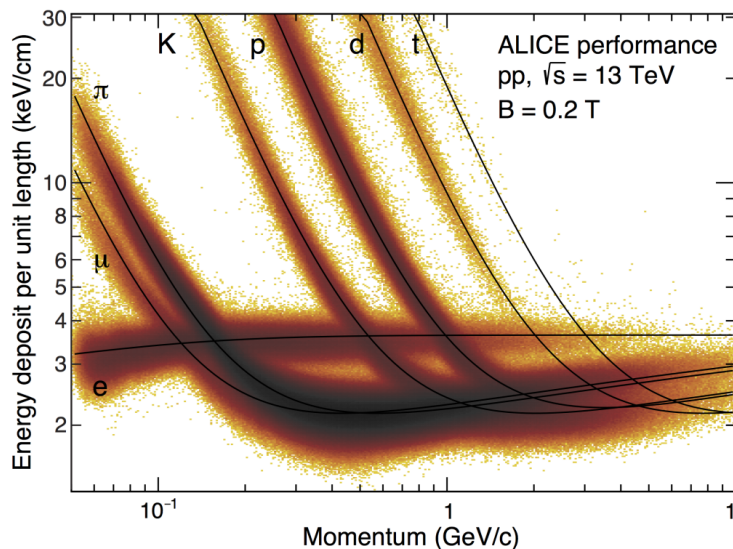


Figure 5.1: Results of the dE/dx particle identification with the ALICE time projection chamber [113]. Several types of particles can clearly be resolved by precise measurement of the energy loss and momentum via curvature in magnetic field.

Modern gaseous detectors and MPGD offer more precise techniques such as charge, cluster counting and single electron counting. This section is focused on the electron energy loss measurements in the gaseous media.

5.2 dE/dx calculation algorithms

The gaseous detectors can return the information about the track of passing particle as a collection of hits with their properties: 2D or 3D coordinate, measurement related to

the deposited energy (e.g. pulse height, time-over-threshold counts), time of arrival. In this section the description of the algorithm of how to extract the dE/dx of the primary particle from this information will be given.

The energy losses follow the Landau-like distribution [29, 114, 115]. The main challenge for the PID is to efficiently separate the distributions from different types of particles. Due to the long Landau tails the distributions overlap and separation power is decreased.

Two standard ways to obtain the dE/dx are the truncated mean and cluster counting.

5.2.1 Truncated mean

In this method the measurement proportional to the energy deposited in a primary ionization is used. This is usually an integrated charge from the detector anode. Due to proportionality the distribution of these measurements also follows the Landau function. The goal of so-called truncated mean procedure is to eliminate the long tails and enhance the dE/dx resolution.

The algorithm operates as described in the following. First, each track is divided by segments of equal length, typically several mm. The energy depositions on each segment along every single track are sorted and some fraction with the highest values is discarded. Then the mean deposited energy value (e.g. truncated mean) is calculated through the remaining segments, one value per track. Starting from some value of truncation fraction the histogram of truncated means starts to follow the Gaussian distribution (Figure 5.2) with well defined momenta mean and RMS. The ratio RMS/mean of this distribution is taken as the dE/dx resolution.

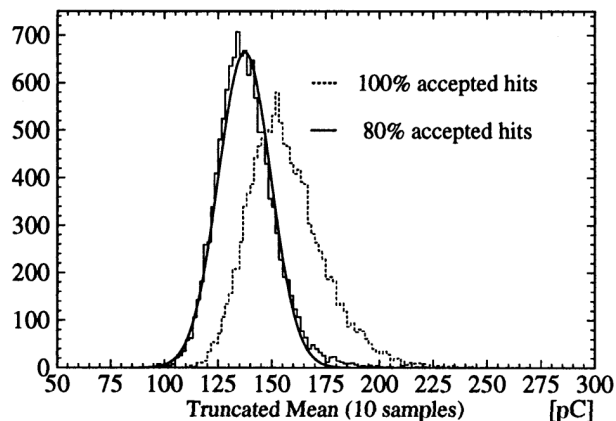


Figure 5.2: Measured and 20% truncated dE/dx distributions [116]. The shape of the truncated distribution has lower skewness, which improves the resolution

The best value of the truncation fraction is picked by optimization of the dE/dx resolution. A typical behavior of this dependence for the KLOE drift chamber is shown in Figure 5.3 for 50 GeV/c pion beam with two different detector configurations [117]. The whole measurements set (100%) has significant Landau tails, so introducing the truncation and increasing the fraction of discarded measurements improves the dE/dx resolution to a certain point. From the other side, discarding the measurements also decrease the statistics. When the shape of dE/dx distribution skewness becomes low enough, further decrease of accepted hits fractions leads to dE/dx resolution increase. The optimal truncation fraction is thus determined by the minimum of the curve, similar to that shown in Figure 5.3, which can vary depending on measurements conditions.

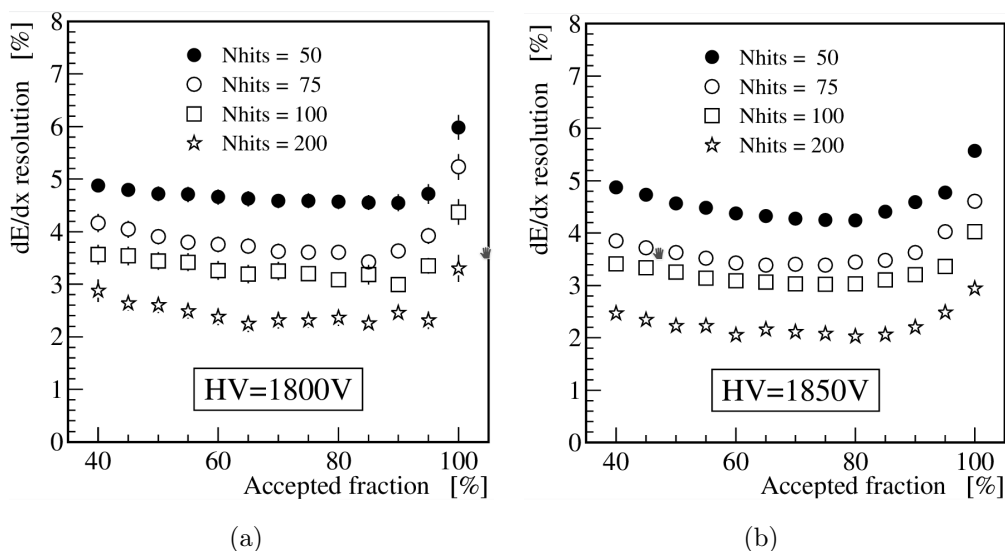


Figure 5.3: The truncation of dE/dx distribution allows to improve the resolution and particle identification capability. Individual dE/dx measurements of 50 GeV/c pion beam are sorted and some fraction of them with the highest values is discarded. Result of applying truncated mean method is shown: dE/dx resolution as a function of discarded measurements fraction for different track lengths and detector configurations [117].

Different distributions on the plots correspond to the tracks reconstructed from different number of hits. This dependence is shown in the Figure 5.4 for the fixed detector configuration and value of accepted hits fraction. The dE/dx resolution is improved from about 5% for 50 hits per track to about 2.5% for 200 hits per track (Figure 5.3(a)). However in the conditions when the energy of the beam corresponds to the Bethe-Bloch plateau region and variations of particles energy are small, one can consider that the

variations of energy loss from track to track are also small. Thus several tracks can be artificially combined in a single long track and a dependence similar to the one shown in the Figure 5.4 can be studied.

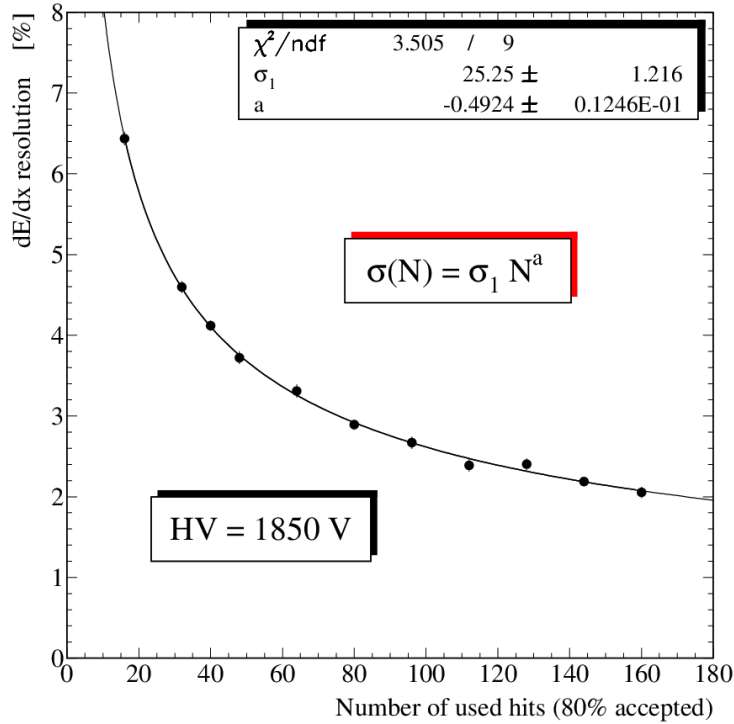


Figure 5.4: dE/dx resolution as a function of number of hits on each track fitted by function $\sigma(N) = \sigma_1 \cdot N^a$ [117]

5.2.2 Cluster counting

A number of clusters along the track corresponds to the number of primary ionizations. Unlike the deposited energy, the number of clusters per track follows Gaussian distribution (Figure 5.6(a)) [118–121]. In some cases cluster counting technique it has gives better or comparable result than the calculation of truncated mean of energy deposits. These techniques can be combined together to improve the resolution as demonstrated in reference [118].

For wire and strip-readout detectors, such as drift chambers, a separation of clusters is implemented by the waveform analysis (Figure 5.5), where each peak corresponds to an individual cluster. The main problem in this approach is the pulses overlap, when several close clusters are erroneously interpreted by analysis algorithm as a single one. In

order to enhance the time resolution, the He-based gas mixtures where the drift velocity of released electrons is about 2.5 times less and ionization density is about 5 times less than in Ar-based mixtures [121], are advantageous for the cluster counting technique.

Neither peaks amplitude info nor area information is used in a basic cluster counting technique, however they can be used to improve cluster separation.

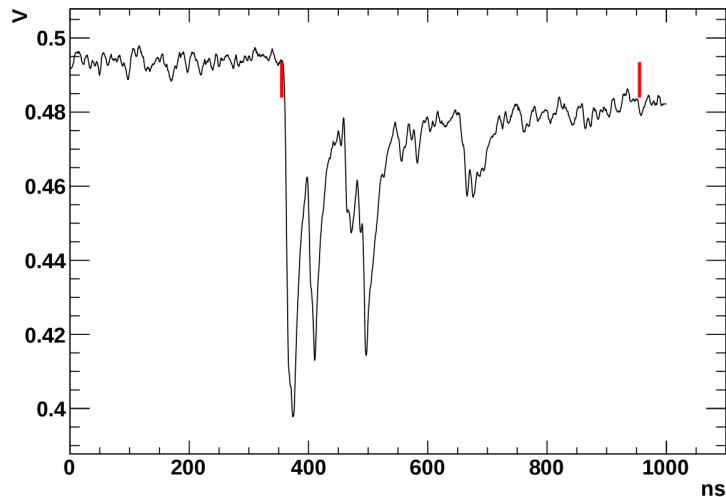


Figure 5.5: *Sample waveform acquired from the drift chamber prototype at TRIUMF [118]. Red markers indicate the integration time margins.*

As addressed in section 5.2.2, due to the secondary ionization a cluster may consist of several (up to hundreds) electrons, which results in a higher amplitude of the corresponding pulse. However, unlike the cluster statistics, the electron number statistics follows a Landau-like distribution (Figure 5.6(b)) similar to the deposited energy distribution. This means that in the case of a single electron detection (like with large diffusion and high-granularity pixelated anode) the algorithm to group the signals from cluster electrons is needed to apply the cluster counting method.

5.3 Simulation

A number of software tools are available to study the energy loss of and electron in gases. The aim of the simulation is to predict and validate the measurements, so we will focus on the number of produced secondary electrons (measurements, input data for the analysis) and the deposited energy (the final result of the analysis). Simulation with HEED, Geant4 and Degrad tools is discussed in this section.

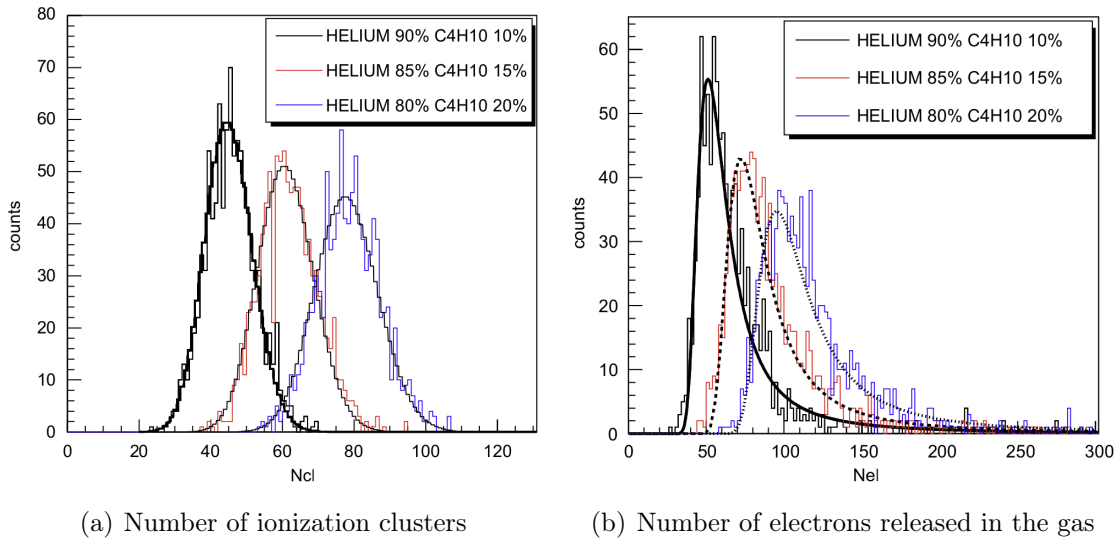


Figure 5.6: dE/dx parameters for particles of 50 GeV in Helium/isoButane gas mixtures [121].

5.3.1 HEED simulation

The HEED [122] (derived from High Energy Electro Dynamics) developed by I. Smirnov is a tool to compute the amount of ionization and location of primary clusters along the track. It implements the PhotoAbsorbtion Ionization model (PAI) proposed by Allison and Cobb [123]. A PAIR (photoabsorption ionization and relaxation) modification of the PAI model was also developed to model the transverse distribution of initial ionization aside from the track.

First versions were written in FORTRAN 77, later interfaced to the Garfield which is a conventional tool for gaseous detectors simulation. Moving to C++, the new version of HEED was developed in 2003-2005 with a possibility to specify the detector 3D space. It comes as a part of Garfield++ as a tool to compute the primary ionization.

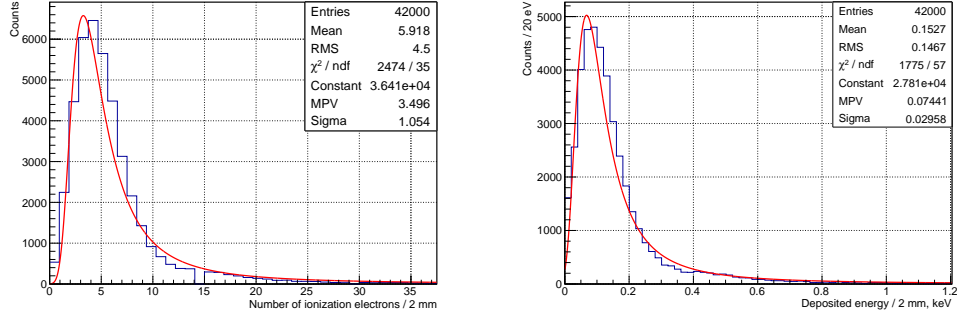
Tracks simulation

Using the approach described in the previous section, the simulation was performed to estimate the distribution of clusters along the track and derive the relation between the number of clusters and the energy deposited by primary particle.

Results for 3 MeV electrons passing through a 56 mm thick volume of He/isoButane 80/20 gas mixture are shown in the Figure 5.7.

The number of clusters distribution for the same conditions is shown in Figure 5.8.

The cluster size distribution and deposit energy per cluster are shown in Figure 5.9:



(a) Total number of electrons released in primary ionization collisions per 2 mm track gap. (b) Deposited energy per 2 mm track gap.

Figure 5.7: *HEED simulation results for e^- of 3 MeV total energy traversing 56 mm thick volume of He/isoButane 80/20 gas mixture.*

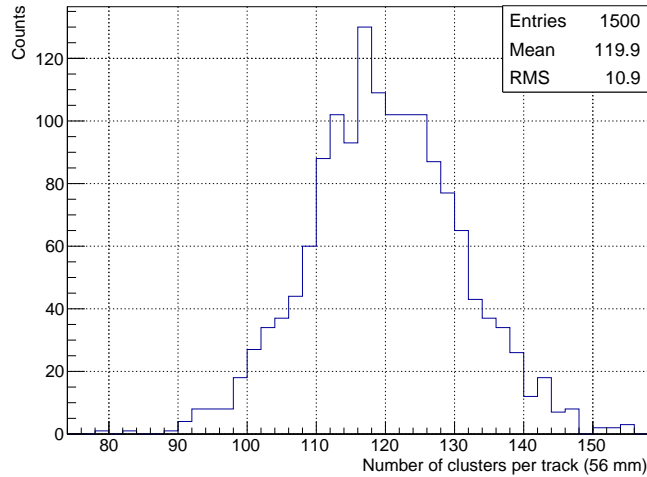
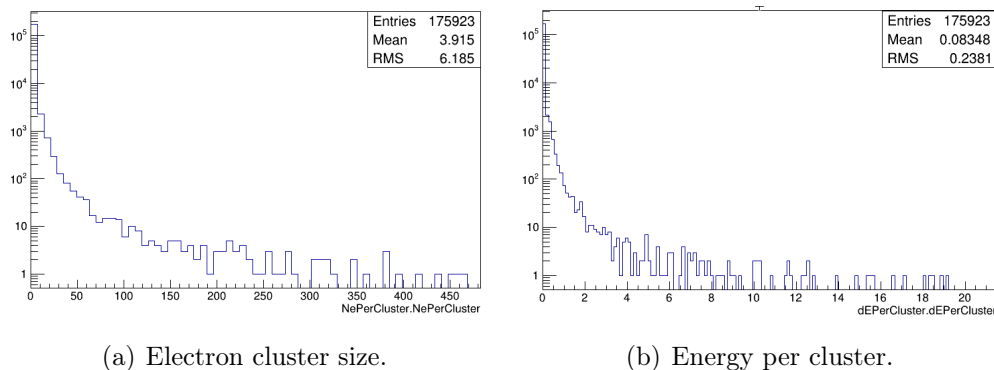


Figure 5.8: *Number of clusters per track distribution obtained with the HEED simulation for e^- of 3 MeV total energy.*

5.3.2 Geant4

Geant4 is a powerful tool for simulation of majority of physics processes for passage of particles through matter. Its application to the description of gaseous detectors is somewhat limited. So far the results for ionization electrons transfer do not agree with other simulation tools and experimental data. However, Geant4 succeeds to reproduce



(a) Electron cluster size.

(b) Energy per cluster.

Figure 5.9: HEED simulation results for clusters produced by e^- of 2.2 MeV total energy in He/isoButane 80/20 gas mixture.

the primary ionization clusters distribution [ALICE paper], [124], which can be used as an input to the simulation of subsequent stages.

A simple detector geometry consisting of a box filled with the gas mixture was implemented. The goal of the simulation was to reproduce a primary ionization along the track and to obtain the energy losses expected from the measured primary ionization.

Several approaches can be used in Geant4 to obtain the energy losses in the detector: to construct a sensitive detector and to process hits in a separate class or to use the SteppingAction class to consider each step along the track. The latter approach was adopted below because of its flexibility. It also allows to follow particles in any physical volume without creation of a separate SensitiveDetector class.

PhysicsLists

There are several choices of PhysicsLists that can be used in gaseous detector simulation, the detailed description of them can be found in [125]. A comparison for some of them for low energy electrons can be found in [126], demonstrating a good agreement between models to describe the mean value of deposited energy for the electron energy range between 1 keV and 10 MeV.

The distribution of the deposited energy in the He/isoButane 80/20 gas mixture is consistent for all modular physics lists with a deviation for *G4EmStandardPhysics_option4* and *G4EmPenelopePhysics* towards lower energies (Figure 5.10(a)). However, the number of primary ionization collisions, i.e. number of clusters, is significantly lower for these two models than for others (Figure 5.10(b)). Nevertheless, the measurement data for MIPs as well as the results from the HEED and Degrad simulation give a value of approxi-

mately 2 ionization collisions per mm, which is far higher than the mean value of all the distributions in Figure 5.10(b), obtained for a 56 mm thick gas layer.

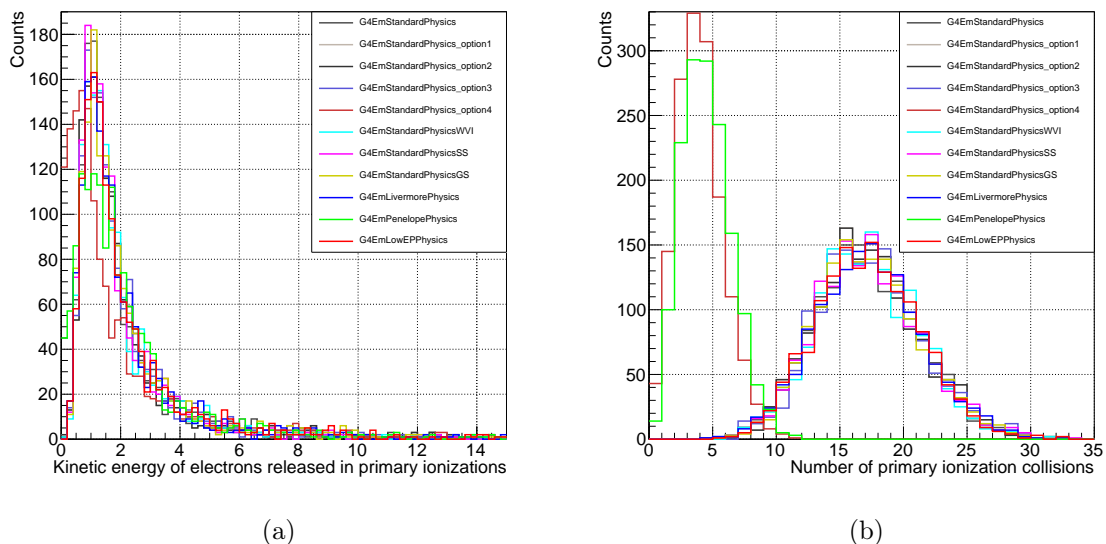


Figure 5.10: Comparison of Geant4 models for 3 MeV electrons passing 56 mm of He/isoButane 80/20 gas mixture.

To model the so-called straggling function (deposited energy distribution) the two following models are available in Geant4: an empirical parametrisation (the model of standard sub-library (*G4UniversalFluctuations*) and the photo-absorption ionisation model (PAI) which considers all ionisation collisions [127]. The latter is preferred for an accurate simulation of energy loss and pair production in sensitive volumes, though the performance is slower than for the standard Geant4 model. Alternatively the PAI-photon model can also be used. It provides a sampling of energy transfer to media excitations, enabling the X-rays production. In Ref. [128] another advantage of PAI models is claimed. The authors found results to be independent of the production thresholds.

The simulation of 3 MeV electrons passage through 56 mm of He/isoButane 80/20 was repeated for the standard PhysicsLists with the PAI model enabled in a gas region. The results are in good agreement both for the deposited energy and number of primary ionizations (Figure 5.11). The PAI results for the *G4EmStandardPhysicsWVI*, *G4EmStandardPhysicsSS* and *G4EmStandardPhysicsGS* are absent because the simulation do not converge and therefore not shown on the plot.

The benefit of using the PAI is demonstrated some estimation of the underproduc-

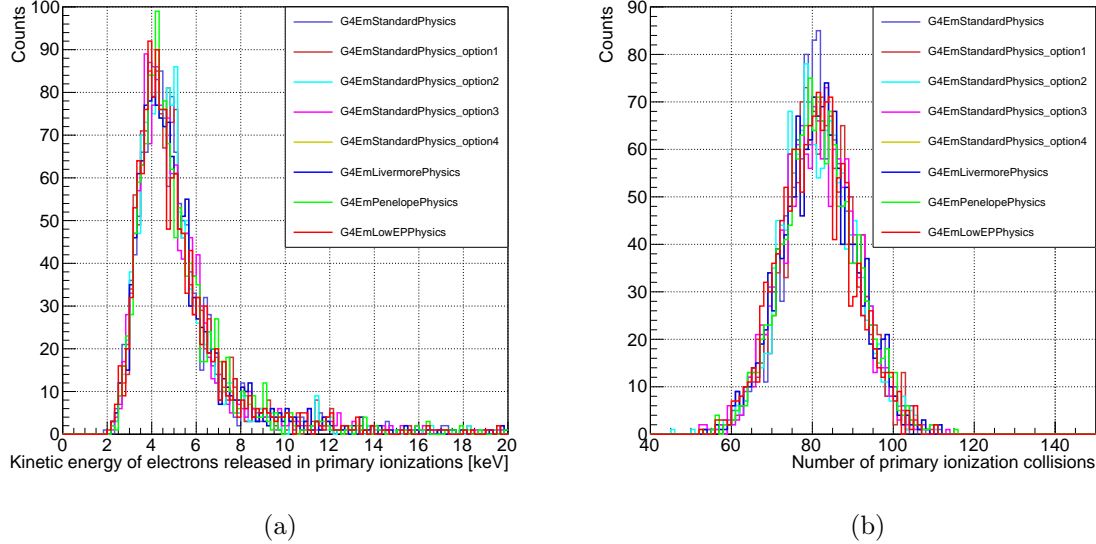


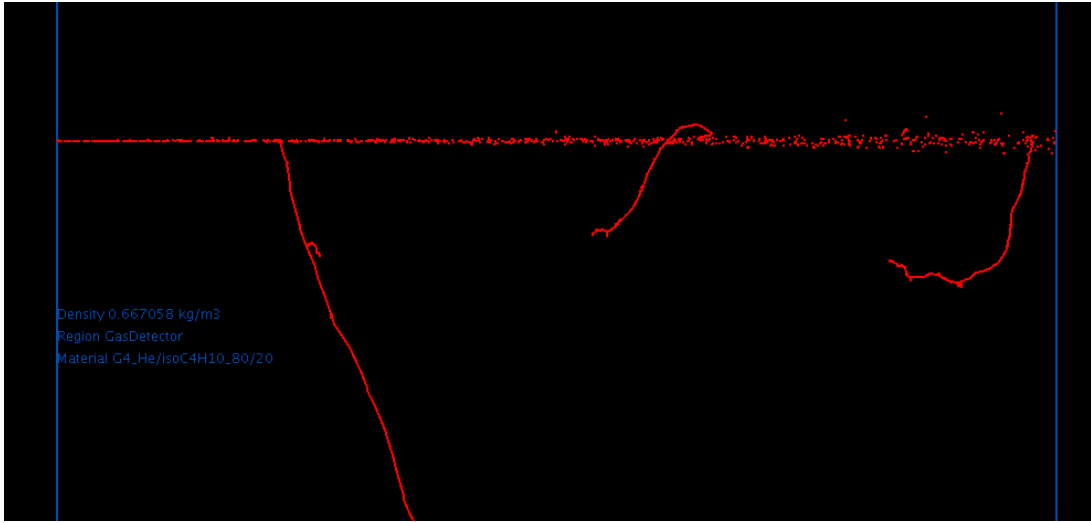
Figure 5.11: Comparison of *Geant4* models for 3 MeV electrons passing 56 mm of He/isoButane 80/20 gas mixture with PAI enabled in a gas region.

tion of electrons in ionizing collisions is not so critical anymore. Since the results are similar across different physics list, below we choose to compare the *Geant4* results with the other simulation tools. According to the review in [125] and *Geant4* documentation (Appendix A.1) the *G4EmStandardPhysics_option3* was chosen.

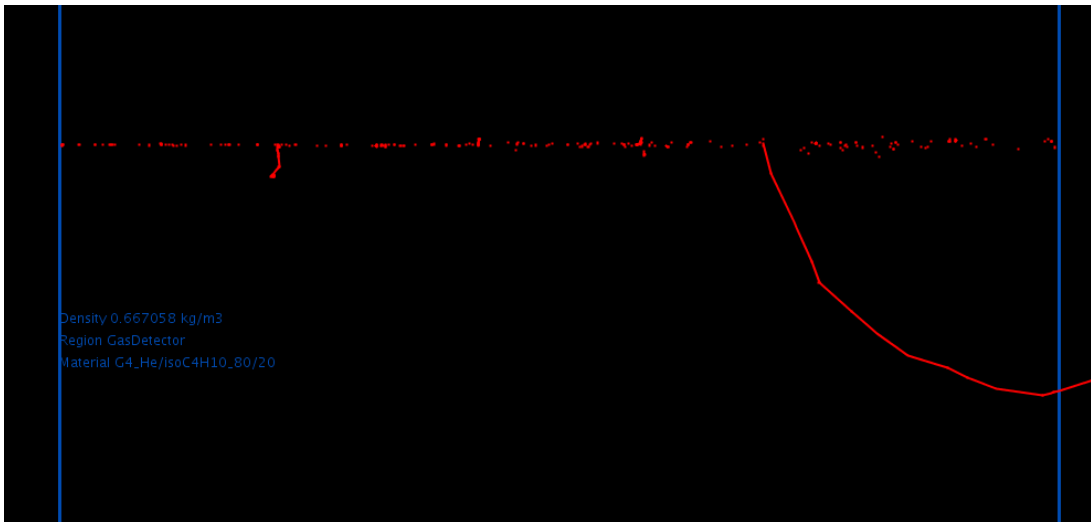
In the Figure 5.12 the results obtained with 100 events of 3 MeV electrons passing through 1 cm of He/isoButane 80/20 gas mixture are shown with (Figure 5.12(a)) and without (Figure 5.12(b)) the PAI model. Contrary to the HEED tool, *Geant4* takes into account the Coulomb scattering so primary particle trajectories are not perfect straight lines.

Stability of the simulation model

There are two types of selection criteria in *Geant4*. First limits the particle production (*production thresholds*) [129] and second defines the range of particle tracking. By default the latter is disabled and all the particles are tracked down to zero kinetic energy. However, sometimes it is useful to enable it to speedup the simulation, so the *G4UserLimits* can be used for this purpose [130]. For the study of primary ionization in fairly thin (several cm) gas volumes one does not need a very large statistics and a few thousands of events is sufficient to obtain a well-binned straggling function histogram (Figures 5.10, 5.11).



(a) PAI implemented



(b) PAI not implemented

Figure 5.12: Trajectories of electrons, produced in primary ionization collisions by 3 MeV electron beam in 10 mm of He/isoButane 80/20 gas mixture (100 events overlapped).

However, the precision is important so the user selection criteria were not applied at all.

The production thresholds are typically set in terms of length, which a produced secondary particle can pass in material. The default value in Geant4 is 1 mm and can be adjusted manually per each type of particle and per each region. In each material this value is internally converted to the minimum energy value at which the particle still can produce secondaries. For our case when we are interested only in a single logical volume of gas, the

explicit energy range for the secondaries production can be set in the PhysicsList using the `GetProductionCutsTable()` – `> SetEnergyRange(G4doublelowedge, G4doublehighedge)` method.

The dependence of the energy loss straggling function on the secondaries production range was studied for 3 MeV electrons passing through 56 mm of He/isoButane 80/20 gas mixture. Higher production threshold was fixed to the value of 100 GeV, while a lower threshold varied in a range of [1...100] eV. The results on the production range are shown in Figure 5.13.

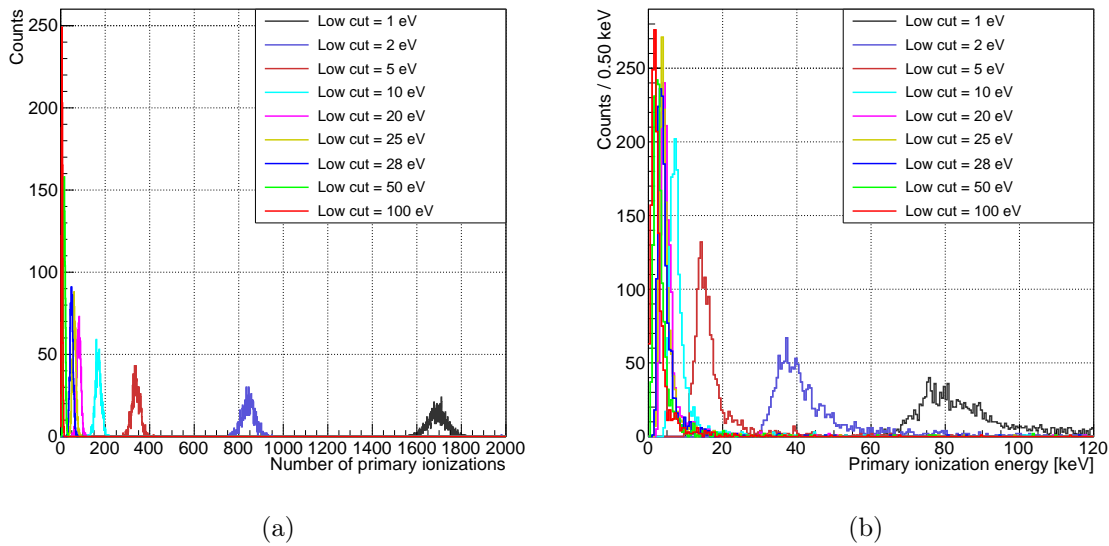


Figure 5.13: Comparison of Geant4 PAI results for the different lower production threshold values.

The number of collisions and the deposited energy obtained from simulation depend on the lower threshold. The ionizing collisions at very low values of threshold are not detectable since the minimum ionization potential for He/isoButane gas mixture is 10.76 eV. The threshold can be set to the value that yields an agreement with other simulation tools such as Degrad and HEED. Results from the Figure 5.13 for the threshold values of 25...100 eV are shown in the Figure 5.14.

From the Figure 5.14 one can conclude that the energy loss dependence is not very strong for the lower production threshold values above the minimum ionization potential of the gas. Oppositely, a strong dependence for the number of primary ionization remains, so a deeper study of the production threshold influence on the energy losses in Geant4

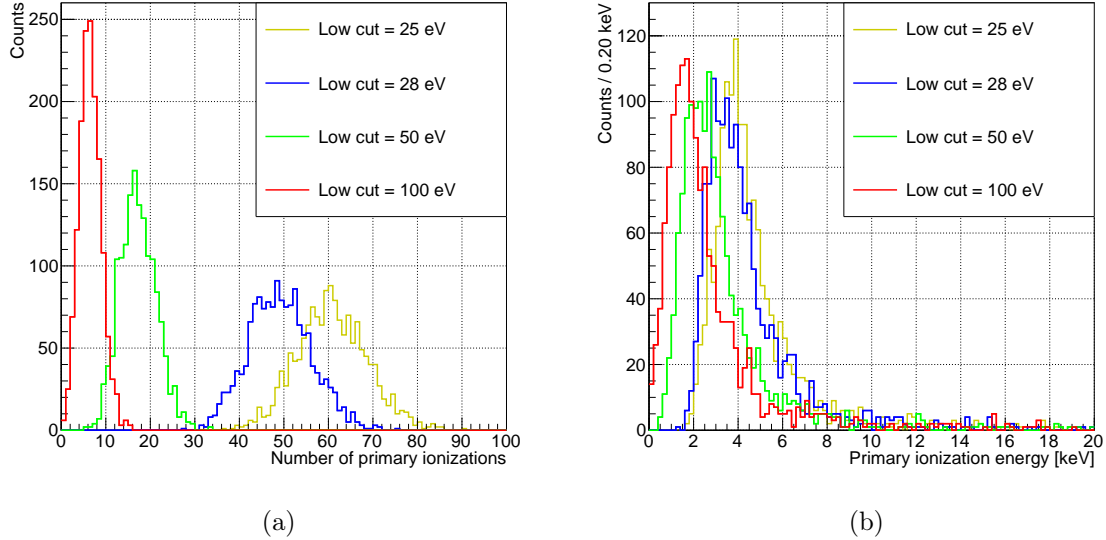


Figure 5.14: Comparison of Geant4 PAI results for the different lower production threshold values.

is required to find a stable region for the Geant4 PAI model and consistency with the HEED, Degrad and the experimental data for MIPs.

First the PAI behavior within Geant4 was studied, for both deposited energy and number of primary ionizations. These two quantities are particularly important since the energy loss is recovered from the number of ionization electrons, counted in experiment.

Since the PAI stability was declared in terms of deposited energy [128], the following quantities were studied:

- Energy, deposited by all particles in the detector volume (E_{dep})
- Total kinetic energy of electrons, produced in primary ionization collisions (E_{kin})
- Total kinetic energy of particles leaving the detector ($E_{kin\ lost}$)

The difference:

$$\Delta E = E_{dep} - (E_{kin} - E_{kin\ lost}) \quad (5.1)$$

is available to produce the electron-ion pairs and should be compared to the value $N_{prim} * W$, where the N_{prim} is a number of primary ionizations and W is the energy that is spent, on average, for the creation of one *free* electron [41]. Thus two derivative quantities were added:

- $E_{kin} - E_{kin\ lost}$
- $E_{kin} - E_{kin\ lost} + N_{prim} \cdot W$,

where the W value for gas mixtures was calculated with HEED. For He/isoButane 80/20 it is equal to 32.94 eV. The quantities described above as a function of lower production threshold are shown in Figure 5.15.

The deposited energy behavior at low values of threshold (< 14 eV) is overestimated which is reflected in Figure 5.13(b) results. Moreover, in this range, the E_{dep} (green) curve and the $E_{kin\ created} - E_{kin\ lost}$ (magenta) curve approach each other, meaning that no energy is required to create the electron-ion pairs. This region is thus unstable due to E_{dep} strong dependence on the threshold value and simulation yields unphysical values.

Above the certain value of 14 eV the deposited energy E_{dep} becomes stable. As mentioned above it is to be compared to the $E_{kin} - E_{kin\ lost} + N_{prim} \cdot W$ curve and they should be equal, with possibly some small fluctuations since W is an average value. However we observe a different behavior with a region where $E_{kin} - E_{kin\ lost} + N_{prim} \cdot W$ value exceeds the E_{dep} .

The energy, required to produce an electron-ion pair cannot be lower than the minimum ionization potential of the gas mixture. For our case it is 10.74 eV for isoButane, so the Figure 5.15(b) was reproduced with the quantity of $E_{kin} - E_{kin\ lost} + N_{prim} \cdot I$ (Figure 5.16).

A new intersection point is 21 eV, which indicates a minimum valid value for the lower production threshold. The cause of this difference for the higher production thresholds is fully understood. A possible explanation is a mixed ionization of He and isoButane potentials. Another contribution to this difference comes from a shift in simulated number of primary ionization collisions.

The intersection point (start of E_{dep} stability region) depends also on the gas and components concentration in the gas mixture. It is important to establish this dependence as a function of W and I values.

At this point the self-consistency of Geant4 deposited energy simulation was established. The PAI model gives a stable result starting from a given value of Geant4 lower production threshold (14 eV for He/isoButane 80/20). However, there is another region (from 14 to 21 eV) where simulation yields unphysical result. The reason of that can be overestimation of the primary ionization collisions, which will be studied in the following sections.

5.3.3 Degrad simulation

Degrad is a tool developed by S. Biagi [131]. It is able to calculate atomic cascades initiated by X-ray photons or electrons interacting in a gas. Degrad returns the number of ionizations, excitations and the position of each thermalized electron as well as many other quantities. Currently Degrad is the first choice of the RD51 collaboration at CERN for simulation of primary gas ionization.

Program interface

The Degrad is a single-file Fortran program, which is compiled and launched in a conventional way. It requires 5 input cards, each containing corresponding simulation parameters and explicitly documented in the source code.

Performance

Unlike the HEED and Geant4, the Degrad continues the simulation until the particle energy reaches the user-defined thermalization limit (default value is 2 eV) in an infinite gas volume. The simulation is therefore slow, taking about 5 minutes to simulate 10 events of 3 MeV electrons in He/isoButane 80/20 gas mixture.

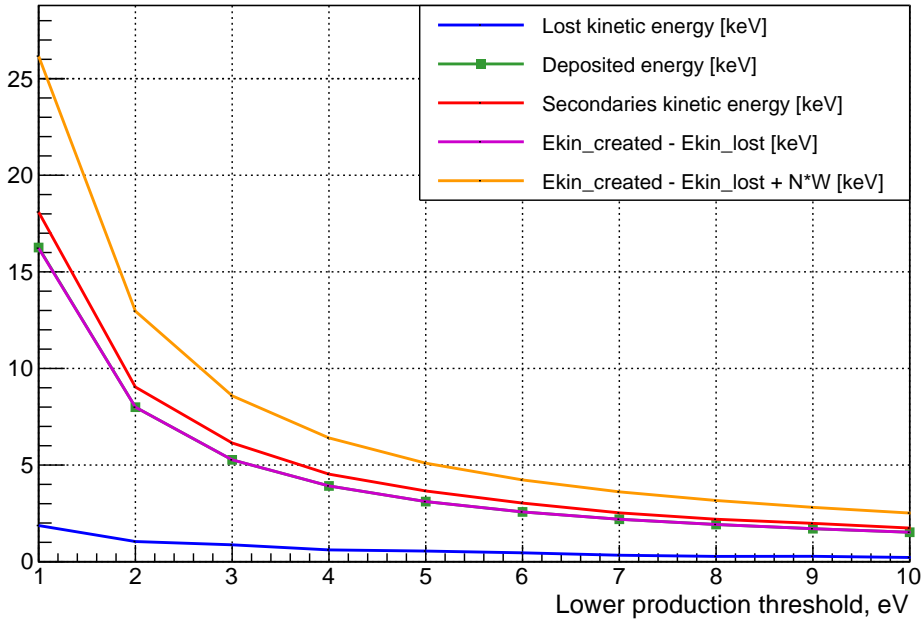
Tracks simulation

Event samples of 3 MeV electron trajectories are shown in Figure 5.17.

The zoom of a single event for the z axis range of [0...56] mm is shown in Figure 5.18. Note the difference in axes ranges, so the track is straighter than it appears on the figure. In the top part of the figure the delta-electron can be seen, so the Degrad out-of-box gives the complete track simulation making it an attractive tool for simulation of primary and secondary ionization.

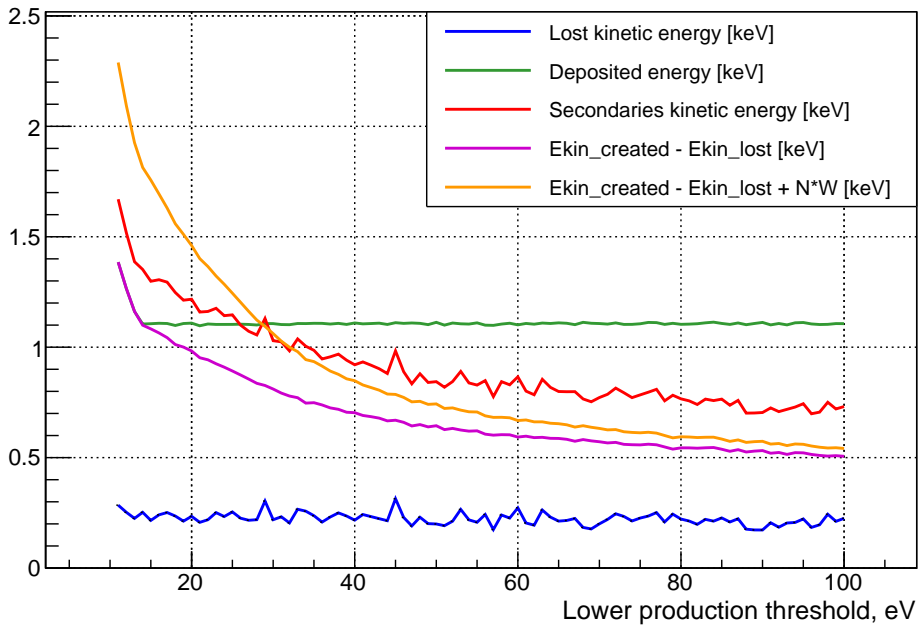
The tracks simulated by Degrad were converted to the format, used to store the data from the Micromegas/InGrid detector and analyzed by the developed track reconstruction software tool (Section 6.2). Results of the reconstruction along with the obtained dE/dx distributions are shown in Figure 5.19 and Figure 5.20 respectively.

He/iC₄H₁₀ 80/20



(a)

He/iC₄H₁₀ 80/20



(b)

Figure 5.15: Deposited energy as a function of lower production threshold.

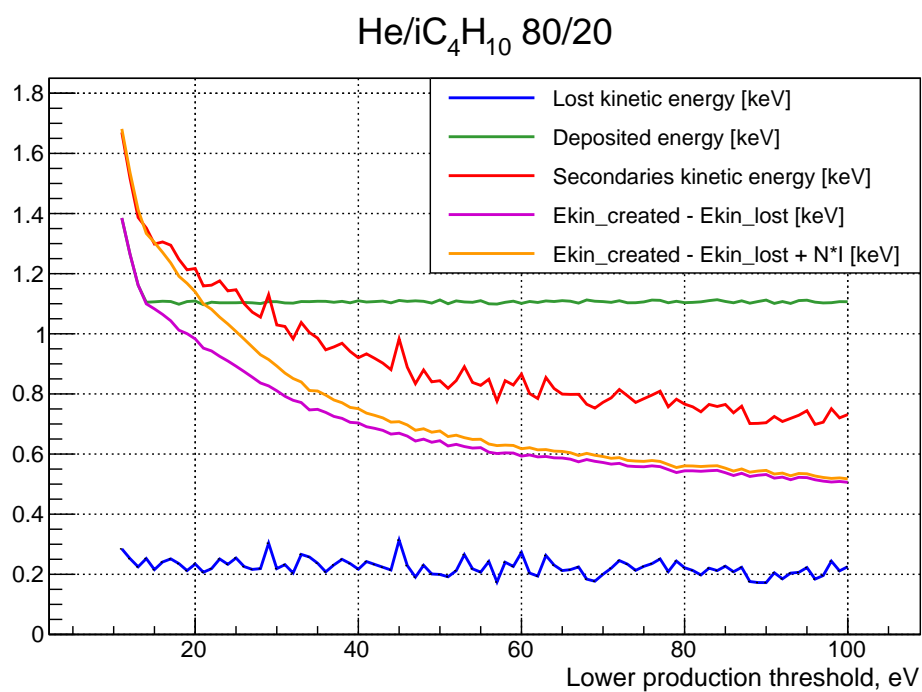


Figure 5.16: Deposited energy as a function of lower production threshold.

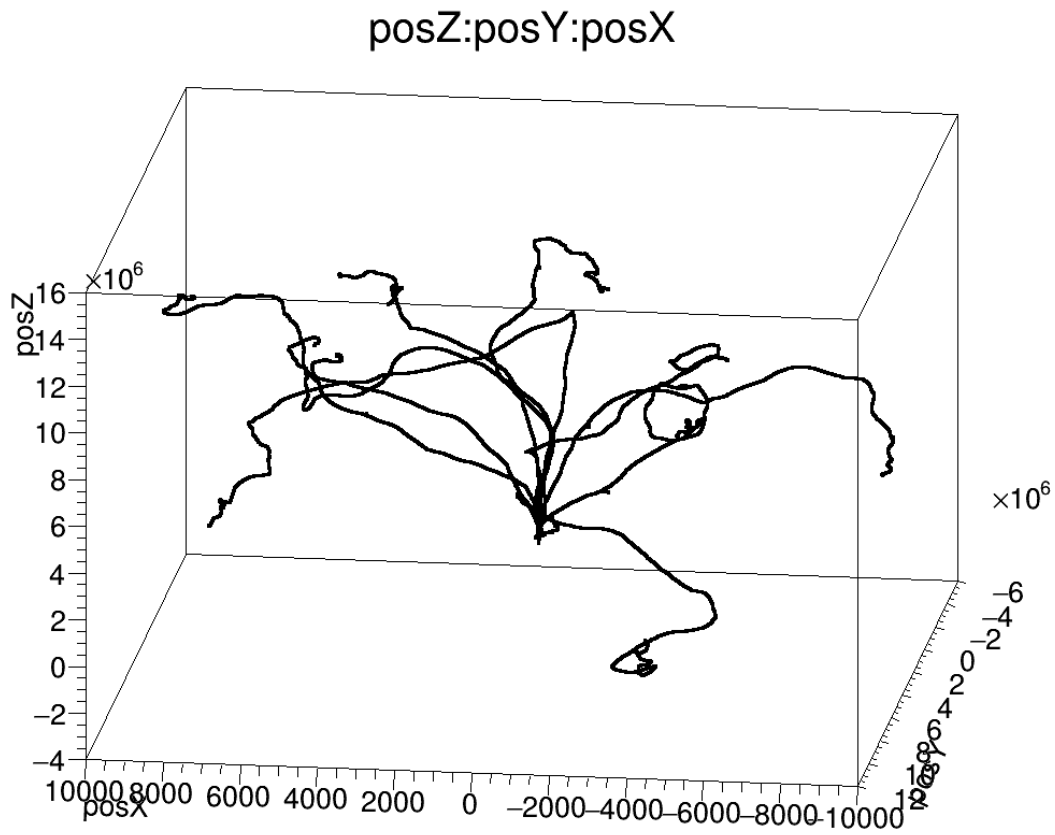


Figure 5.17: Trajectories of 3 MeV electrons simulated by Degrad (10 events overlapped). All the dimensions are currently in μm

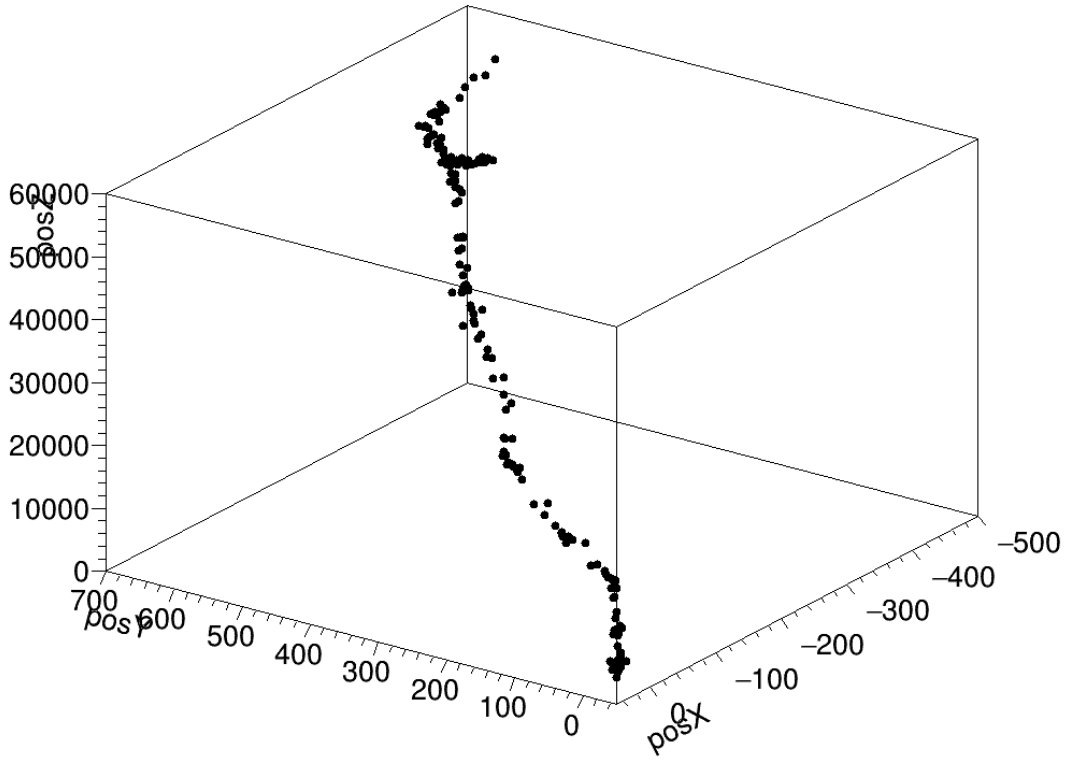


Figure 5.18: Trajectories of 3 MeV electrons simulated by Degrad (10 events overlapped). All the dimensions are given in μm

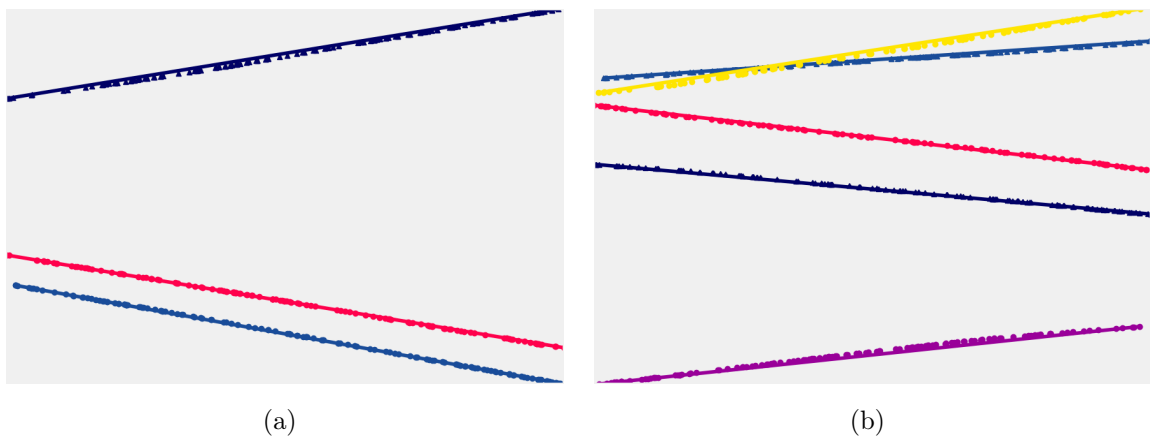


Figure 5.19: Tracks of 3 MeV electrons in He/isoButane 80/20 gas mixture, simulated by Degrad and reconstructed.

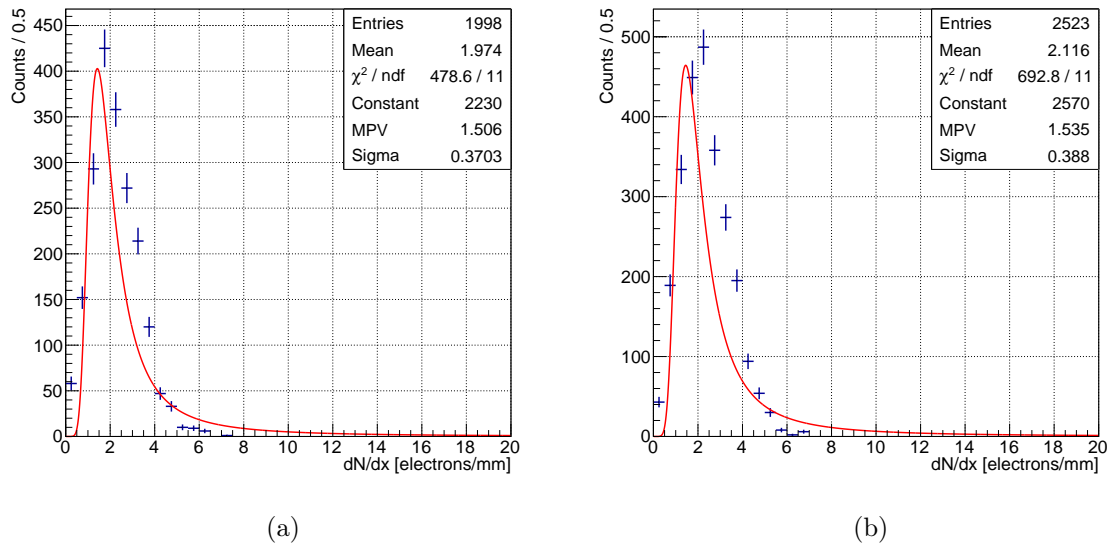


Figure 5.20: dE/dx distributions of 1.3 MeV (a) and 3 MeV (b) electrons, simulated by Degrad.

LARGE-AREA INGRID MODULE CHARACTERIZATION

Future large-scale experiments often require precise, low material, radiation resistant tracking covering large surface. Large-area novel MPGD provide a promising solution for this demand. However, it is important to demonstrate a functionality of a large-area MPGD.

The test beam campaign to characterize large-area Micromegas/InGrid detector and to measure the electron dE/dx took place in February 2017 with the 96-chips InGrid module (Figure 6.1), using LEETECH as a source of electrons. This chapter presents the characterization results, the track reconstruction technique optimization for a multiple scattering environment. and first results on the energy loss of low-energy electrons.

6.1 Experimental setup

The studied 96-chips Micromegas/InGrid module is shown in Figure 6.1. The module was placed to the detector area after the LEETECH exit window (Figure 6.2). The gas used was He/isoButane 80/20. Height of the drift region was about 17 mm. To ensure a maximum InGrid electron detection efficiency, the grid voltage was set to 470 V.

To efficiently count the electrons released in primary ionization collisions the diffusion should be large to avoid double hits of the Timepix pixels. Therefore the drift field was set to 1200 V which corresponds to about $200 \mu\text{m}/\sqrt{\text{cm}}$ diffusion (Figure 6.3).

The Timepix pixels were set to the TOT mode. This allows to measure the hit charge and after the track reconstruction compare the performance of truncated mean method and cluster counting technique.

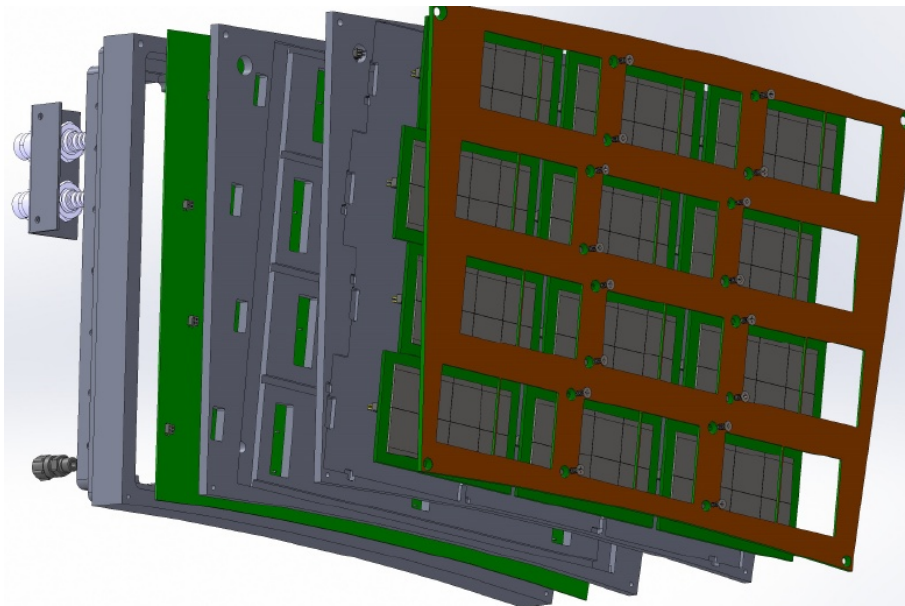
LEETECH dipole current was varied in the entire range of the values at which the reconstructed tracks were obtained. Aluminum targets were chosen accordingly to benefit from large electron multiplicity for the given energy, defined by the dipole magnet (Figure 4.20). Collimator openings were adjusted for each measurement to limit the number of tracks in the event.

More than 100 runs were acquired in total, efficiently covering the energy range between 1.3 and 2.76 MeV.

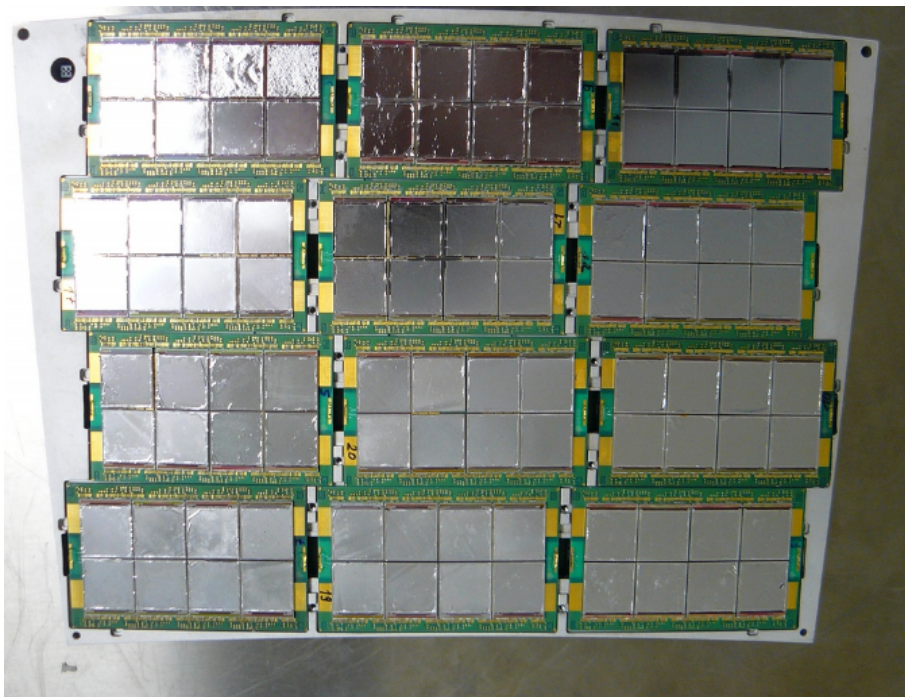
6.2 Track reconstruction

An important step of the data analysis from the tracking detector is the track reconstruction. Based on these results all the detector characteristics, such as spatial, time, dE/dx resolution can be extracted.

There are two different main approaches for the track reconstruction - global, which uses the whole data frame to simultaneously find all the tracks, and local, which iteratively starts at a given point and sequentially goes through the hits of the data frame, assigning them (or not) to the considered track. Typical example of the local approach is the Kalman filter [133–135], which estimates possible locations of the track hits, checks the data whether the hits were acquired in the predicted regions and extrapolates the track according to the best match of the new hits to the filter prediction. Typically the local methods are faster and they scale better on the large datasets, but their drawback is a high sensitivity to the detector dead regions, where no hits are acquired and the algorithm may stuck and mark the track as completed. This is potentially the case of the InGrid module



(a)



(b)

Figure 6.1: 96-chip Micromegas/InGrid module, developed at Bonn University: CAD 3D design (a) and assembled module (b).

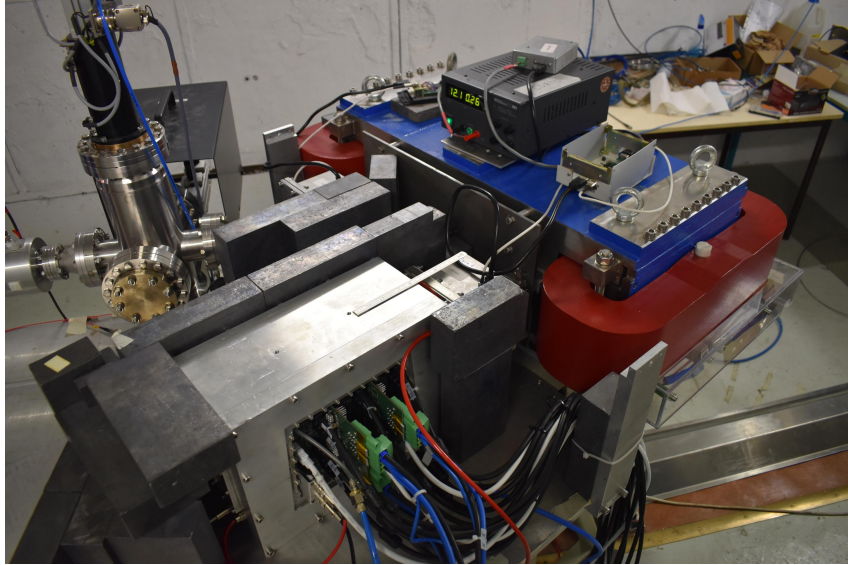


Figure 6.2: *The gas box containing the 96-chips InGrid module installed at the LEETECH detector area.*

design, where dead region area can be large due to the octoboard placement and Timepix chip connections. An extensive overview of the global and local track reconstruction method modifications can be found in [136].

The Hough transform modification was used for the data analysis from the InGrid module. Its performance for similar applications was demonstrated in [73, 76]. The software tool was developed with Python using the OpenCV image processing library and Matplotlib + Qt interface [137] (Figure 6.4).

6.2.1 Hough transform

The Hough transform is a common technique to search for linear and circular patterns in the image [138], which can be extended for an arbitrary shape [139]. It is a global method, which uses the hits from the entire detector, thus being less sensitive to dead regions. The mathematical formulation of the Hough line transform is the following: each line can be represented by the equation 6.1

$$\rho = x \cos \theta + y \sin \theta \quad (6.1)$$

where ρ is the perpendicular distance from the origin to the line, and θ is the angle formed by this perpendicular line and horizontal axis measured in counter-clockwise direction

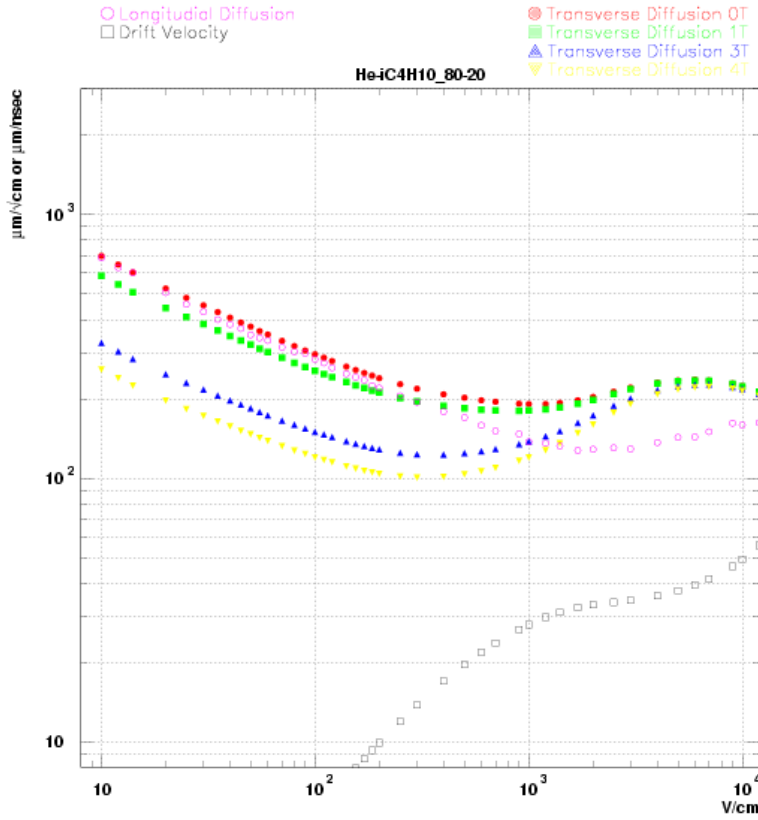


Figure 6.3: Drift velocity and diffusion coefficients as a function of the drift electric field for He/isoButane 80/20 gas mixture [132] generated by Magboltz [38].

(Figure 6.5(a)).

When processing the 2D hits frame from the InGrid detector, each hit with defined x and y (Equation 6.1) represents a sinusoid in a Hough space. The intersection point of many sinusoids indicates a track. In practice this is implemented by filling the 2D histogram in a Hough space and searching for the local maxima. Example of the Hough transform application on the data frame from two octoboards of the 96-chips InGrid module is shown in Figure 6.6.

6.2.2 Reconstruction results

Several reconstructed data frames are presented in Figure 6.7. From there it can be seen that even for the track multiplicities around 10 and despite multiple scattering effect secondary electrons production and tracks overlapping the majority of tracks are

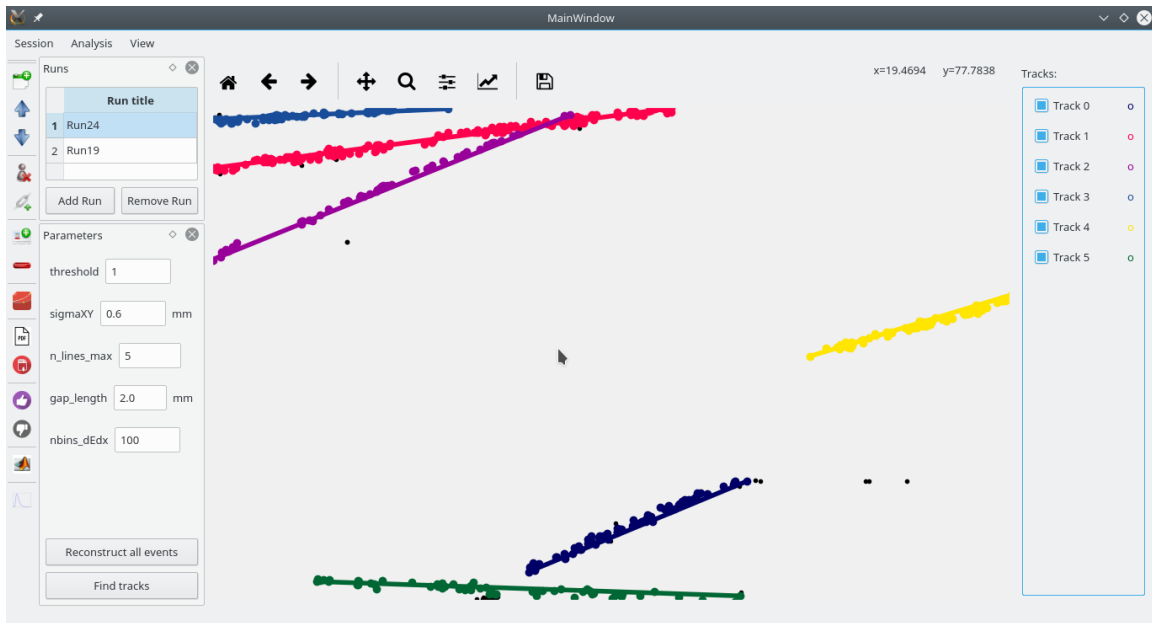


Figure 6.4: A software tool, developed for the track reconstruction and further data analysis, based on the *OpenCV*, *Qt*, *ROOT* and *Matplotlib* libraries. Results of the data frame track reconstruction is shown.

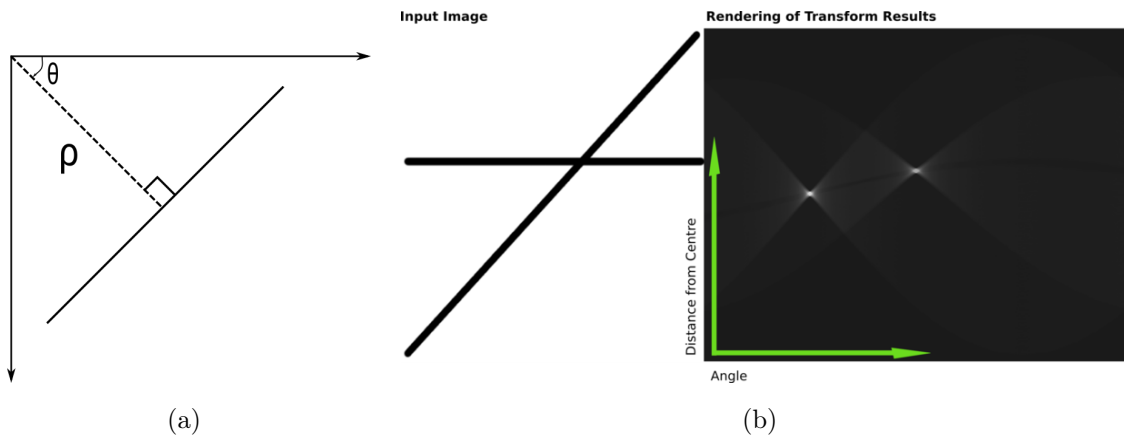


Figure 6.5: Hough transform illustration. The line parametrization (a) and result of the Hough transform on the image with two lines (b).

reconstructed correctly.

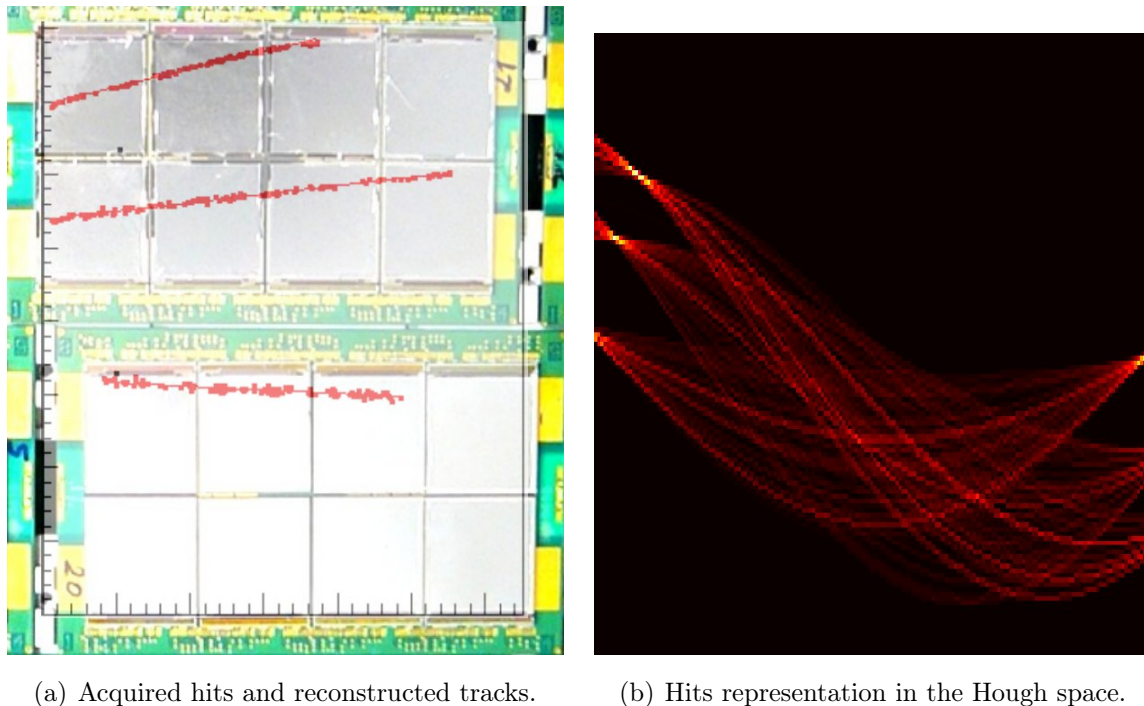


Figure 6.6: *Hough transform of the InGrid data frame.*

6.2.3 Tracks selection criteria

From Figure 6.7 one can see that a number of tracks does not correspond to the beam electrons and should not be propagated to further analysis. Therefore, a set of selection criteria should be applied to suppress the background.

In order to develop a first approach for track selection, for a single run of 1000 frames the analysis was performed and good tracks were selected manually. The track parameter histograms for good and bad tracks for each parameter were compared (Figure 6.8) and corresponding selection criteria were deduced.

The good tracks have a small θ angle - deviation from the horizontal direction (Figure 6.8(b)) and the distance to origin ρ which corresponds to the central octoboard placement (Figure 6.8(c)). The x_0 entry coordinate of the good tracks (Figure 6.8(a)) also corresponds to the octoboard position which are shifted by about 7 mm. This is represented by two peaks at $x_0 = 3 \text{ mm}$ and $x_0 = 10 \text{ mm}$ in Figure 6.8(a). The fit of reconstructed tracks can be used to extract another selection criteria of hits density per track length (Figure 6.8(d)).

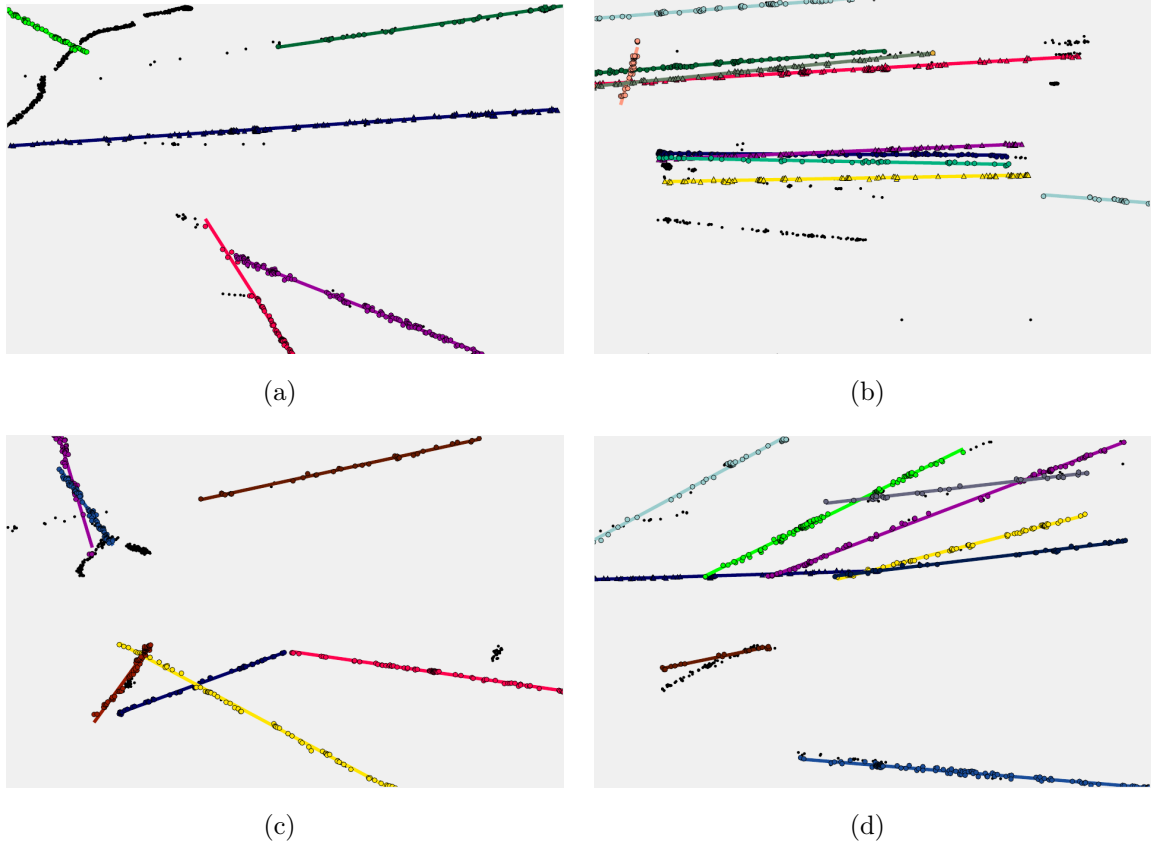


Figure 6.7: *Examples of reconstructed events.*

6.3 Spatial resolution

The common way to determine a transverse spatial resolution of gaseous detector is to compare the track residual distributions to the expected ones caused by diffusion only. The detector intrinsic transverse spatial resolution σ_0 is defined with a relation:

$$\sigma_{xy}(z) = \sqrt{\sigma_0^2 + D_T^2 \cdot z}, \quad (6.2)$$

where z is a drift distance to the cathode plane, D_T is a transverse gas diffusion coefficient and $\sigma_{xy}(z)$ is a total spatial resolution of the detector, which is a function of z .

Therefore, typical plots characterizing the detector are obtained performing the so-called z -scan, when the drift distance is varied and residual mean is plotted versus the z -position of the beam (height above the anode plane) as shown in Figure 6.9.

Based on the results presented in Figure 6.9, the authors of Ref. [76] stated that the shape of the fitted curve in comparison to the single electron diffusion hints on the reso-

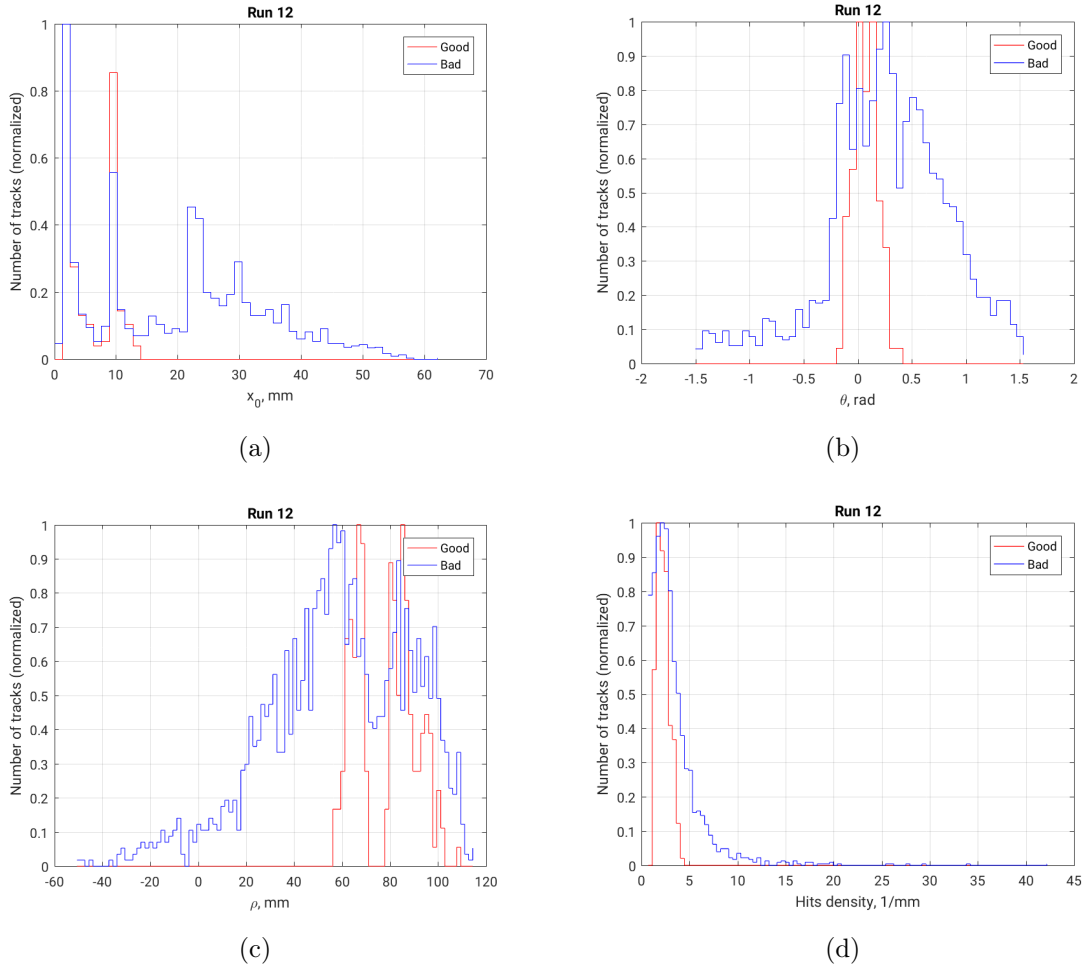


Figure 6.8: Tracks selection criteria, derived from manual track annotation.

lution of the detector: all points are slightly above the optimum value given by diffusion. Hence, the resolution is completely dominated by diffusion, which is physically possible for a pixelated readout, as the intrinsic spatial resolution is small, $55 \mu\text{m}/\sqrt{12} = 15.9 \mu\text{m}$.

For the detector setup at LAL (Figure 6.2) it is not possible to adjust the z coordinate of the beam, since a small gas volume with a 17 mm drift distance was used. For the reconstructed tracks the residuals were calculated and fitted by the Gaussian curve (Figure 6.10).

From Figure 6.3 one can see that at the conditions of the experiment (drift field is equal to 1200 V/cm), the gas transverse diffusion coefficient is about $200 \mu\text{m}/\sqrt{\text{cm}}$. The maximum drift distance was limited by the height of the field mesh above the cathode plane, which is about 17 mm. However, the precise value is not well defined because of the

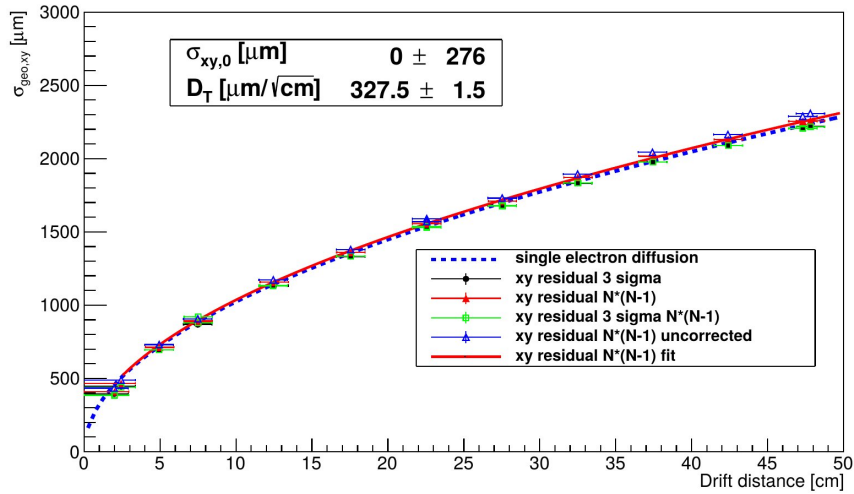


Figure 6.9: The residuals z -scan performed for the large-TPC prototype with Micromegas/In-Grid layout in Ar/isoButane/CF₄ 95/3/2 gas mixture against single electron diffusion. The residual means were calculated using different methods [76].

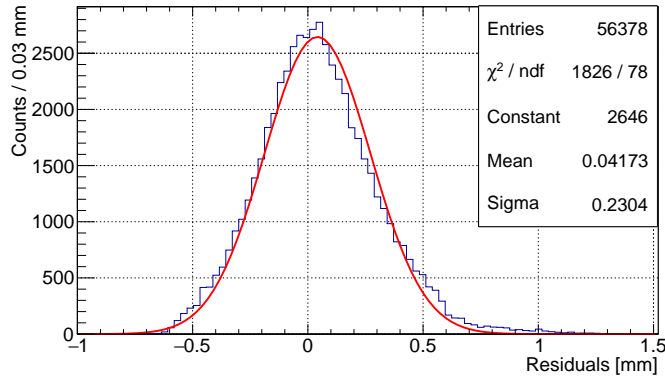


Figure 6.10: The residuals distribution obtained from the measurements. The obtained value of $\sigma_{xy} = 230 \mu\text{m}$ agrees with the expected spatial spread.

relatively large beam size of a few mm and nonzero track inclination angle (Figure 6.7). For the obtained value of $\sigma_{xy} = 230 \mu\text{m}$ (Figure 6.10) the drift distance calculated according to equation 6.2 is found to be 13 mm, which is a reasonable evaluation. Therefore, the shape and width of the reconstructed track residuals distribution are in agreement with the expectations.

6.4 dN/dx distributions

After the reconstruction and filtering stage the number of track hits per unit length was obtained. Neglecting the pixel double-hit events, this is equal to the number of ionization electrons.

To the tracks were divided on slices of 4 mm length and the number of hits per mm was calculated for several runs (Figure 6.11).

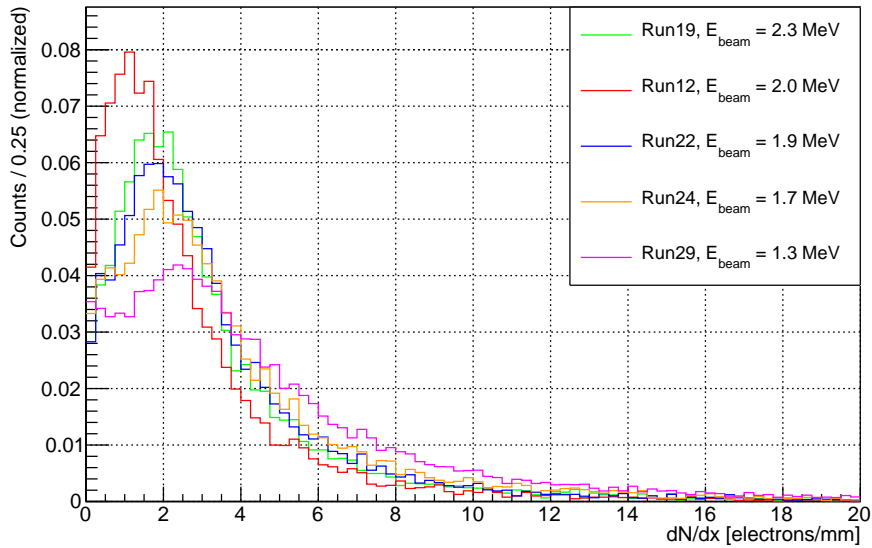


Figure 6.11: *Experimental results of dN/dx distributions for different beam electron energies.*

The Landau fit of the distribution is shown in Figure 6.12. Similarly to the simulation results (Section 5.3), for the thin gas layers the Landau curve gives an approximate description of the dE/dx distribution.

The comparison results of experimental and Degrad simulation data is shown in Figure 6.13. It can be observed that the simulation does not describe well the experimental distributions, which have larger RMS. Possible explanation of the deviation to the larger values is the hits from crossing tracks either from delta-electrons or from scattered electron, which hits can be partially assigned to another track. It can be seen from Figure 6.7 that the described case is present at each data frame. Deviations to the lower values can be caused by the detector field inhomogeneities, which deviate the ionization electrons thus reducing the chip occupancy.

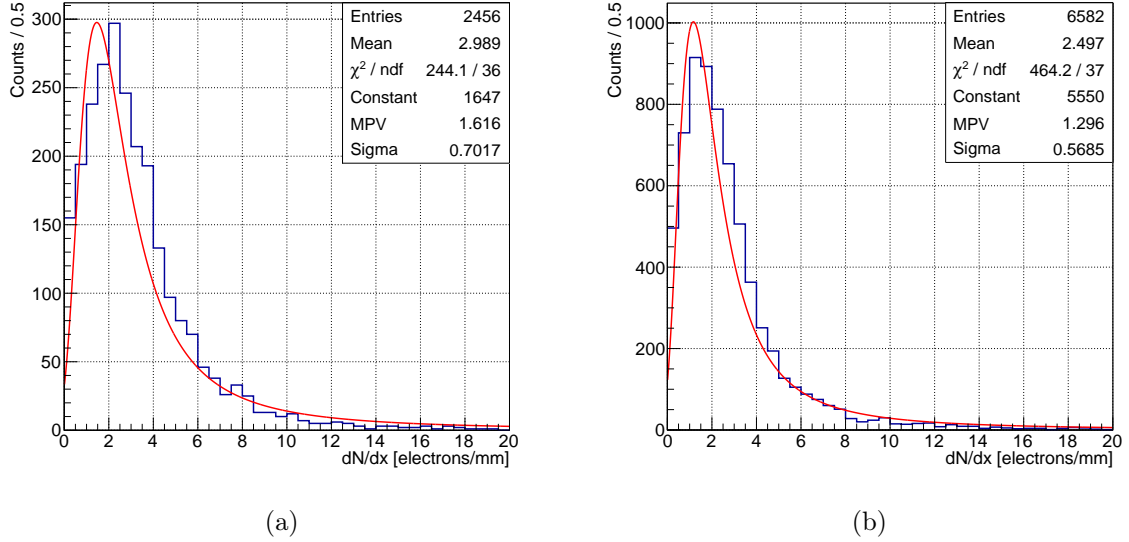


Figure 6.12: Number of ionization electrons per track unit length for primary electrons of 1.7 MeV (a) and 2.3 MeV (b) kinetic energy, fitted with Landau curve.

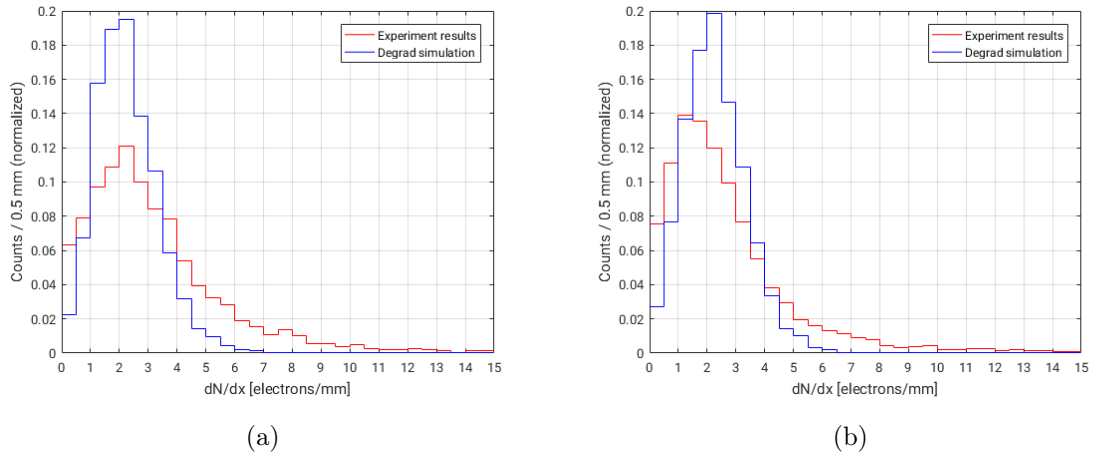


Figure 6.13: Comparison between the dN/dx distributions obtained in Degrad simulation and experiment for the runs shown in Figure 6.12.

6.5 Discussion

The Micromegas/InGrid module test beam results has demonstrated that the low energy electrons can be successfully used for the gaseous detectors characterization. The corresponding track reconstruction software has been developed, yielding reasonable results

CHAPTER 6. LARGE-AREA INGRID MODULE CHARACTERIZATION

for the detector spatial resolution. The dE/dx distributions of low energy electrons were obtained and compared to corresponding simulation. Further research of the deviations from the expected distribution shape can improve the agreement with simulation.

QUARTZ DETECTOR PROTOTYPE CHARACTERIZATION

As mentioned in Chapter 4, a short (below 10 ps) length of the bunches from PHIL ensures a good particles timing at the exit of LEETECH. This enables a possibility to characterize the detectors with precise timing requirements.

Within the present thesis the timing of the quartz bar detector was studied at the LEETECH. This is important in view of the upgrade of the BESIII detector coupled to multi-channel plate photomultiplier (MCPMT) and planning of future HIEPA tau-charm factory in China [21]

This chapter describes the timing simulation of the LEETECH spectrometer, indicating the feasible values of the electrons time spread at the exit. The experimental study of the quartz bar time spread is addressed and obtained values are compared to the simulation results in view of the time-of-flight detector precision requirements for the BESIII upgrade and HIEPA.

7.1 Introduction

As outlined in Chapter 2, one of the possible choices of the time-of-flight detector for the upgrade of the BESIII experiment in China is a quartz detector readout by MCP-PMT. In this chapter preliminary tests of the 20x40x200 mm³ quartz bar coupled to MCP-PMT with the LEETECH facility are discussed. The main question addressed is how precisely can we measure the time difference of the signal arrival to the opposite sides of the quartz bar using the Cherenkov light, produced by the relativistic particles passing through the detector.

Working with the electron beam from PHIL, which has a small time spread of about 5 ps, the LEETECH facility can be used for characterization of such types of detectors.

7.2 Physics basics

The quartz bar coupled to a photon detector can detect a Cherenkov light, emitted by a charged particle traversing the quartz media. This is used for a particle identification technique, based on a time-of-flight measurement. A brief overview of this principle is outlined below.

The Cherenkov electromagnetic radiation is emitted when the charged particle passes through a medium. The speed of light is c/n , where n is a medium refractive index. The Cherenkov light is emitted when c/n is lower than the particle's velocity v . In this case the polarisation of the medium molecules occurs and they emit a few eV photons in the direction, defined in the following way (Figure 7.1):

$$\cos(\theta_C) = \frac{c}{nv} = \frac{1}{n\beta} \quad (7.1)$$

This is illustrated by Figure 7.1(a). The spectrum of Cherenkov photons per unit length is described by the following equation:

$$\frac{dN}{\partial x \partial \lambda} = \frac{2\pi\alpha z^2}{\lambda^2} \left(1 - \frac{1}{n^2(\lambda)\beta^2} \right) \quad (7.2)$$

and is shown in Figure 7.1(b). In a medium with high enough refractive index and high quality of the surface the Cherenkov radiation will exert a multiple inner reflections until it reaches the end face of the detector, preserving the speed and angular distribution.

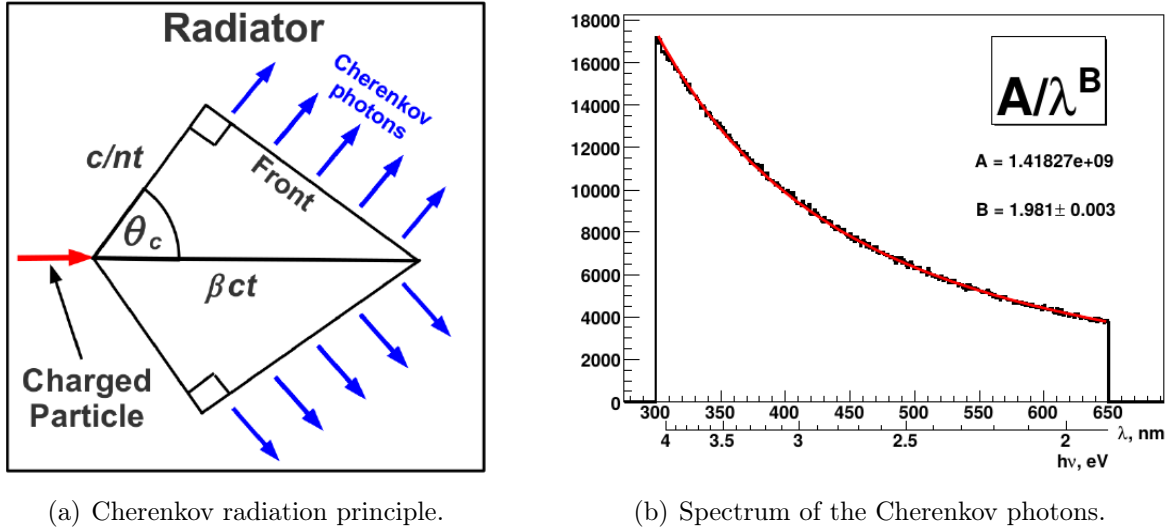


Figure 7.1: Cherenkov effect description [140].

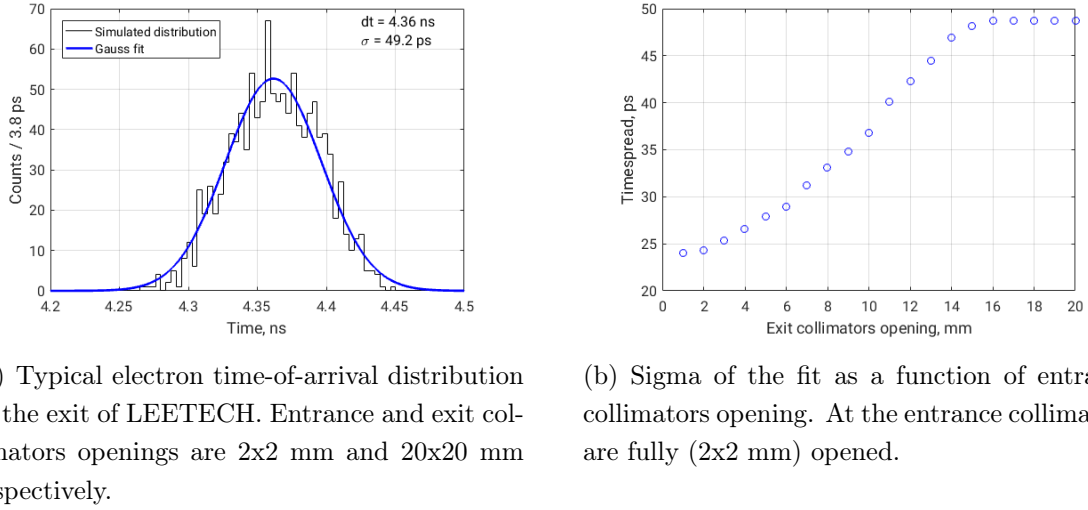
7.3 Simulation

To better understand the expected spread in particle arrival time at the exit of the LEETECH spectrometer the corresponding simulation was performed using Geant4. In Figure 7.2(a) the electron time of arrival distribution at the exit of LEETECH is shown, which is well described by the Gaussian curve. The parameter impacting the time spread the most is the exit collimator opening, since it directly defines possible deviations from the optimal electron trajectory. The Gaussian sigma from the fit of the time of arrival distribution as a function of the entrance collimators opening is presented in Figure 7.2(b).

The obtained estimated time spread in the range between 25 and 50 ps demonstrates the feasibility of the LEETECH spectrometer to deliver precision timing measurements.

7.4 Experimental setup

The highly polished $20 \times 40 \times 200 \text{ mm}^3$ quartz bar was placed on the bearings, while two MCP-PMT detectors (Burle XP85012 and Hamamatsu SL-10) were positioned at its end faces without any additional optical link. To reduce the external light contribution the setup is placed in the steel box with the black inner side (Figure 7.3). To allow the electron beam passing to the quartz detector, a long aperture of 1 cm height was made at the side of the cover box from the detector center to its end (10 cm). The light tightness was reinforced using the black tape covering.



(a) Typical electron time-of-arrival distribution at the exit of LEETECH. Entrance and exit collimators openings are 2x2 mm and 20x20 mm respectively.

(b) Sigma of the fit as a function of entrance collimators opening. At the entrance collimators are fully (2x2 mm) opened.

Figure 7.2: Simulation results of the LEETECH timing characteristics.

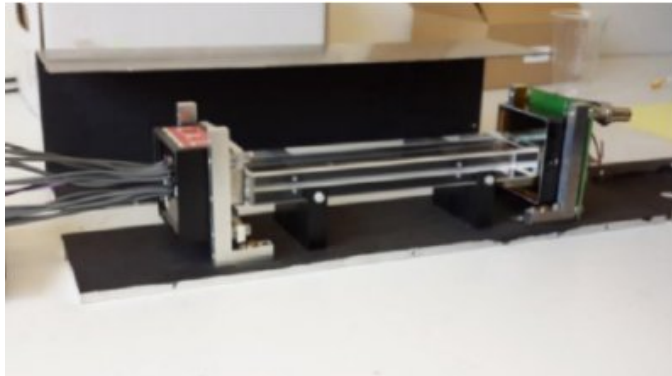


Figure 7.3: Components of the quartz detector experimental setup. The quartz bar of $20 \times 40 \times 200 \text{ mm}^3$ size, two MCP-PMT and the cover plate are shown.

The LeCroy WavePro 740Zi-A oscilloscope with a 40 GHz bandwidth was used for signal readout from MCP-PMT. Typical waveforms are shown in Figure 7.4, where the histogram of MCP-PMT time-of-arrival differences is also displayed. A clear peaks corresponding to the Cherenkov light from quartz bar end-sides are observed along with the noise and periodic coupling signal.

To study the time resolution of the detector and provide sufficient signal-to-noise ratio the LEETECH intensity was maximized by full opening the collimators at the entrance and exit and setting the magnetic field to the maximum value of the attenuator spectral characteristic (Figure 4.24). Using a $100 \mu\text{m}$ attenuator this corresponds to the kinetic

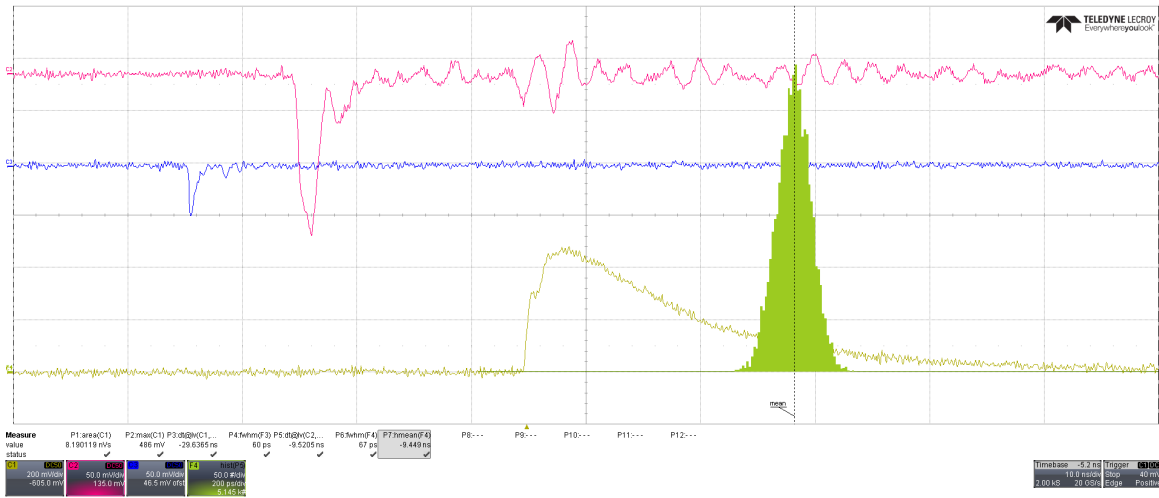


Figure 7.4: Typical waveform shapes acquired during the quartz bar measurement session. Red and blue signals correspond to MCP-PMTs, Burle XP85012 and Hamamatsu SL-10, respectively, yellow signal represents the PHIL laser used as a trigger, and the histogram of time differences between the signal time of arrival are shown.

energy of the electrons at the exit of about 2.95 MeV.

The quartz bar, surrounded by MCP-PMT and light-protected from external noise was installed in front of the LEETECH exit window; the center of the detector was aligned with a beam entry point. Having a long hole in the quartz protection box matching the beam entrance, the quartz bar position was sequentially changed with a step of 2 cm. This way changing the beam entrance point and therefore mean value of the time-of-arrival difference. Six different detector positions were measured in total with the beam entrance point displacement from the center of 0, 2, 4, 6, 8 and 10 cm.

The time difference distribution between time-of-arrival of two signals from the quartz bar end-sides was studied. Typical measurement result is shown in Figure 7.5.

The value of time-of-arrival difference for a single acquisition was calculated using the digital Constant Fraction Discriminator (dCFD) method [112, 141–143], when the time of signal arrival is defined as a time stamp and when the signal reaches a half of its amplitude. The time stamp itself is calculated as a linear interpolation result between the two nearest points on the signal waveform.

The time spread result of about 50 ps was obtained. This value looks promising for the further studies and demonstrates the quartz bar and MCP-PMT detector applicability for the fast time-of-flight detector systems.

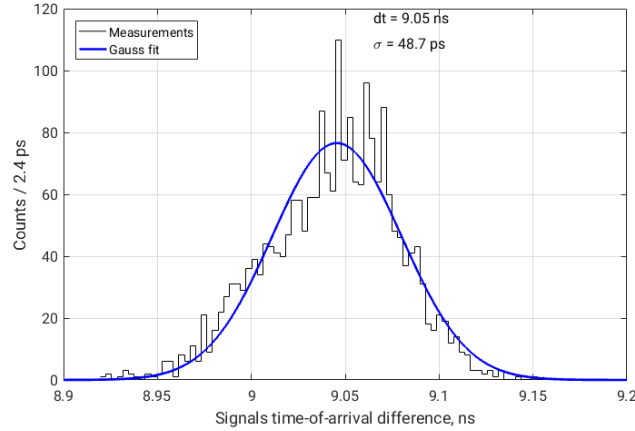


Figure 7.5: Typical measured time-of-arrival difference distribution for the quartz bar detector setup. The high mean value is caused by the cable length difference, while the measured time spread includes the total contribution from LEETECH, quartz bar, MCPMT and readout electronics.

7.5 Position recovery

The measurement result for different detector positions is shown in Figure 7.6. A linear dependence between the quartz bar displacement and mean time-of-arrival difference is observed for the medium displacement value. At the same time, in the case when the beam enters the detector near its edge the saturation is observed. The mean time at zero displacement represents the delay difference caused by different cable length for the two MCPMT detectors. The slope of the linear fit has a meaning of the light velocity projection to the quartz bar longitudinal axis.

A simplified velocity calculation from the Cherenkov light angle definition (Figure 7.1(a)) for the quartz bar with refractive index of $n = 1.46$ yields:

$$V_x = \frac{c}{n} \sin(\theta_C) = \frac{c}{n} \sqrt{1 - \left(\frac{1}{n\beta}\right)^2} = 14.8 \text{ cm/ns} \quad (7.3)$$

The slope value from the fit is $p_1 = 0.12 \pm 0.03 \text{ ns/cm}$, which gives the light velocity projection value of $V_x = 2/p_1 = 16 \pm 4 \text{ cm/ns}$, which agrees with the calculation within uncertainty. The fit error can be significantly improved by repeating the measurement with a finer step and better detector positioning precision.

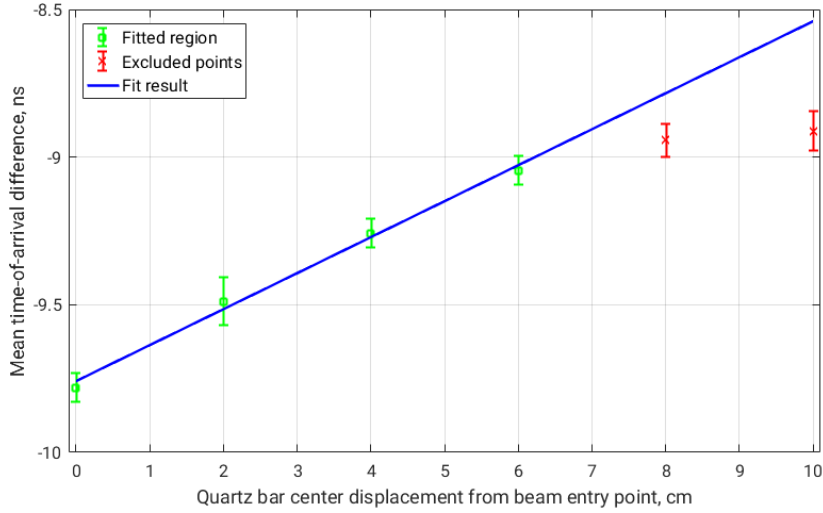


Figure 7.6: Mean time-of-arrival difference as a function of the quartz bar displacement. At large displacements the beam entrance point is very close to the detector end and the saturation is observed.

7.6 Discussion

The resulting timespread of 50 ps for the time-of-arrival difference obtained with the $20 \times 40 \times 200 \text{ mm}^3$ quartz bar coupled to MCP-PMT detector setup demonstrates its competitiveness as a candidate for the future tau-charm factories time-of-flight detector, where the detector resolution of tens of picoseconds is required. The obtained value accounts for several contributions. It includes several sources of the time spread: timing of the LEETECH facility, variation of trajectories in the quartz bar, the MCP-PMT timing comprises and the readout electronics jitters. In the current detector setup the time resolution of the MCP-PMT detector plays a crucial role. Among the alternatives a promising choice is a Silicon Photomultipliers (SiPM) which have the time resolution down to values about 20 ps [144, 145]. The further characterization of the quartz bar and MCP-PMT time resolution and investigation of such characteristics as detector geometry, beam intensity, quality of the optical coupling between the quartz and MCP-PMT surfaces is required.

CHAPTER 7. QUARTZ DETECTOR PROTOTYPE CHARACTERIZATION

MAIN RESULTS

The main results obtained in the present thesis are listed below

- A new test beam facility LEETECH (Low Energy Electron TECHnique) was designed, constructed and commissioned at LAL (Orsay), providing a possibility of smooth energy and intensity adjustment of the electron beam from PHIL accelerator.
- A facility characterization including energy and time spread, beam parameters dependence on the LEETECH configuration options were established.
- A low intensity mode with a few (down to a single) electrons per bunch was studied with a diamond sensor, also establishing the detector capability to resolve the signals from individual MIPs.
- In framework of cooperation with ILC-TPC collaboration the measurement campaign of the large-area Micromegas/InGrid detector was performed and the dE/dx value for low-energy electrons was studied. Performance of the actual tools to perform the dE/dx simulation are compared.
- Measurement campaign of the quartz bar detector readout by the MCP-PMT, which is a candidate for the time-of-flight for BESIII upgrade and future τ -charm factories, was performed. The obtained time spread of about 50 ps is a promising result for further detector development. This also demonstrated capabilities of the LEETECH platform for precision timing measurements.

DISCUSSION AND OUTLOOK

Within the present thesis the design, construction and commissioning of a new test beam facility LEETECH have been performed. Performance of the new facility, including low-multiplicity operation mode has been demonstrated. A number of interesting detector tests, including large-area diamond, Micromegas/InGrid and quartz bar detectors have been performed.

The construction of LEETECH (Low Energy Electron TECHnique) and its application to several types of detector is presented.

Based on the PHIL accelerator with a beam energy in the range between 3.5 and 5 MeV, upgradable to 10 MeV, LEETECH finds its place for the detector characterizations and tests where a high energy of modern large test beam facilities is not required, but a smooth adjustment of beam energy and intensity is a key requirement. This covers a wide range of applications including many test of gaseous and semiconductor detectors, in particular those where MIPs are desired, medical physics application and others.

A full cycle of design, construction and commissioning has been performed, including a technical implementation. A simulation framework has been developed in Geant4 framework, providing information on the bunches characteristics at the exit of LEETECH depending on the facility configuration parameters in a convenient format.

Following the facility characterization, several measurement campaigns for different detector technologies were performed at the LEETECH facility. The diamond sensor measurements demonstrated the functionality of LEETECH to provide bunches consisting of a few electrons and proved the diamond sensor ability to resolve signals from such bunches.

A characterization of the first large-area Micromegas/InGrid detector using the low-energy electrons has been performed and several characteristics such as spatial and dE/dx resolution were measured. The track reconstruction technique have been optimized for the case of medium track multiplicity and multiple scattering and can potentially be reused for similar problems.

Finally, timing characterization of the quartz bar coupled to MCPMT was performed. A time resolution of 50 ps was obtained. This is a first demonstration for a development of the forward time-of-flight detector for a future tau-charm factory.

Despite all the difficulties, quite a nice extension of the PHIL accelerator has been installed, providing a smooth adjustment of energy and intensity of the outgoing electron bunches. Taking into account an inherited from PHIL ultimately short bunch duration (down to 20 ps) and relatively small operation cost (due to low particles energy) the resulting spectrometer represents a competitive test beam facility among existing ones, which are of high demand nowadays. Several measurement sessions have demonstrated its applicability to the real world problems.

The scope of improvements is very broad. A common issue in all the performed measurement session is a background particles which can be seen in spectrums acquired with diamond detector and in the electron track frames from Micromegas/InGrid module. This background is synchronous with a beam and most probably caused by multiply-scattered particles. However, all the efforts to suppress it have not yield a significant improvement.

The LEETECH simulation performance can be improved by porting it to the distributed computing systems such a cluster. The commonly used GPU can be an option to accelerate the simulation if this will be officially supported by Geant4 in the future.

Acknowledgements

The work described in this thesis was made possible due to the efforts of many people. First of all I would like to acknowledge my family who patiently allowed me to travel for quite a long time to France, spend the evenings in data analysis and writing the thesis.

I would like to thank to my supervisors Sergey Barsuk and Oleg Bezshyyko, who have found the LEETECH project, all the time wisely guiding the workflow. Also I'm grateful to Maxim Titov for giving me a chance to attend and present my work at conferences and introducing me to RD51 community, which made possible the measurement session with a Micromegas/InGrid module. I would like to thank also to Igor Kadenko for all the support from Ukrainian side.

At LAL I worked with a person who has made a major impact on my working approach, being a great example of leading skills and optimism, this is Slava Kubytskyi. The diamond detector measurement session was a first success of the LEETECH facility, at the same time being fun and full of adventures, as well as the followed analysis was. Thank you!

There is also a great man who helped us to rise the LEETECH when we had nothing, Leonid Burmistrov. Always being hard-loaded with his own tasks, he provided us all the equipment needed to install, test and commission the LEETECH, from the screwdriver to the 40 GHz oscilloscope, also leading the measurement sessions and caring for a good work organization. Also I'm very grateful to Iryna Chaikovska for all the support with hardware and software and fruitful discussions about the LEETECH activities.

Withing the RD51 collaboration I was lucky to work with two great persons: Jochen Kaminsky, who arrived at LAL with the Micromegas/InGrid module, providing everything for the measurements and carefully guiding the flow; and Dorothea Pfeiffer, who helped me with the simulation research on the electron energy losses in gas. Thank you Jochen and Doro!

A special thanks to whole department of accelerator at LAL, who provided the beam from the PHIL accelerator and made possible all our measurements. Pierre, Jean-Noel, Sophie, Christelle, Thomas, Nouredine, Nicolas - sincerely thank you!

The current thesis activity was possible thanks to the scholarship of the French Embassy in Ukraine. I'm very grateful to the organization and coordination for the great support during the Ph.D. project.

BIBLIOGRAPHY

- [1] Georges Aad et al. “Observation of a new particle in the search for the Standard Model Higgs boson with the ATLAS detector at the LHC”. In: *Physics Letters B* 716.1 (2012), pp. 1–29 (cit. on p. 17).
- [2] Julia Woithe, Gerfried J Wiener, and Frederik F Van der Veken. “Let’s have a coffee with the Standard Model of particle physics!” In: *Physics Education* 52.3 (2017), p. 034001 (cit. on p. 18).
- [3] W. Buchmuller and C. Ludeling. “Field Theory and Standard Model”. In: *High-energy physics. Proceedings, European School, Kitzbuehel, Austria, August 21-September, 2005*. 2006. arXiv: [hep-ph/0609174 \[hep-ph\]](#) (cit. on p. 18).
- [4] Janusz Gluza and Tord Riemann. “Massive Feynman integrals and electroweak corrections”. In: *Nucl. Part. Phys. Proc.* 261-262 (2015), pp. 140–154. DOI: [10.1016/j.nuclphysbps.2015.03.012](#). arXiv: [1412.3311 \[hep-ph\]](#) (cit. on p. 18).
- [5] Paul Langacker. *The standard model and beyond*. CRC press, 2017 (cit. on p. 19).
- [6] “The High-Luminosity LHC”. In: (2015) (cit. on p. 19).
- [7] Harriet Kim Jarlett. “The Future Circular Collider”. In: (2016) (cit. on p. 19).
- [8] Qing Qin et al. “Overview of the CEPC Accelerator”. In: (2015) (cit. on p. 19).
- [9] T Abe et al. “Belle II technical design report”. In: *arXiv preprint arXiv:1011.0352* (2010) (cit. on p. 19).
- [10] Matthew Reece. “Physics at a Higgs factory”. In: *The Future of High Energy Physics: Some Aspects*. World Scientific, 2017, pp. 39–53 (cit. on p. 21).
- [11] Keisuke Fujii et al. “Physics case for the international linear collider”. In: *arXiv preprint arXiv:1506.05992* (2015) (cit. on pp. 21–23).
- [12] Daniel G Figueroa, Juan García-Bellido, and Francisco Torrentí. “Decay of the standard model Higgs field after inflation”. In: *Physical Review D* 92.8 (2015), p. 083511 (cit. on p. 22).

- [13] Georges Aad et al. “Search for dark matter produced in association with a Higgs boson decaying to two bottom quarks in p p collisions at $s = 8$ TeV with the ATLAS detector”. In: *Physical Review D* 93.7 (2016), p. 072007 (cit. on p. 22).
- [14] Alexander Kusenko, Lauren Pearce, and Louis Yang. “Postinflationary Higgs relaxation and the origin of matter-antimatter asymmetry”. In: *Physical review letters* 114.6 (2015), p. 061302 (cit. on p. 22).
- [15] Howard Baer et al. “The International linear collider technical design report-volume 2: physics”. In: *arXiv preprint arXiv:1306.6352* (2013) (cit. on p. 22).
- [16] Barry Barish and James E. Brau. “The International Linear Collider”. In: *Int. J. Mod. Phys. A* 28.27 (2013), p. 1330039. DOI: [10.1142/S0217751X13300391](https://doi.org/10.1142/S0217751X13300391). arXiv: [1311.3397](https://arxiv.org/abs/1311.3397) [physics.acc-ph] (cit. on p. 24).
- [17] Ties Behnke et al. *The international linear collider technical design report-volume 4: detectors*. Tech. rep. Argonne National Laboratory (ANL), Argonne, IL (United States); Pacific Northwest National Laboratory (PNNL), Richland, WA (United States); SLAC National Accelerator Laboratory (SLAC), Menlo Park, CA (United States); Fermi National Accelerator Laboratory (FNAL), Batavia, IL (United States), 2013 (cit. on pp. 25, 52).
- [18] He Sheng Chen. “Tau-Charm Factory Project at Beijing”. In: *Nuclear Physics B-Proceedings Supplements* 59.1-3 (1997), pp. 316–323 (cit. on p. 26).
- [19] Svende Annelies Braun. “Analysis of the decay $\Theta^+ \Theta^- \rightarrow \gamma X(3872) \rightarrow J/\psi \gamma \gamma$ at the BESIII experiment”. In: (2014) (cit. on p. 27).
- [20] Medina Ablikim et al. “Design and construction of the BESIII detector”. In: *Nuclear Instruments and Methods in Physics Research Section A: Accelerators, Spectrometers, Detectors and Associated Equipment* 614.3 (2010), pp. 345–399 (cit. on pp. 27, 28).
- [21] Frederick A Harris, BES Collaboration, et al. “Becpii and Besiii”. In: *Nuclear Physics B-Proceedings Supplements* 162 (2006), pp. 345–350 (cit. on pp. 28, 131).
- [22] Zhao Chuan et al. “Time calibration for the end cap TOF system of BESIII”. In: *Chinese Physics C* 35.1 (2011), p. 72 (cit. on p. 29).
- [23] RX Yang et al. “MRPC detector for the BESIII E-TOF upgrade”. In: *Journal of Instrumentation* 9.09 (2014), p. C09032 (cit. on p. 29).

BIBLIOGRAPHY

- [24] AE Bondar. “Project of a super charm-tau factory at the Budker Institute of Nuclear Physics in Novosibirsk”. In: *Physics of Atomic Nuclei* 76.9 (2013), pp. 1072–1085 (cit. on p. 30).
- [25] Changzheng Yuan. “Hadron spectroscopy and charmonium decays from BES and CLEOc”. In: *High Energy Physics and Nuclear Physics* 30.6 (2006), pp. 488–496 (cit. on p. 30).
- [26] Besiii Collaboration et al. “The construction of the BESIII experiment”. In: *Nuclear Instruments and Methods in Physics Research Section A: Accelerators, Spectrometers, Detectors and Associated Equipment* 598.1 (2009), pp. 7–11 (cit. on p. 30).
- [27] D. Attie. “TPC review”. In: *Nucl. Instrum. Meth.* A598 (2009), pp. 89–93. DOI: [10.1016/j.nima.2008.08.114](https://doi.org/10.1016/j.nima.2008.08.114) (cit. on pp. 34, 35).
- [28] Christoph Brezina et al. “Gossipo-3: A prototype of a Front-End Pixel Chip for Read-Out of Micro-Pattern Gas Detectors”. In: (2009) (cit. on pp. 36, 40).
- [29] F. Sauli. “Bubble Chambers”. In: *Annu. Rev. Nucl. Sci (TODO edit)*. (1977) (cit. on pp. 36, 97).
- [30] Vittorio Palladino and Bernard Sadoulet. “Application of classical theory of electrons in gases to drift proportional chambers”. In: *Nuclear Instruments and Methods* 128.2 (1975), pp. 323–335 (cit. on pp. 36, 37).
- [31] V. Palladino and B. Sadoulet. “Application of the Classical Theory of Electrons in Gases to Multiwire Proportional and Drift Chambers”. In: (1974) (cit. on pp. 37, 38).
- [32] Philip M Morse, WP Allis, and ES Lamar. “Velocity distributions for elastically colliding electrons”. In: *Physical Review* 48.5 (1935), p. 412 (cit. on p. 37).
- [33] To Holstein. “Energy distribution of electrons in high frequency gas discharges”. In: *Physical Review* 70.5-6 (1946), p. 367 (cit. on p. 37).
- [34] Henry Margenau. “Conduction and dispersion of ionized gases at high frequencies”. In: *Physical Review* 69.9-10 (1946), p. 508 (cit. on p. 37).
- [35] LS Frost and AV Phelps. “Rotational excitation and momentum transfer cross sections for electrons in H2 and N2 from transport coefficients”. In: *Physical Review* 127.5 (1962), p. 1621 (cit. on pp. 37, 38).

- [36] AG Engelhardt and AV Phelps. “Transport coefficients and cross sections in argon and hydrogen-argon mixtures”. In: *Physical Review* 133.2A (1964), A375 (cit. on p. 38).
- [37] RD Hake Jr and AV Phelps. “Momentum-Transfer and Inelastic-Collision Cross Sections for Electrons in O₂, CO, and C O₂”. In: *Physical Review* 158.1 (1967), p. 70 (cit. on p. 38).
- [38] SF Biagi. “Monte Carlo simulation of electron drift and diffusion in counting gases under the influence of electric and magnetic fields”. In: *Nuclear Instruments and Methods in Physics Research Section A: Accelerators, Spectrometers, Detectors and Associated Equipment* 421.1 (1999), pp. 234–240 (cit. on pp. 38, 39, 121).
- [39] C. Patrignani et al. “Review of Particle Physics”. In: *Chin. Phys.* C40.10 (2016), p. 100001. DOI: [10.1088/1674-1137/40/10/100001](https://doi.org/10.1088/1674-1137/40/10/100001) (cit. on pp. 38, 96).
- [40] ME Rose and SA Korff. “An investigation of the properties of proportional counters. I”. In: *Physical Review* 59.11 (1941), p. 850 (cit. on p. 38).
- [41] Walter Blum, Werner Riegler, and Luigi Rolandi. *Particle detection with drift chambers*. Springer Science & Business Media, 2008 (cit. on pp. 39, 108).
- [42] P Fonte et al. “Single-electron pulse-height spectra in thin-gap parallel-plate chambers”. In: *Nuclear Instruments and Methods in Physics Research Section A: Accelerators, Spectrometers, Detectors and Associated Equipment* 433.1 (1999), pp. 513–517 (cit. on p. 40).
- [43] Y. Bilevych et al. “Spark protection layers for CMOS pixel anode chips in MPGDs”. In: *Nucl. Instrum. Meth.* A629 (2011), pp. 66–73. DOI: [10.1016/j.nima.2010.11.116](https://doi.org/10.1016/j.nima.2010.11.116) (cit. on pp. 39, 52).
- [44] Heinz Raether. “Electron avalanches and breakdown in gases”. In: (1964) (cit. on p. 40).
- [45] E. Rutherford and H. Geiger. “An Electrical Method of Counting the Number of α -Particles from Radio-Active Substances”. In: *Proceedings of the Royal Society of London Series A* 81 (Aug. 1908), pp. 141–161. DOI: [10.1098/rspa.1908.0065](https://doi.org/10.1098/rspa.1908.0065) (cit. on p. 40).
- [46] H. Geiger and W. Müller. “Elektronenzählrohr zur Messung schwächster Aktivitäten”. In: *Naturwissenschaften* 16 (Aug. 1928), pp. 617–618. DOI: [10.1007/BF01494093](https://doi.org/10.1007/BF01494093) (cit. on p. 40).

BIBLIOGRAPHY

- [47] Georges Charpak et al. “The use of multiwire proportional counters to select and localize charged particles”. In: *Nucl. Instrum. Meth.* 62 (1968), pp. 262–268. DOI: [10.1016/0029-554X\(68\)90371-6](https://doi.org/10.1016/0029-554X(68)90371-6) (cit. on pp. 42, 43).
- [48] A. H. Walenta, J. Heintze, and B. Schuerlein. “The multiwire drift chamber, a new type of proportional wire chamber”. In: *Nucl. Instrum. Meth.* 92 (1971), pp. 373–380. DOI: [10.1016/0029-554X\(71\)90413-7](https://doi.org/10.1016/0029-554X(71)90413-7) (cit. on p. 43).
- [49] D.C. Cheng et al. “Very large proportional drift chambers with high spatial and time resolutions”. In: *Nuclear Instruments and Methods* 117.1 (1974), pp. 157–169. ISSN: 0029-554X. DOI: [http://dx.doi.org/10.1016/0029-554X\(74\)90394-2](http://dx.doi.org/10.1016/0029-554X(74)90394-2) (cit. on p. 43).
- [50] Claus Grupen and Boris Schwartz. *Particle detectors*. 2008 (cit. on p. 43).
- [51] Nina A. Filatova et al. “Study of Drift Chamber System for a K^-e Scattering Experiment at the Fermi National Accelerator Laboratory”. In: *Nucl. Instrum. Meth.* 143 (1977), p. 17. DOI: [10.1016/0029-554X\(77\)90326-3](https://doi.org/10.1016/0029-554X(77)90326-3) (cit. on p. 44).
- [52] Claus Grupen and Boris Shwartz. *Particle detectors*. Vol. 26. Cambridge university press, 2008 (cit. on p. 46).
- [53] A Oed. “Properties of micro-strip gas chambers (MSGC) and recent developments”. In: *Nuclear Instruments and Methods in Physics Research Section A: Accelerators, Spectrometers, Detectors and Associated Equipment* 367.1-3 (1995), pp. 34–40 (cit. on p. 46).
- [54] Fabio Sauli. “GEM: A new concept for electron amplification in gas detectors”. In: *Nuclear Instruments and Methods in Physics Research Section A: Accelerators, Spectrometers, Detectors and Associated Equipment* 386.2-3 (1997), pp. 531–534 (cit. on p. 46).
- [55] Yannis Giomataris et al. “MICROMEAS: a high-granularity position-sensitive gaseous detector for high particle-flux environments”. In: *Nuclear Instruments and Methods in Physics Research Section A: Accelerators, Spectrometers, Detectors and Associated Equipment* 376.1 (1996), pp. 29–35 (cit. on pp. 46, 47).
- [56] B Mindur et al. “Development of Micro-Pattern Gas Detectors Technologies”. In: (2008) (cit. on p. 46).

- [57] Fabio Sauli. “The gas electron multiplier (GEM): Operating principles and applications”. In: *Nuclear Instruments and Methods in Physics Research Section A: Accelerators, Spectrometers, Detectors and Associated Equipment* 805 (2016), pp. 2–24 (cit. on p. 46).
- [58] Rajendra Nath Patra et al. “Measurement of basic characteristics and gain uniformity of a triple GEM detector”. In: *Nuclear Instruments and Methods in Physics Research Section A: Accelerators, Spectrometers, Detectors and Associated Equipment* 862 (2017), pp. 25–30 (cit. on p. 47).
- [59] Enrico Costa et al. “An efficient photoelectric X-ray polarimeter for the study of black holes and neutron stars”. In: *Nature* 411.6838 (2001), pp. 662–665 (cit. on p. 48).
- [60] Ronaldo Bellazzini et al. “Reading a GEM with a VLSI pixel ASIC used as a direct charge collecting anode”. In: *Nuclear Instruments and Methods in Physics Research Section A: Accelerators, Spectrometers, Detectors and Associated Equipment* 535.1 (2004), pp. 477–484 (cit. on p. 48).
- [61] Wolfram Erdmann. “The front-end for the CMS pixel detector”. In: *Nuclear Instruments and Methods in Physics Research Section A: Accelerators, Spectrometers, Detectors and Associated Equipment* 549.1 (2005), pp. 153–156 (cit. on p. 48).
- [62] Xavier Llopart et al. “Medipix2, a 64k pixel read out chip with 55/spl mu/m square elements working in single photon counting mode”. In: *Nuclear Science Symposium Conference Record, 2001 IEEE*. Vol. 3. IEEE. 2001, pp. 1484–1488 (cit. on p. 48).
- [63] Xavier Llopart Cudié. “Design and characterization of 64K pixels chips working in single photon processing mode”. PhD thesis. Mid Sweden U., Sundsvall, 2007 (cit. on p. 48).
- [64] T Poikela et al. “Timepix3: a 65K channel hybrid pixel readout chip with simultaneous ToA/ToT and sparse readout”. In: *Journal of instrumentation* 9.05 (2014), p. C05013 (cit. on p. 48).
- [65] Marc J Madou. *Fundamentals of microfabrication: the science of miniaturization*. CRC press, 2002 (cit. on p. 50).
- [66] Ralph Müller. “Design and construction of precision tooling for the construction of resistive strip micromegas detectors for the ATLAS Small Wheel upgrade project”. In: *Nuclear Science Symposium and Medical Imaging Conference (NSS/MIC), 2015 IEEE*. IEEE. 2015, pp. 1–6 (cit. on p. 50).

BIBLIOGRAPHY

- [67] Hiroyuki Sako et al. “Development of a GEM-based TPC for H-dibaryon Search at J-PARC”. In: *PoS* (2014), p. 300 (cit. on p. 50).
- [68] Tom Francke. *Innovative applications and developments of micro-pattern gaseous detectors*. IGI Global, 2014 (cit. on p. 50).
- [69] SP George et al. “Particle tracking with a Timepix based triple GEM detector”. In: *Journal of Instrumentation* 10.11 (2015), P11003 (cit. on p. 51).
- [70] Ulrich Einhaus, Jochen Kaminski, and Michele Caselle. “ROPPERI-A TPC read-out with GEMs, pads and Timepix”. In: *arXiv preprint arXiv:1801.07178* (2018) (cit. on p. 51).
- [71] MA Chefdeville. “Development of micromegas-like gaseous detectors using a pixel readout chip as collecting anode”. PhD thesis. Paris-Saclay University, Amsterdam University, 2009 (cit. on p. 51).
- [72] Gilles De Lentdecker. “A large TPC prototype for an ILC detector”. In: *Nuclear Science Symposium Conference Record (NSS/MIC), 2009 IEEE*. IEEE, 2009, pp. 2283–2285 (cit. on p. 52).
- [73] M Lupberger. “The Pixel-TPC: first results from an 8-InGrid module”. In: *Journal of Instrumentation* 9.01 (2014), p. C01033 (cit. on pp. 52, 120).
- [74] Peter Schade, Jochen Kaminski, Lctpc Collaboration, et al. “A large TPC prototype for a linear collider detector”. In: *Nuclear Instruments and Methods in Physics Research Section A: Accelerators, Spectrometers, Detectors and Associated Equipment* 628.1 (2011), pp. 128–132 (cit. on p. 52).
- [75] J Kaminski et al. “GridPix detectors—introduction and applications”. In: *Nuclear Instruments and Methods in Physics Research Section A: Accelerators, Spectrometers, Detectors and Associated Equipment* 845 (2017), pp. 233–235 (cit. on p. 52).
- [76] Michael Lupberger. “The Pixel-TPC: A feasibility study”. PhD thesis. Bonn U., 2015-08-31 (cit. on pp. 53, 120, 124, 126).
- [77] Fred Hartjes Kevin Heijhof Jochen Kaminsky Kees Ligtenberg Gerhard Raven Jan Timmermans Klaus Desch Harry van der Graaf. “Pixel TPC simulation, geometry and expected performance”. In: *LCTPC Collaboration Meeting* (2017) (cit. on p. 54).

- [78] Michael Lupberger et al. “Toward the Pixel-TPC: Construction and operation of a large area GridPix detector”. In: *IEEE Transactions on Nuclear Science* 64.5 (2017), pp. 1159–1167 (cit. on p. 53).
- [79] M Alves et al. “PHIL photoinjector test line”. In: *Journal of Instrumentation* 8.01 (2013), T01001 (cit. on pp. 56, 64).
- [80] Thomas Vinatier. “Influence of laser parameters on the relativistic short electron bunches dynamics in linear accelerators based on RF-guns and development of associated diagnostics”. PhD thesis. Université Paris Sud-Paris XI, 2015 (cit. on pp. 56–60).
- [81] J Arthur et al. *Linac coherent light source (LCLS) conceptual design report*. Tech. rep. 2002 (cit. on p. 59).
- [82] M Vogt et al. “Status of the free electron laser user facility FLASH”. In: *Proc. 5th Int. Particle Accelerator Conf.(Dresden, Germany, 2014)*. Vol. 938. 2014 (cit. on p. 59).
- [83] Julien Branlard et al. “European XFEL RF Gun Commissioning and LLRF Linac Installation”. In: *Proceedings, 5th International Particle Accelerator Conference (IPAC 2014): Dresden, Germany, June 15-20, 2014*. 2014, WEPME065 (cit. on p. 59).
- [84] Robert B Palmer. “A laser driven grating linac”. In: *Part. Accel.* 11.Print-80-0475 (1980), pp. 81–90 (cit. on p. 60).
- [85] Peter Forck. “Lecture notes on beam instrumentation and diagnostics: Joint University Accelerator School, January-March 2011”. In: (2015) (cit. on p. 60).
- [86] Hung-chi Lihn et al. “Measurement of subpicosecond electron pulses”. In: *Physical Review E* 53.6 (1996), p. 6413 (cit. on p. 60).
- [87] Harsh Purwar et al. “Estimation of Longitudinal Dimensions of Sub-Picosecond Electron Bunches with the 3-Phase Method”. In: *8th Int. Particle Accelerator Conf.(IPAC’17), Copenhagen, Denmark, 14â 19 May, 2017*. JACOW, Geneva, Switzerland. 2017, pp. 139–141 (cit. on p. 60).
- [88] Enrica Chiadroni. *Bunch length characterization at the TTF VUV-FEL*. Tech. rep. 2006 (cit. on p. 60).

BIBLIOGRAPHY

- [89] Thomas Vinatier et al. “Length measurement of high-brightness electron beam thanks to the 3-phase method”. In: *5th International Particle Accelerator Conference IPAC’14*. Joint Accelerator Conferences Website. 2014, pp. 3459–3461 (cit. on p. 61).
- [90] *Delta Elektronik SM 800 series power supply datasheet* (cit. on p. 65).
- [91] *Opera FEA Simulation Software* (cit. on p. 66).
- [92] Karl Spanner and Burhanettin Koc. “Piezoelectric motors, an overview”. In: *Actuators*. Vol. 5. 1. Multidisciplinary Digital Publishing Institute. 2016, p. 6 (cit. on p. 69).
- [93] Karmjit Sidhu. *Understanding Linear Position Sensing Technologies* (cit. on p. 70).
- [94] *NSE-5310 Miniature Position Encoder with Zero Reference and I²C Output* (cit. on pp. 70, 71).
- [95] Philips Semiconductors. “The I2C-bus specification”. In: *Philips Semiconductors 9397.750* (2000), p. 00954 (cit. on p. 71).
- [96] *TE-STM32F107* (cit. on p. 72).
- [97] *STM32F407xx datasheet*. 15274. Rev. 10. ST Microelectronics. Mar. 2017 (cit. on p. 72).
- [98] *lwIP - A Lightweight TCP/IP stack* (cit. on p. 72).
- [99] *TE-STM32F107 Ethernet periphery configuration* (cit. on p. 72).
- [100] *LEETECH Master board MAC address configuraion* (cit. on p. 72).
- [101] *LEETECH Master board TCP/IP configuraion* (cit. on p. 72).
- [102] *STM32F407xx datasheet*. 022152. Rev. 4. ST Microelectronics. June 2013 (cit. on p. 73).
- [103] Hang Wu, Weihua Su, and Zhiguo Liu. “PID controllers: Design and tuning methods”. In: *Industrial Electronics and Applications (ICIEA), 2014 IEEE 9th Conference on*. IEEE. 2014, pp. 808–813 (cit. on p. 76).
- [104] M Pillon, M Angelone, and AV Krasilnikov. “14 MeV neutron spectra measurements with 4% energy resolution using a type IIa diamond detector”. In: *Nuclear Instruments and Methods in Physics Research Section B: Beam Interactions with Materials and Atoms* 101.4 (1995), pp. 473–483 (cit. on p. 84).

-
- [105] H Fraiss-Kolbl et al. “A fast low-noise charged-particle CVD diamond detector”. In: *IEEE Transactions on nuclear science* 51.6 (2004), pp. 3833–3837 (cit. on p. 84).
- [106] S Han et al. “Temporally resolved response of a natural type IIA diamond detector to single-particle excitation”. In: *Diamond and Related Materials* 2.5-7 (1993), pp. 835–840 (cit. on p. 84).
- [107] M Pomorski et al. “Charge transport properties of single crystal CVD-diamond particle detectors”. In: *Diamond and Related materials* 16.4 (2007), pp. 1066–1069 (cit. on p. 84).
- [108] Shan Liu et al. “In vacuum diamond sensor scanner for beam halo measurements in the beam line at the KEK Accelerator Test Facility”. In: *Nuclear Instruments and Methods in Physics Research Section A: Accelerators, Spectrometers, Detectors and Associated Equipment* 832 (2016), pp. 231–242 (cit. on p. 84).
- [109] D El Khechen et al. “First Tests of SuperKEKB Luminosity Monitors during 2016 Single Beam Commissioning”. In: *hist* 16.18 (2016), p. 20 (cit. on p. 84).
- [110] <http://www.e6.com>. Accessed: 2018-03-30 (cit. on p. 84).
- [111] C Weiss et al. “Ionization signals from diamond detectors in fast-neutron fields”. In: *The European Physical Journal A* 52.9 (2016), p. 269 (cit. on p. 85).
- [112] Dominique Breton et al. “The WaveCatcher family of SCA-based 12-bit 3.2-GS/s fast digitizers”. In: *Real Time Conference (RT), 2014 19th IEEE-NPSS*. IEEE, 2014, pp. 1–8 (cit. on pp. 90, 135).
- [113] Alexander Kalweit, ALICE collaboration, et al. “Particle identification in the ALICE experiment”. In: *Journal of Physics G: Nuclear and Particle Physics* 38.12 (2011), p. 124073 (cit. on p. 96).
- [114] Richard Talman. “On the statistics of particle identification using ionization”. In: *Nuclear Instruments and Methods* 159.1 (1979), pp. 189–211 (cit. on p. 97).
- [115] Hans Bichsel. “Comparison of Bethe-Bloch and Bichsel functions”. In: *STAR Note* 439 (2002) (cit. on p. 97).
- [116] A Andryakov et al. “dE/dx measurement in a He-based gas mixture”. In: *Nuclear Instruments and Methods in Physics Research Section A: Accelerators, Spectrometers, Detectors and Associated Equipment* 409.1-3 (1998), pp. 390–394 (cit. on p. 97).

BIBLIOGRAPHY

- [117] P. Valente G. Finocchiaro M. Piccolo. *dE/dx resolution in a 90GeV/c pions*. KLOE note 161. July 1997 (cit. on pp. [98](#), [99](#)).
- [118] Jean-François Caron et al. “Improved particle identification using cluster counting in a full-length drift chamber prototype”. In: *Nuclear Instruments and Methods in Physics Research Section A: Accelerators, Spectrometers, Detectors and Associated Equipment* 735 (2014), pp. 169–183 (cit. on pp. [99](#), [100](#)).
- [119] V. V. Berdnikov, S. V. Somov, and L. Pentchev. “Use of cluster counting technique for particle identification in a drift chamber with the cathode strip readout”. In: *Instrum. Exp. Tech.* 58.4 (2015). [Prib. Tekh. Eksp.2015,no.4,32(2015)], pp. 473–477. DOI: [10.1134/S0020441215030185](#) (cit. on p. [99](#)).
- [120] L. Cerrito et al. “Cluster counting in a large drift chamber in He 80% - CH₄ 20% at normal conditions”. In: (1998) (cit. on p. [99](#)).
- [121] R. Perrino et al. “Cluster counting drift chamber as high precision tracker for ILC experiments”. In: *Nucl. Instrum. Meth.* A598 (2009), pp. 98–101. DOI: [10.1016/j.nima.2008.08.073](#) (cit. on pp. [99–101](#)).
- [122] I Smirnov. “Heed: interactions of particles with gases”. In: *W5060*, <http://consult.cern.ch/writeup/heed> () (cit. on p. [101](#)).
- [123] WWM Allison and JH Cobb. “Relativistic charged particle identification by energy loss”. In: *Annual Review of Nuclear and Particle Science* 30.1 (1980), pp. 253–298 (cit. on p. [101](#)).
- [124] John Apostolakis et al. “An implementation of ionisation energy loss in very thin absorbers for the GEANT4 simulation package”. In: *Nuclear Instruments and Methods in Physics Research Section A: Accelerators, Spectrometers, Detectors and Associated Equipment* 453.3 (2000), pp. 597–605 (cit. on p. [103](#)).
- [125] GEANT Collaboration et al. “Physics reference manual”. In: *Version: 4.10.3* (2016) (cit. on pp. [103](#), [105](#)).
- [126] V. Grichine. “Recent validation and improvements of Geant4 standard EM package at low energies”. In: *16th Geant4 Collaboration Meeting* (2011) (cit. on p. [103](#)).
- [127] V Ivanchenko et al. “Geant4 electromagnetic physics: improving simulation performance and accuracy”. In: *SNA+ MC 2013-Joint International Conference on Supercomputing in Nuclear Applications+ Monte Carlo*. EDP Sciences. 2014, p. 03101 (cit. on p. [104](#)).

- [128] V Ivantchenko et al. “Overview and new developments in Geant4 electromagnetic physics”. In: (2005) (cit. on pp. 104, 108).
- [129] *Geant4 Application Developer User Guide*. <http://geant4.cern.ch/G4UsersDocuments/UsersGuides/ForApplicationDeveloper/html/GettingStarted/particleDef.html#2.4.2>. Accessed: 2017-10-18 (cit. on p. 105).
- [130] *Geant4 Application Developer User Guide*. <https://geant4.web.cern.ch/geant4/UserDocumentation/UsersGuides/ForApplicationDeveloper/html/ch05s07.html>. Accessed: 2017-10-18 (cit. on p. 105).
- [131] CDR Azevedo et al. “Position resolution limits in pure noble gaseous detectors for X-ray energies from 1 to 60 keV”. In: *Physics Letters B* 741 (2015), pp. 272–275 (cit. on p. 110).
- [132] *Various gas mixtures transport coefficients storage (Magboltz calculation)*. (Cit. on p. 121).
- [133] Pierre Billoir and S Qian. “Simultaneous pattern recognition and track fitting by the Kalman filtering method”. In: *Nuclear Instruments and Methods in Physics Research Section A: Accelerators, Spectrometers, Detectors and Associated Equipment* 294.1-2 (1990), pp. 219–228 (cit. on p. 118).
- [134] Wouter D Hulsbergen. “Decay chain fitting with a Kalman filter”. In: *Nuclear Instruments and Methods in Physics Research Section A: Accelerators, Spectrometers, Detectors and Associated Equipment* 552.3 (2005), pp. 566–575 (cit. on p. 118).
- [135] Wolfgang Adam et al. “Reconstruction of electrons with the Gaussian-sum filter in the CMS tracker at the LHC”. In: *Journal of Physics G: Nuclear and Particle Physics* 31.9 (2005), N9 (cit. on p. 118).
- [136] Are Strandlie and Rudolf Fruhwirth. “Track and vertex reconstruction: From classical to adaptive methods”. In: *Rev. Mod. Phys.* 82 (2010), pp. 1419–1458. DOI: [10.1103/RevModPhys.82.1419](https://doi.org/10.1103/RevModPhys.82.1419) (cit. on p. 120).
- [137] Gary Bradski and Adrian Kaehler. “OpenCV”. In: *Dr. Dobb’s journal of software tools* 3 (2000) (cit. on p. 120).
- [138] John Illingworth and Josef Kittler. “A survey of the Hough transform”. In: *Computer vision, graphics, and image processing* 44.1 (1988), pp. 87–116 (cit. on p. 120).

BIBLIOGRAPHY

- [139] Dana H Ballard. “Generalizing the Hough transform to detect arbitrary shapes”. In: *Readings in computer vision*. Elsevier, 1987, pp. 714–725 (cit. on p. 120).
- [140] Leonid Burmistrov. “A detector for charged particle identification in the forward region of SuperB”. PhD thesis. Université Paris Sud-Paris XI, 2011 (cit. on p. 133).
- [141] L Bardelli et al. “Time measurements by means of digital sampling techniques: a study case of 100 ps FWHM time resolution with a 100 MSample/s, 12 bit digitizer”. In: *Nuclear Instruments and Methods in Physics Research Section A: Accelerators, Spectrometers, Detectors and Associated Equipment* 521.2-3 (2004), pp. 480–492 (cit. on p. 135).
- [142] O Atanova et al. “Measurement of the energy and time resolution of a undoped CsI+ MPPC array for the Mu2e experiment”. In: *Journal of Instrumentation* 12.05 (2017), P05007 (cit. on p. 135).
- [143] Yang Hai-Bo et al. “Application of the DRS4 chip for GHz waveform digitizing circuits”. In: *Chinese Physics C* 39.5 (2015), p. 056101 (cit. on p. 135).
- [144] N Cartiglia et al. “Beam test results of a 16 ps timing system based on ultra-fast silicon detectors”. In: *Nuclear Instruments and Methods in Physics Research Section A: Accelerators, Spectrometers, Detectors and Associated Equipment* 850 (2017), pp. 83–88 (cit. on p. 137).
- [145] Frédéric Nolet et al. “Digital SiPM channel integrated in CMOS 65 nm with 17.5 ps FWHM single photon timing resolution”. In: *Nuclear Instruments and Methods in Physics Research Section A: Accelerators, Spectrometers, Detectors and Associated Equipment* (2017) (cit. on p. 137).



APPENDIX

A.1 Geant4 PhysicsLists options for primary ionization simulation

Geant4 proposes several out-of-box *PhysicsLists* around which the simulation can be built. The main trade-off is a performance-accuracy compromise, which level should be selected for a given project individually. The *PhysicsLists* classes with their description according to the Geant4 documentation are summarized in Table [A.1](#).

PhysicsList	Comments
G4EmStandardPhysics	Provides construction of default EM standard physics
G4EmStandardPhysics_option1	Provides construction of EM standard physics using set of options allowing speed up simulation. Results for simulation in thin layers of materials with different density may be biased.
G4EmStandardPhysics_option2	Provides construction of EM standard physics using set of options allowing to utilize sub-cutoff option for ionization processes and higher production threshold than in default EM physics.
G4EmStandardPhysics_option3	Provides construction of EM standard physics using set of the most advanced options allowing precise simulation at low and intermediate energies
G4EmStandardPhysics_option4	Provides construction of EM physics using the best models of standard and low-energy packages and set of the most advanced options allowing precise simulation at low and intermediate energies

Table A.1: *Standard electromagnetic PhysicsLists description in Geant4*

Titre : Source polyvalente d'électrons de basse énergie sur l'accélérateur PHIL pour caractériser des détecteurs Micromegas avec une lecture CMOS intégrée et étudier dE/dx pour les électrons de basse énergie

Mots clés : Instrumentation de faisceaux, Micromegas-InGrid, Geant4

Résumé : Les futures expériences en physique des hautes énergies nécessitent une augmentation de la précision de détection sur de plus en plus grands volumes (où surfaces). Les précisions spatiales et temporelles sont importantes ainsi que la collecte rapide des signaux, la réduction du temps mort et l'amélioration de la résistance aux radiations. Les détecteurs gazeux sont reconnus pour leur efficacité dans des expériences où de grands volumes sont mis en jeu, là où les détecteurs silicium ne peuvent pas être exploités. Par conséquent, de nouvelles R&D complexes ont été lancées sur des détecteurs gazeux à hautes performances.

Cette thèse de R&D porte sur une nouvelle technologie Micromegas/InGrid développée par le Laboratoire de l'Accélérateur Linéaire (LAL), l'Université Nationale de Kiev et le CEA dans le cadre de la collaboration LCTPC. Pour cela, une plate-forme polyvalente appelée LEETECH a été conçue, construite et mise en service sur le faisceau d'accélérateur à photo-injecteur PHIL du LAL.

Un cadre de simulation basé sur Geant4 a été développé, fournissant des informations sur les caractéristiques des clusters à la sortie de LEETECH en fonction des paramètres de configuration de l'ins-

tallation.

Suite à la caractérisation de l'installation, plusieurs campagnes de mesures pour différentes technologies de détection ont été réalisées sur LEETECH. Les mesures du capteur de diamant ont démontré la capacité de LEETECH à fournir des paquets composés de quelques électrons et ont démontré la capacité du capteur de diamant à résoudre les signaux provenant de tels paquets.

Une caractérisation du premier détecteur Micromegas/InGrid de grande surface utilisant les électrons de basse énergie a été réalisée et plusieurs caractéristiques telles que la résolution spatiale et les pertes par ionisation ont été mesurées. La technique de reconstruction de traces a été optimisée en tenant compte de la diffusion multiple et peut éventuellement être réutilisée pour la reconstruction online des futures expériences.

Enfin, la caractérisation temporelle de la barre de quartz couplée au MCP-PMT a été effectuée. Une résolution temporelle de 50 ps a été obtenue. Il s'agit d'une première démonstration du développement du détecteur de temps de vol pour un futur accélérateur tau-charm.

Title : Versatile low-energy electron source at the PHIL accelerator to characterise Micromegas with integrated Timepix CMOS readout and study dE/dx for low energy electrons

Keywords : Beam-line instrumentation, Micromegas-InGrid, Geant4

Abstract : For the future experiments the precision tracking in large volumes/surfaces is required. Both spatial and time precision is important as well as fast signal collection, low dead time and improved radiation resistance. Gaseous detectors are known to ensure an efficient tracking in large volumes of large-scale experiments where silicon detectors cannot be exploited for entire tracking systems.

New R&D programs require versatile test platforms with high precision, based on radioactive sources, cosmic ray muons and in particular calibrated beam facilities.

Within the present thesis the design, construction and commissioning of a new test beam facility LEETECH have been performed. Performance of the new facility, including low-multiplicity operation mode has been demonstrated. A number of detector tests, including large-area diamond, Micromegas/InGrid and quartz bar detectors have been performed.

Following the facility characterization, several measu-

rement campaigns for different detector technologies were performed at the LEETECH facility. The diamond sensor measurements demonstrated the functionality of LEETECH to provide bunches consisting of a few electrons and proved the diamond sensor ability to resolve signals from such bunches.

A characterization of the first large-area Micromegas/InGrid detector using the low-energy electrons has been performed and several characteristics such as spatial and dE/dx resolution were measured. The track reconstruction technique have been optimized for the case of medium track multiplicity and multiple scattering and can potentially be reused for similar problems.

Finally, timing characterization of the quartz bar coupled to MCP-PMT was performed. A time resolution of 50 ps was obtained. This is a first demonstration for a development of the forward time-of-flight detector for a future tau-charm factory.

